

AD-A210 571

# David Taylor Research Center

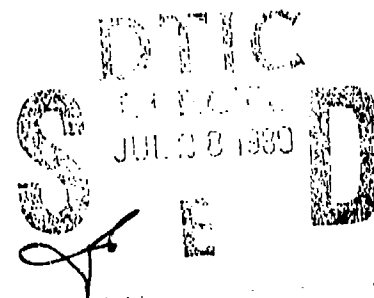
Bethesda, Maryland 20884-5000

DTRC/SME-88-81 April 1989

Ship Materials Engineering Department  
Research and Development Report

MECHANISMS OF STRENGTH AND TOUGHNESS IN A MICROALLOYED,  
PRECIPITATION HARDENED STEEL

M. E. Natishan

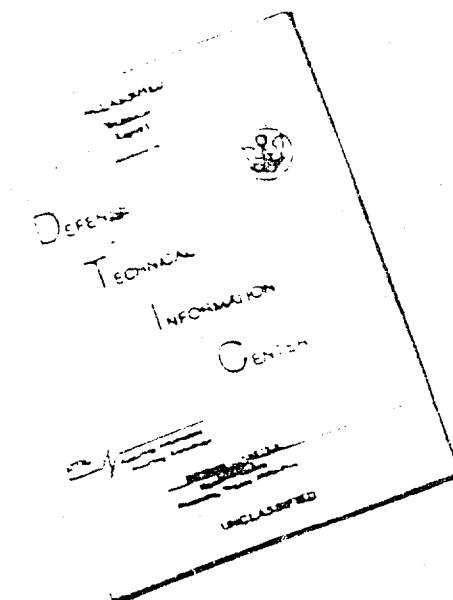


Approved for public release; distribution is unlimited.



89 7 28 0 55

# DISCLAIMER NOTICE



THIS DOCUMENT IS BEST  
QUALITY AVAILABLE. THE COPY  
FURNISHED TO DTIC CONTAINED  
A SIGNIFICANT NUMBER OF  
PAGES WHICH DO NOT  
REPRODUCE LEGIBLY.

REPRODUCED FROM  
BEST AVAILABLE COPY

## MAJOR DTRC TECHNICAL COMPONENTS

CODE 011 DIRECTOR OF TECHNOLOGY, PLANS AND ASSESSMENT

12 SHIP SYSTEMS INTEGRATION DEPARTMENT

14 SHIP ELECTROMAGNETIC SIGNATURES DEPARTMENT

15 SHIP HYDROMECHANICS DEPARTMENT

16 AVIATION DEPARTMENT

17 SHIP STRUCTURES AND PROTECTION DEPARTMENT

18 COMPUTATION, MATHEMATICS & LOGISTICS DEPARTMENT

19 SHIP ACOUSTICS DEPARTMENT

27 PROPULSION AND AUXILIARY SYSTEMS DEPARTMENT

28 SHIP MATERIALS ENGINEERING DEPARTMENT

### DTRC ISSUES THREE TYPES OF REPORTS:

1. **DTRC reports, a formal series**, contain information of permanent technical value. They carry a consecutive numerical identification regardless of their classification or the originating department.
2. **Departmental reports, a semiformal series**, contain information of a preliminary, temporary, or proprietary nature or of limited interest or significance. They carry a departmental alphanumeric identification.
3. **Technical memoranda, an informal series**, contain technical documentation of limited use and interest. They are primarily working papers intended for internal use. They carry an identifying number which indicates their type and the numerical code of the originating department. Any distribution outside DTRC must be approved by the head of the originating department on a case-by-case basis.

UNCLASSIFIED

SECURITY CLASSIFICATION OF THIS PAGE

## REPORT DOCUMENTATION PAGE

1a. REPORT SECURITY CLASSIFICATION UNCLASSIFIED			1d. RESTRICTIVE MARKINGS		
2a. SECURITY CLASSIFICATION AUTHORITY			3. DISTRIBUTION / AVAILABILITY OF REPORT		
2b. DECLASSIFICATION / DOWNGRADING SCHEDULE			Approved for public release; distribution unlimited.		
4. PERFORMING ORGANIZATION REPORT NUMBER(S) DTRC/SME-88-81			5. MONITORING ORGANIZATION REPORT NUMBER(S)		
6a. NAME OF PERFORMING ORGANIZATION David Taylor Research Center		6b. OFFICE SYMBOL (If applicable) Code 2814	7a. NAME OF MONITORING ORGANIZATION		
6c. ADDRESS (City, State, and ZIP Code) Bethesda, MD 20084-5000			7b. ADDRESS (City, State, and ZIP Code)		
8a. NAME OF FUNDING / SPONSORING ORGANIZATION David Taylor Research Center		8b. OFFICE SYMBOL (If applicable) Code 0113	9. PROCUREMENT INSTRUMENT IDENTIFICATION NUMBER		
8c. ADDRESS (City, State, and ZIP Code) Bethesda, MD 20084-5000			10. SOURCE OF FUNDING NUMBERS		
			PROGRAM ELEMENT NO. 61152N	PROJECT NO. RR00001	TASK NO. RR0000101
			WORK UNIT ACCESSION NO. DN505505		
11. TITLE (Include Security Classification) (U) MECHANISMS OF STRENGTH AND TOUGHNESS IN A MICROALLOYED, PRECIPITATION HARDENED STEEL					
12. PERSONAL AUTHOR(S) M. E. Natishan					
13a. TYPE OF REPORT		13b. TIME COVERED FROM TO		14. DATE OF REPORT (Year, Month, Day) 1989 April	
				15. PAGE COUNT 225	
16. SUPPLEMENTARY NOTATION					
17. COSATI CODES			18. SUBJECT TERMS (Continue on reverse if necessary and identify by block number)		
FIELD	GROUP	SUB-GROUP	HSLA Steel; Structure/Property Relationship; Fracture Characteristics; Physical Metallurgy		
19. ABSTRACT (Continue on reverse if necessary and identify by block number) The microstructural parameters contributing to the strength and toughness of low carbon, microalloyed, precipitation hardenable steels were identified in two ASTM A710, grade A, 50 mm thick plates in the re-austenitized, quenched and aged condition. Tensile, impact toughness and fracture toughness properties were determined over a full range of test temperatures to characterize the mechanical behavior and the fracture processes in the fracture mode transition temperature region, especially as related to cleavage failure and cracking parallel to the loading direction (longitudinal cracking). Microstructural and fractographic characterization using optical microscopy, along with SEM and TEM techniques identified planar arrays of carbide precipitates (in the longitudinal direction) and a non-homogeneous grain size distribution as the primary contributing factors to lower toughness, while copper precipitation played a large role in strengthening.					
20. DISTRIBUTION / AVAILABILITY OF ABSTRACT <input type="checkbox"/> UNCLASSIFIED/UNLIMITED <input type="checkbox"/> SAME AS RPT <input type="checkbox"/> DTIC USERS			21. ABSTRACT SECURITY CLASSIFICATION (U)		
22a. NAME OF RESPONSIBLE INDIVIDUAL M. E. Natishan			22b. TELEPHONE (Include Area Code) (301) 267-2264		22c. OFFICE SYMBOL Code 2814



## TABLE OF CONTENTS

INTRODUCTION.....	1
BACKGROUND	
Microstructural Strengthening Mechanisms and Their Effect on Material Toughness.....	5
Grain Size Strengthening.....	7
Precipitation and Dispersion Strengthening.....	20
The Brittle Fracture of Steels.....	35
EXPERIMENTAL PROCEDURE	
Material.....	61
Microstructural Characterization.....	61
Mechanical Property Characterization.....	66
Fractography and Fracture Mode Characterization....	73
RESULTS	
Material.....	77
Microstructural Characterization.....	78
Mechanical Properties.....	92
Fractography and Fracture Characterization.....	103
DISCUSSION	
Microstructure, Strength and Toughness.....	175
Mechanisms of Longitudinal Cracking in Tensile Specimens.....	190
CONCLUSION.....	199
SUGGESTED WORK.....	201

Accession For	
NTIS GRA&I	<input checked="" type="checkbox"/>
DTIC TAB	<input type="checkbox"/>
Unannounced	<input type="checkbox"/>
Justification.....	
By.....	
Distribution/	
Availability Codes	
Avail and/or	
Dist	Special
A-1	



## LIST OF TABLES

TABLE	PAGE
1. Chemical Compositions.....	78
2. Particle Size and Spacing.....	87
3. Transverse and Through-thickness Tensile Properties.....	98
4. A Comparison of FATT and Yield Strengths of the Two Plates Studied.....	103
5. Charpy V-Notch Cleavage Initiation Data.....	144
6. Cleavage Fracture Initiation Data Measured from Fracture Toughness Specimens.....	167

## LIST OF FIGURES

FIGURE	PAGE
1. The effects of grain size and alloy content on yield strength as predicted by Gladman.....	8
2. Factors contributing to the strength of controlled-rolled low alloy steel.....	12
3. The dependence of strengthening on precipitate size and volume fraction as predicted by the Ashby-Orowan model.....	27
4. The effects of alloy elements on the strength of controlled-rolled, low alloy steels.....	30
5. The effects of alloy additions on the ductile-brittle transition temperature in controlled-rolled, low alloy steels.....	33
6. Schematic of the ASTM specified, 505 tensile specimen used for determining tensile properties.....	68
7. Schematic of plate material with plate and specimen directions labelled.....	68
8. Schematic of the ASTM specified Charpy V-notch specimen used in all impact toughness testing.....	70
9. Schematic of the ASTM E813 specified compact-tension specimen used in quasi-static fracture toughness testing.....	72
10. (a) SEM Photomicrograph of the fracture surface of an impact toughness specimen with measured distances labelled.....	75
11. Optical photomicrographs, taken in the three orthogonal plate directions of the microstructure of plate GFF.....	80
12. Optical photomicrograph, taken in the three orthogonal plate directions, of the microstructure of plate GGN.....	81
13. Scanning electron photomicrograph of polished GGN specimens, etched in a 2% nital solution.....	82
14. Plot of the grain size distribution for the two plates characterized in this study.....	84

15. Transmission electron photomicrograph showing the particle distribution in plate GGN.....	82
16. Transmission electron photomicrograph showing copper precipitates in the microstructure of plate GGN.....	89
17. Transmission electron diffraction pattern taken from a region of copper precipitates.....	90
18. Transmission electron photomicrograph showing the clusters of copper precipitates in the microstructure of plate GFF.....	91
19. The load/displacement curves for one tensile specimen from each plate tested at $-40^{\circ}\text{C}$ .....	93
20. A plot of the tensile properties for plates GGN and GFF versus test temperature.....	94
21. A plot of the strain hardening exponent for the tensile specimens from plates GGN and GFF versus test temperature.....	95
22. A plot of the tensile ductility properties for specimens from both plates versus test temperature.....	97
23. A plot of the Charpy V-notch impact energies for specimens from both plates GFF and GGN versus test temperature.....	100
24. A plot of $J_{IC}$ and $J_C$ fracture toughness versus test temperature for specimens from both plates GFF and GGN.....	101
25. Line drawings showing the crack opening directions and the corresponding dimple shapes of the uniform strain mode and the three primary crack opening modes.....	105
26. Scanning electron photomicrograph of the fracture surface of tensile specimen GFF-1 tested at $24^{\circ}\text{C}$ ...	108
27. Scanning electron (SEM) photomicrograph of the dimple morphology of tensile specimen GFF-1.....	109
28. SEM photomicrograph of the matching fracture surfaces of tensile specimen GFF-2 tested at $-18^{\circ}\text{C}$ showing longitudinal cracking.....	110

29. SEM photomicrograph of the matching fracture surfaces of tensile specimen GFF-3 tested at -45° C showing longitudinal cracking.....	111
30. SEM photomicrograph of tensile specimen GFF-4 tested at -75° C.....	112
31. SEM photomicrograph of specimen GFF-4.....	113
32. SEM photomicrograph of the shear lip fracture area of tensile specimen GFF-2 tested at -18° C.....	114
33. SEM photomicrograph of the regions of longitudinal cracking in tensile specimen GFF-2 tested at -18° C showing the fracture mode to be microvoid coalescence.....	115
34. SEM photomicrograph of one fracture surface from tensile specimen GFF-6 tested at -130° C showing the transverse fracture surfaces on either side of the necked region.....	116
35. SEM photomicrograph of the matching fracture surfaces of tensile specimen GFF-7 tested at -130° C.....	117
36. SEM photomicrograph of the longitudinal crack in tensile specimen GFF-7 with ductile tearing exhibited at the edge of the crack while the rest of the fracture mode is cleavage.....	119
37. SEM photomicrograph of the matching surface to Figure 35.....	120
38. SEM photomicrograph of the longitudinal crack in the necked region of tensile specimen GFF-8 tested at -155° C showing mechanical fibering due to plastic deformation.....	121
39. SEM photomicrograph of the longitudinal crack shown in Figure 37.....	122
40. SEM photomicrograph of the longitudinal crack shown in Figure 37, in the region of crack arrest..	122
41. SEM photomicrograph of matching fracture surfaces of tensile specimen GGN-150 tested at 22° C.....	123
42. SEM photomicrographs of the matching fracture surfaces from specimen GGN-151 tested at 22° C showing a radial pattern of longitudinal cracks....	124

43. SEM photomicrograph of matching fracture surfaces from tensile specimen GGN-152 tested at $-18^{\circ}\text{C}$ showing a single, through diameter, longitudinal crack.....	125
44. SEM photomicrographs of matching fracture surfaces from tensile GGN-153 tested at $-20^{\circ}\text{C}$ .....	126
45. Stereo SEM fractographs of the central part of the fracture surface from tensile specimen GGN-153.....	127
46. Stereo SEM fractographs of the fracture surface near the outer edge of tensile specimen GGN-153....	128
47. SEM photomicrographs of the fracture surface of the longitudinal crack in tensile specimen GGN-151 showing opening mode dimples.....	129
48. SEM photomicrographs of the longitudinal crack fracture surfaces from specimen GGN-151 showing shear mode dimples.....	131
49. SEM photomicrographs of the fracture surface of specimen GGN-150 in the shear lip area.....	132
50. SEM photomicrograph of matching fracture surfaces of tensile specimen GGN-155 tested at $-45^{\circ}\text{C}$ .....	133
51. SEM photomicrographs of matching fracture surfaces of tensile specimen GGN-156 tested at $-73^{\circ}\text{C}$ showing a single, through diameter longitudinal crack.....	134
52. SEM photomicrograph of shear dimples on the transverse fracture surface adjacent to the longitudinal cracks in specimen GGN-156.....	135
53. SEM stereo-photomicrograph of the transverse fracture surface of specimen GGN-156 showing a mixed cleavage and ductile fracture mode.....	136
54. SEM photomicrograph of matching transverse fracture surfaces of tensile specimen GGN-160 tested at $-130^{\circ}\text{C}$ .....	137
55. SEM photomicrographs of the longitudinal crack surface from the tensile specimen GGN-160.....	138
56. SEM photomicrograph of the fracture surface of Charpy impact specimen GFF-116 tested at $-62^{\circ}\text{C}$ .....	140

57. SEM photomicrograph of the fracture surface of Charpy impact specimen GFF-116.....	141
58. SEM photomicrographs of the fracture surface of Charpy impact specimen GGN-128 tested at 22° C showing a microvoid coalescence fracture mode....	142
59. SEM photomicrographs of the fracture surface of Charpy impact specimen GFF-134 tested at -105° C.....	146
60. SEM photomicrograph of the fracture surface of Charpy impact specimen GGN-120 tested at 37° C.....	147
61. SEM photomicrograph of the fracture surface of Charpy impact specimen GGN-124 tested at -50° C....	148
62. SEM photomicrograph of the fracture surface of Charpy impact specimen GGN-124.....	149
63. SEM photomicrograph of the fracture surface of Charpy impact specimen GFF-111 tested at -120° C...	150
64. SEM photomicrograph of the cleavage initiation site of Charpy impact specimen GFF-111.....	151
65. SEM photomicrograph of the fracture surface of Charpy impact specimen GGN-108 tested at -130° C...	152
66. SEM photomicrograph of the cleavage initiation site on the fracture surface of GGN-108.....	153
67. SEM photomicrograph of the fracture surface of fracture toughness specimen GGN-27 tested at -10° C.....	155
68. SEM photomicrograph of the stable crack growth region of GGN-27.....	156
69. Plot of the dimple diameter distribution as measured from specimen GGN-27 compared to the plate GGN grain size distribution.....	158
70. SEM photomicrograph of the cleavage initiation region of GGN-27.....	159
71. SEM photomicrograph of fracture toughness specimen GGN-130 tested at -10° C.....	160
72. SEM photomicrograph of the cleavage initiation site on specimen GFF-11.....	161

73. SEM photomicrograph of the cleavage initiating particle on specimen GFF-11.....	162
74. SEM photomicrograph of the matching fracture surfaces from fracture toughness specimen GFF-2 tested at $-100^{\circ}$ C.....	163
75. SEM photomicrographs of the matching cleavage initiation sites of fracture toughness specimen GFF-2.....	165
76. SEM photomicrograph of the cleavage initiation site on surface one of specimen GFF-2.....	166
77. A plot of the distribution of secondary crack sizes measured adjacent to the primary crack in specimens from both plates.....	169
78. SEM photomicrograph of secondary cracks adjacent to the main crack in fracture toughness specimen GGN-27 tested at $-10^{\circ}$ C.....	171
79. SEM photomicrograph of secondary cracking in fracture toughness specimen GFF-14 tested at $-105^{\circ}$ C.....	172
80. SEM photomicrographs of secondary cracking in fracture toughness specimen GFF-11 tested at $-70^{\circ}$ C.....	173
81. Transmission electron photomicrograph showing particle/dislocation interactions in the microstructure of plate GFF.....	177
82. Transmission electron photomicrograph showing the particle/dislocation interactions in the microstructure of plate GGN.....	178
83. Transmission electron photomicrograph showing the "pinning" effect of particles on dislocation motion in the microstructure of plate GFF.....	180
84. Transmission electron photomicrograph showing the dislocation loops around precipitates in a microstructure consisting of copper precipitates in a ferrite matrix.....	181



# LIST OF SYMBOLS

ASTM	American Society for Testing and Materials
a	crack length
a <sub>c</sub>	critical crack length
b	Burger's vector
c	atomic concentration of solute atoms
°C	degrees Centigrade
cm	centimeters
C <sub>0</sub>	carbide particle thickness
CVN	Charpy V-notch
d	grain diameter
DBTT	ductile-brittle transition temperature
E	Young's modulus
%El	percent elongation
f	volume fraction of particles
FATT	fracture appearance transition temperature
f <sub>r</sub>	fraction of recrystallized ferrite
F.S.	fracture stress
G	shear modulus
Hz	hertz
J	joules
J <sub>C</sub>	cleavage fracture toughness
J <sub>IC</sub>	critical fracture toughness
K <sub>IC</sub>	critical stress intensity factor
kJ	kilojoule
k <sub>y</sub>	grain size coefficient
L	interparticle or solute atom spacing
(L)	longitudinal plate direction
LN <sub>2</sub>	liquid nitrogen
m	meter
m	grain boundary ledge density
MPa	megapascal
mm	millimeter
MN	meganeutron
n	number of dislocations
N	length of dislocation array
n	strain hardening exponent
RA	reduction in area
r	distance ahead of the crack tip
r <sub>a</sub>	matrix atom radius
r <sub>b</sub>	solute atom radius
r <sub>crit</sub>	maximum particle radius to counteract grain growth
R	radius of curvature of dislocation
R <sub>0</sub>	matrix grain radius
S	carbide strength
s	second
(S)	through thickness plate direction
SEM	scanning electron microscopy
T	dislocation line tension
T	temperature

(T)	transverse plate direction
TEM	transmission electron microscopy
UTS	ultimate tensile stress
V	plastic zone volume
V	volt
W	specimen width
X	mean planar particle intercept
X	distance ahead of crack tip within plastic zone
X <sub>0</sub>	characteristics
YS	yield stress
z	radii ratio (growing grains/matrix grain)

$\sigma$ $\sigma_s$ $\sigma_p$ $\sigma_d$ $\sigma_{f1}$ $\sigma_{f2}$ $\sigma_{f3}$ $\sigma_{f4}$ $\sigma_{f5}$ $\sigma_{f6}$ $\sigma_{f7}$ $\sigma_{f8}$ $\sigma_{f9}$ $\sigma_{f10}$ $\sigma_{f11}$ $\sigma_{f12}$ $\sigma_{f13}$ $\sigma_{f14}$ $\sigma_{f15}$ $\sigma_{f16}$ $\sigma_{f17}$ $\sigma_{f18}$ $\sigma_{f19}$ $\sigma_{f20}$ $\sigma_{f21}$ $\sigma_{f22}$ $\sigma_{f23}$ $\sigma_{f24}$ $\sigma_{f25}$ $\sigma_{f26}$ $\sigma_{f27}$ $\sigma_{f28}$ $\sigma_{f29}$ $\sigma_{f30}$ $\sigma_{f31}$ $\sigma_{f32}$ $\sigma_{f33}$ $\sigma_{f34}$ $\sigma_{f35}$ $\sigma_{f36}$ $\sigma_{f37}$ $\sigma_{f38}$ $\sigma_{f39}$ $\sigma_{f40}$ $\sigma_{f41}$ $\sigma_{f42}$ $\sigma_{f43}$ $\sigma_{f44}$ $\sigma_{f45}$ $\sigma_{f46}$ $\sigma_{f47}$ $\sigma_{f48}$ $\sigma_{f49}$ $\sigma_{f50}$ $\sigma_{f51}$ $\sigma_{f52}$ $\sigma_{f53}$ $\sigma_{f54}$ $\sigma_{f55}$ $\sigma_{f56}$ $\sigma_{f57}$ $\sigma_{f58}$ $\sigma_{f59}$ $\sigma_{f60}$ $\sigma_{f61}$ $\sigma_{f62}$ $\sigma_{f63}$ $\sigma_{f64}$ $\sigma_{f65}$ $\sigma_{f66}$ $\sigma_{f67}$ $\sigma_{f68}$ $\sigma_{f69}$ $\sigma_{f70}$ $\sigma_{f71}$ $\sigma_{f72}$ $\sigma_{f73}$ $\sigma_{f74}$ $\sigma_{f75}$ $\sigma_{f76}$ $\sigma_{f77}$ $\sigma_{f78}$ $\sigma_{f79}$ $\sigma_{f80}$ $\sigma_{f81}$ $\sigma_{f82}$ $\sigma_{f83}$ $\sigma_{f84}$ $\sigma_{f85}$ $\sigma_{f86}$ $\sigma_{f87}$ $\sigma_{f88}$ $\sigma_{f89}$ $\sigma_{f90}$ $\sigma_{f91}$ $\sigma_{f92}$ $\sigma_{f93}$ $\sigma_{f94}$ $\sigma_{f95}$ $\sigma_{f96}$ $\sigma_{f97}$ $\sigma_{f98}$ $\sigma_{f99}$ $\sigma_{f100}$	material constant
	amplitude of the crack tip stress singularity
	atomic misfit
	strain rate
	crack surface energy
	specific surface energy
	plastic work term
	failure probability
	dislocation density
	density of dislocation forest
	applied stress
	athermal stress
	crack tip tensile stress
	fracture stress
	matrix friction stress
	yield stress
	yield stress
	resolved shear stress
	resolved shear stress applied on slip plane
	stress to activate Frank-Read source
friction stress	
effective shear stress	
Poisson's ratio	

## ABSTRACT

The microstructural parameters contributing to the strength and toughness of low carbon, microalloyed, precipitation hardenable steels were identified in two ASTM A710, grade A, 50 mm thick plates in the reaustenitized, quenched and aged condition. Tensile, impact toughness and fracture toughness properties were determined over a full range of test temperatures to characterize the mechanical behavior and the fracture processes in the fracture mode transition temperature region, especially as related to cleavage failure and cracking parallel to the loading direction (longitudinal cracking). Microstructural and fractographic characterization, using optical microscopy, along with SEM and TEM techniques identified planar arrays of carbide precipitates (in the longitudinal direction) and a non-homogeneous grain size distribution as the primary contributing factors to lower toughness, while copper precipitation played a large role in strengthening.

## ADMINISTRATIVE INFORMATION

This report was prepared as part of the Micromechanisms of the Cleavage Fracture Process in Steels Program which was sponsored by DTRC's Independent Research Program under David D. Moran (Code 01). The work was performed at DTRC under Work Unit Number 1-2814-213, Program Element Number 61152N.

## INTRODUCTION

The microstructure-mechanical property relationships of structural steels have been widely studied for many years in an effort to improve the strength and fracture resistance of these materials without appreciably increasing the production and fabrication (welding) costs. Fueled by the demand for strong, tough, low cost steels by the construction, energy and transportation industries, this research resulted in the development of many new steel alloys tailored for various uses.

The microstructural features which can be varied to modify steel properties range in size from the atomic scale, as in solid solution hardening, to large particles and grain size distribution. The mechanisms to increase yield strength include solid solution hardening, dispersion and precipitation hardening, strain hardening and grain refinement. Chemistry, processing, and heat treating parameters can be varied to control the complex interaction of these mechanisms to produce a material optimized for a specific use. The microstructural features critical to strength and toughness include: grain size and shape of the transformation product, precipitate size and volume fraction, dislocation density, volume fraction and shape of non-metallic inclusions, carbide content and distribution, and texture [1].

The general trend in structural steel development has been to decrease carbon content in order to increase fabricability [2]. Microalloy additions of carbide stabilizers and precipitation hardening elements and tight control of processing parameters are used instead to give a fine grain size and a dispersion of fine precipitates which increase strength levels. Control of thermomechanical treatment parameters is critical in microalloyed steels since these affect the solution and reprecipitation kinetics of the carbides and nitrides which ultimately control the transformation product grain size [1].

When carbon content is lowered to the lowest possible values, other alloy additions take on a primary role in the strengthening process. Niobium, titanium, and vanadium are often added in small amounts for grain size control and precipitation strengthening [1,3] while copper addition results in a fine precipitate for strengthening [4]. Nickel additions act in solid solution to strengthen the matrix while also improving toughness [5].

A high strength, high toughness, microalloyed steel which takes advantage of the strengthening mechanisms described above is ASTM A710, Grade A steel. The austenitized, quenched and precipitation heat treated condition of this alloy is known as the Class 3 condition, which has an approximate yield strength of 517 MPa and

exhibits upper shelf fracture toughness behavior at room temperature [6]. This steel is finding many applications where the expected service temperatures are well below room temperature, such as in the oil industry (offshore platform construction and transcontinental pipelines) [7]. The tendency for failure in a cleavage fracture mode increases with decreasing service temperature resulting in a reduction in fracture toughness. Models to date have described the fracture process in high or medium carbon, high alloy steels. These models may not be adequate for describing the fracture process in very low carbon, microalloyed steels and certainly cannot be used to predict the microstructural parameters controlling the fracture process, and thus the strength, since the precipitates and even the grain structures are different. To fully understand the fracture process in these new "clean" steels, it is necessary to identify the microstructural features controlling their strength and toughness. The objective of this research project was to determine the microstructural parameters controlling the strength and toughness properties in ASTM A710, Grade A, Class 3, a microalloyed steel.

The approach used in this investigation combined detailed metallographic characterization of the microstructure and fracture surface features, with full characterization of the fracture properties, of two 50 mm ASTM A710, Grade A, Class 3, steel plates from different

producers. Experiments were designed to define the microstructural parameters controlling the fracture initiation and crack propagation process, and to provide a basis for modelling the fracture process in the ductile-to-brittle transition temperature region in this low carbon, low alloy, ferritic, precipitation hardened steel.

## MICROSTRUCTURAL STRENGTHENING MECHANISMS AND THEIR EFFECT ON MATERIAL TOUGHNESS

Research in quantitative metallurgy has produced great advances in the understanding of the effects of microstructure on the properties of structural steels. Using these quantitative relationships, chemistries and thermomechanical processing can be varied to produce steels with properties for a variety of uses, each maximized for cost efficiency as well as strength and toughness. Microalloyed, precipitation strengthened steels have recently been developed to take advantage of the lower cost and increased weldability afforded by reductions in carbon and other alloy additions. These steels gain their strength through additions of strong carbide and nitride formers which contribute to grain refinement as well as providing a fine distribution of precipitates for strengthening [1,3]. Copper additions also produce a very fine precipitate for strengthening [5], and rare earth additions strengthen inclusions prevent them from elongating during the hot rolling process [8]. Thermomechanical processing parameters can be varied to maximize the effect of these alloy additions on strength and toughness [1].



The equations that have led to the development of high strength, high toughness steels relate microstructural parameters to yield strength,  $\sigma_y$ , ductile-to-brittle impact transition temperature (DBTT) and strain to fracture,  $e_f$  [9]. These include:

$$\sigma_y = \sigma_i + k(d^{-1/2}) + k_1(\text{dispersion}) \quad <1>$$

$$\text{DBTT} = C_1 - k(d^{-1/2}) + k_2(\text{dispersion}) + k_3(\text{pearlite}) \quad <2>$$

$$e_f = C_2 - f_1(\text{vol. fract.})f_2(\text{shape}) \quad <3>$$

where,  $\sigma_i$  = the internal friction stress  
 $k, k_1, k_2, k_3, C_1$ , and  $C_2$  = constants  
 $f_1$  and  $f_2$  = vol. fraction, and shape factors of precipitates respectively [9].

From these equations it is clear that the grain size acts to increase the yield strength and decrease the DBTT, while dispersion, precipitation and solid solution strengthening increase the yield strength to the detriment of toughness and ductility. The effects of grain size and dispersed precipitates on the yield strength are not additive, however. Research by Irvine, Pickering and Gladman [10] has shown that as the effect of one parameter increases, the effect of the other parameter decreases. This is because the yield strength is determined by the mean free path of dislocation travel which is, in turn, determined by the grain size and/or precipitate spacing, and is controlled by whichever is more limiting [11]. Thus, all of these factors

must be combined to optimize both strength and toughness for the particular use for which the steel is being designed.

## GRAIN SIZE STRENGTHENING

### Effects of Grain Size on the Yield Strength

The Hall-Petch equation has been used to describe the relationship between polygonal grain size and the yield strength [11,12] and is given by:

$$\sigma_y = \sigma_i + k_y d^{-1/2} \quad <4>$$

where  $\sigma_y$  = the yield stress,  
 $\sigma_i$  = the friction stress,  
 $d$  = the grain diameter, and  
 $k_y$  = the grain size coefficient,

where  $k_y$  is related to the stress concentration required to activate slip dislocation sources.

More complex versions of the Hall-Petch equation have been proposed for specific alloys by using regression analysis [13] with a 95% confidence limit of  $\pm 31$  MPa. Figure 1 shows the yield stress as predicted by Gladman et al. [9] for a carbon-manganese steel. This figure also shows the large increase in yield strength that can be gained by reducing the ferrite grain size, as well as the contributions made to the yield strength by additions of various alloy elements.

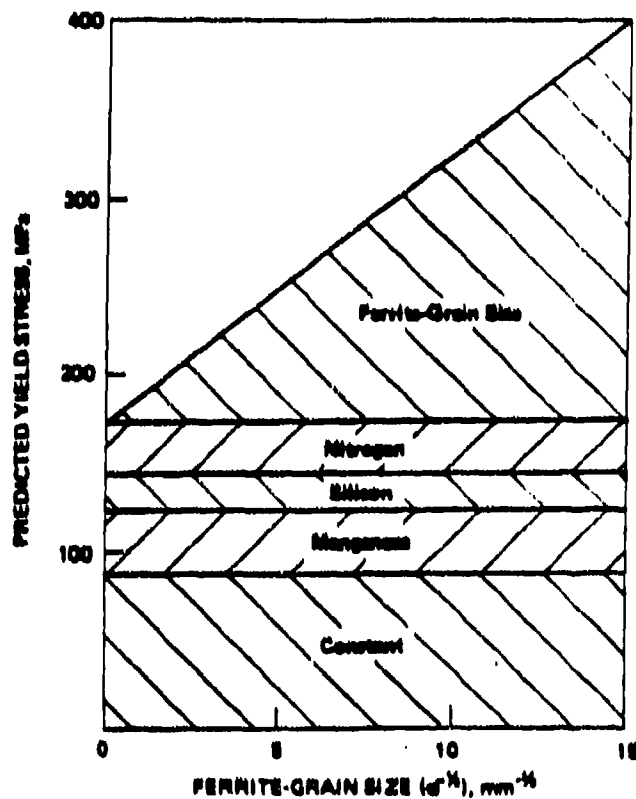


Figure 1. The effects of grain size and alloy elements addition as predicted by Gladman et al. [1].

There are several models which describe mechanisms of grain boundary strengthening as predicted by the Hall-Petch equation. Cottrell's model [14] describes grain boundaries as barriers to slip where yielding is seen to occur when the stresses at the head of dislocation pile-ups at a grain

boundary in one grain are sufficient to nucleate dislocations in the adjacent grain. This stress is given by:

$$\tau_c = (\tau_a - \tau_i) (d/4r)^{1/2}, \quad <5>$$

where  $\tau_c$  is the stress required to activate a Frank-Read source in the adjacent grain,  $\tau_a$  is the resolved shear stress applied on the slip plane,  $\tau_i$  is the friction stress,  $d$  is the grain diameter, and  $r$  is the distance ahead of the shear crack tip. Another model proposed by several researchers [15-19] does not use pile-up theory to describe the yield stress but instead describes the effect of grain size on the yield strength as due to its limiting effect on dislocation density,  $\rho$ , as seen in the experimentally observed relationship that  $\rho$  is inversely proportional to  $d$  [20]. Using this relationship, the equation for the yield stress is given by:

$$\sigma_y = \tau_i + \alpha G b d^{-1/2} \quad <6>$$

where  $G$  = the shear modulus of the material,  
 $b$  = the Burgers vector,  
 $d$  = the grain size,  
 $\tau_i$  = the internal friction stress, and  
 $\alpha$  = a constant (usually 0.3 to 0.6).

A third mechanism describing strengthening due to grain boundaries also does not use dislocation pile-up theory but instead considers grain boundaries as a source of

dislocations. Li's model [21,22] presumed that dislocation ledges on grain boundaries act as sources for dislocations and that the stress to unlock these dislocation ledge sources was inversely proportional to the angle of misfit between adjacent grains. Thus, when the misfit angle between two grain was large, the stress required for dislocation generation from the grain boundary ledges was small. The dislocations generated by the grain boundary ledges form dislocation forests near the grain boundaries with a dislocation density that was proportional to the number of grain boundary dislocation sources and was given by:

$$\rho_f = 8m/\pi d, \quad <7>$$

where  $m$  = the grain boundary ledge density,  
 $d$  = grain size.

Li proposed that the yield stress was the stress required to move dislocations through the dislocation forest and was given by:

$$\sigma_y = \sigma_i + \alpha Gb(8m/\pi)^{1/2}d^{-1/2} \quad <8>$$

where  $\sigma_i$  = the internal friction stress,  
 $\alpha$  = a constant which depends on the dislocation arrangement and is approximately 0.4,  
 $G$  = the shear modulus,  
 $d$  = the grain size, and  
 $b$  = the Burgers vector.

This equation showed that the effect of grain size on yield

strength was due to grain boundary dislocation ledge density. The effect of temperature on the slope of the Hall-Petch equation was determined to be due to the variation in grain boundary ledge structure with temperature.

The dislocation structures formed during the rolling process also play a role in increasing the yield strength. Bramfitt and Marder [23] proposed that since dislocation cell structures act as barriers to slip in a manner similar to grain boundaries, their effect on the yield strength would be similar. They determined the volume fraction of grains versus cells in their material and wrote an equation for the yield stress in which the contribution of each was proportional to its size and volume fraction:

$$\sigma_y = \sigma_i + K[d^{-1/2}(f_r) + d_c^{-1/2}(1-f_r) K_c/K] \quad <9>$$

where  $d$  = the grain size  
 $d_c$  = dislocation cell size  
 $f_r$  = the fraction of recrystallized ferrite,  
 $K$  and  $K_c$  = the experimentally determined values for plots of fully recrystallized structures,  $K$ , and the fully cellular structures,  $K_c$ .

Deviation of experimental data from values predicted using the above equation occurs in partially recrystallized structures, with the above relationship predicting a higher yield behavior due to the local substructure distribution in the ferrite. Figure 2 [24] shows the contribution made to

the yield strength by the various mechanisms described above for a low temperature rolled plate. Some controversy exists as to whether ferrite grain size distribution affects the yield behavior of low temperature rolled steels but, to date there is no experimental evidence that it does.

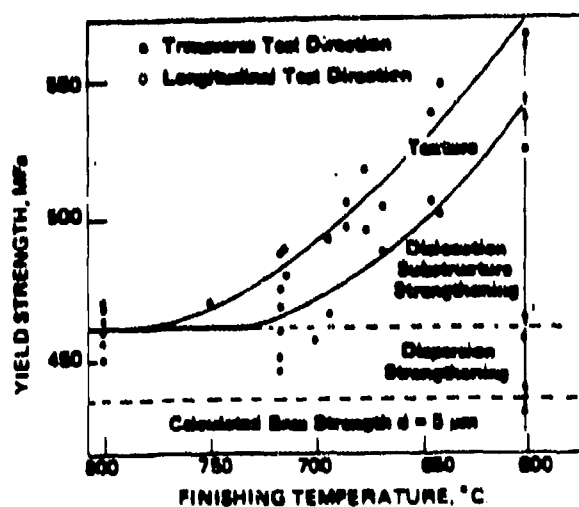


Figure 2. Factors contributing to the strength of controlled-rolled low alloy steel. From Little et al. [24].

## Grain Refinement Mechanisms

The conditioning of austenite during the rolling process is a major factor in determining the strength and toughness properties of rolled steels. Through the use of controlled rolling, the structure, morphology, and grain size of the austenite can be conditioned such that the eventual transformation of the austenite produces the desired ferritic structure to optimize the strength and toughness. Metallurgical changes take place during each stage of the thermomechanical treatment process which affects the responses in subsequent stages as the solutes and particles are repeatedly dissolved and reprecipitated. This sequential processing can give rise to cumulative effects which are very complex in the microalloyed steels.

To understand the mechanisms influencing the properties of hot-rolled steels, the effects of deformation, temperature, and time on recrystallization, precipitation, and transformation have been studied in relation to chemical composition. Composition [25] controls the precipitate solubility and thus, the recrystallization of the austenite. The reheat temperature controls the initial austenite grain size and the solution and precipitation of the microalloy carbides/nitrides [26]. The rolling treatment controls the amount of deformation and recrystallization of the austenite grains, and also the amount of strain induced precipitation



[26].

Grain refinement is desirable because it increases both strength and toughness as shown in equations 1 through 3. Austenite grain refinement can be produced during controlled rolling by two different methods. Type I transformation takes place at higher rolling temperatures where the austenite rapidly recrystallizes and repeated reductions during the rolling process produce austenite grain refinement through successive recrystallization events. The smaller austenite grain size produces small ferrite grains on transformation. Type II transformation takes place at lower temperatures at which austenite recrystallization is inhibited and successive rolling reductions produce a flattened austenitic grain structure, causing refinement by increasing the grain boundary area per unit volume and also by introducing heterogeneities into the austenite in the form of substructures which act as nucleation sites for ferrite during transformation. This increases the number of nucleation events and thus, decreases the size of the ferrite grains nucleated during the transformation process.

Rolling schedules have been designed to utilize deformation over a wide range of temperatures to ensure maximum grain refinement. These usually involve sequential deformation of austenite, above and below the austenite

recrystallization temperature, in the dual phase region of austenite and ferrite and in the ferrite region down to temperatures of about 600°C [24]. This technique of sequential rolling through a range of temperatures produces ferrite with a wide variety of features due to the variation in strain history of each grain. These features may include [9]:

- (a) disparity in ferrite grain size and shape;
- (b) dislocation substructures comprised of either cells, or random arrays, or both;
- (c) a crystallographic texture, and;
- (d) a wide range of carbide/particle sizes resulting from strain induced precipitation and spheroidization.

Alloying additions play a role in decreasing the austenite grain size by pinning austenite grain boundaries. When a grain boundary intersects a particle, grain boundary area is eliminated because the particle now makes up part of the grain boundary and thus the grain boundary energy is reduced. Any movement of the grain boundary away from this particle (i.e. during grain growth) results in an increase in the local grain boundary energy. The critical particle radius for effective pinning of the grain boundary is given by [27]:

$$r_{crit} = (6\bar{R}_0 f) / \pi (3/2 - 2/Z)^{-1} \quad <10>$$

where  $r_{crit}$  = the maximum size of the particle that will effectively counteract the driving force for grain growth,

$f$  = the volume fraction of particles in the microstructure  
 $\bar{R}_0$  = the matrix grain radius  
 $Z$  = the ratio of the radii of the growing grain to the matrix grains.

Thus, at some critical particle size, the driving force for grain growth equals the pinning force. Further growth of the particles results in less effective grain boundary pinning. Therefore, a fine particle size is more effective at inhibiting grain growth.

Alloy additions are chosen to produce a fine, well distributed precipitate at the thermomechanical treatment temperature. Since particle coarsening is proportional to the alloy element content in equilibrium with its carbide/nitride [28], it is important to know the solubility limits of these elements. Common grain refining alloy additions are aluminum and vanadium, which form nitrides of limited solubility, niobium, which forms a carbonitride, and titanium which forms both a carbide and a nitride [9,21,25,26]. Studies by Irvine et al. [10] have shown the solubility limits for these alloys in iron to be:

$$\begin{array}{ll}
 \log_{10} [Al] [N] = -6770/T(^{\circ}K) + 1.03 & <11> \\
 \log_{10} [V] [N] = -8330/T(^{\circ}K) + 3.46 & <12> \\
 \log_{10} [Nb] [C] = -6770/T(^{\circ}K) + 2.26 & <13> \\
 \log_{10} [Ti] [C] = -7000/T(^{\circ}K) + 2.75 & <14>
 \end{array}$$

where  $[X]$  is the dissolved solute and  $[C]$  and  $[N]$  are the dissolved carbon and nitrogen contents expressed in weight percent. The niobium can form niobium carbides with a high

carbon content or the carbon can be replaced by the sum of the carbon and nitrogen contents [10].

Silicon and phosphorous have been found to counteract the grain refining effects of fine distributions of carbides and nitrides [10]. These elements act as ferrite stabilizers, raising the temperature at which ferrite is formed which thus limits the amount of austenite conditioning that can occur during rolling and allows more ferrite grain growth, resulting in larger ferrite grains.

Alloy additions affect the recrystallization behavior of the austenite by increasing the temperature at which complete recrystallization occurs [29], thereby increasing austenitic grain refinement at a given temperature. Solute content also tends to raise the grain coarsening temperature due to a solute drag effect on the growth of austenite grain boundaries [30-32]. Niobium, when added in small amounts ( $<0.1\%$ ), is extremely effective in strengthening steels without a substantial reduction in toughness due to its ability to readily form precipitates with carbon and nitrogen. In small amounts it acts as an austenite stabilizer. Niobium is thought to cause either a solid solution effect [33] or a strain induced precipitation which stabilizes the substructure in the deformed austenite [34].

Research has shown [35-40] that the response of a

steel to a given thermomechanical treatment is closely related to the kinetics of dissolution and reprecipitation of niobium carbonitrides, vanadium nitrides, aluminum nitrides, and titanium carbides and nitrides in austenite since these particles act to retard the recovery and recrystallization of austenite during, and subsequent to, deformation. One of the primary requirements of a successfully conditioned austenite is the presence of a large number of crystal defects that can act as sites for ferrite nucleation during cooling. Niobium (or vanadium, aluminum, or titanium) can be added to restrict the motion of these subgrain and grain boundaries after hot deformation in order to maintain the large effective austenite interfacial area per unit volume created during the rolling process by elongating the austenite grains. Increasing the grain boundary area increases the number of sites available for ferrite nucleation and leads to refinement of the ferrite grains because the small thickness of the "pancaked" austenite grains puts an effective upper limit on the size of the resulting ferrite grains, enhancing both strength and toughness properties.

Studies by Wilson and Gray [41,42] have shown that low transformation temperatures promote finer ferrite grains, larger increments of precipitation hardening and higher yield strengths. Accumulation of strains below the austenite recrystallization temperature increases the

austenite-to-ferrite start temperature while also increasing the number of sites available for ferrite nucleation. Thus, it is clear that the exact transformation conditions will depend on a balance between the competing factors of solution, reprecipitation, recovery, recrystallization and grain refinement.

#### Effects of Grain Refinement on Toughness

Grain size reduction increases the yield strength while decreasing the DBTT as shown in equation <1>. Regression analysis done by Gladman [9] on a carbon-manganese steel, has shown the relationship between grain size and DBTT to be  $-11^{\circ}\text{C}$  per unit increment in  $d^{-1/2}(\text{mm}^{-1/2})$  while each unit increment in grain size increases the yield strength by 15 MPa. The method used for grain refinement is important because not all methods have the overall effect of increasing strength while decreasing the DBTT. To increase yield strength while decreasing, or at least maintaining the DBTT, the most effective method for grain size reduction is the use of thermomechanical processing. When a low reheat temperature is combined with a low rolling temperature and a fast cooling rate, a small grain size with a fine distribution of precipitates results, which gives good strength and toughness properties [10].

High angle boundaries increase strength and toughness

because they act as barriers to crack propagation, while low angle boundaries contribute to strength because they act as barriers to slip, but are detrimental to toughness because they do not inhibit crack propagation [9].

#### PRECIPITATION AND DISPERSION STRENGTHENING

Dispersion strengthening arises from a fine distribution of insoluble, incoherent, second phases, such as oxides, carbides, and nitrides, in a metallic matrix. Dislocation motion through the matrix occurs by the dislocations bending to a radius which allows them to move between the particles. The stress to bend the dislocation is determined by the interparticle spacing [43].

Precipitation strengthening is produced by a fine distribution of a second phase in which the solute atoms exhibit decreasing solubility in the metal matrix with decreasing temperature. Precipitation strengthening results when a metal, with the second phase atoms in solution, is quenched, and then given an aging treatment to precipitate the second phase. In high strength, low alloy carbon steels copper precipitates have been used to produce strengthening instead of carbon [44]. It has been suggested [45,46] that in the underaged condition, when these copper precipitates first nucleate in the ferrite matrix, these precipitates are

coherent with the bcc ferrite matrix. Upon further aging these copper-rich precipitates grow and transform to an incoherent fcc structure [45,46]. The critical particle size for coherency is believed to be approximately 2.5 nm. In the overaged, incoherent stage strengthening by these copper precipitates may be caused by a combination of coherency strains and Orowan strengthening [45-47] as will be described later.

The Hall-Petch equation applies only for materials that obtain their strengthening through the direct effects of lattice friction, solute atoms and grain boundaries [48]. For precipitation hardening alloys Hall-Petch predictions of the yield strength fall below measured properties. To determine how best to predict the effects of precipitates on the yield strength of a steel, it is necessary to consider mechanisms of precipitation strengthening. There are several different models dealing with precipitation strengthening which vary in the assumed particle distribution and in the mechanism by which dislocations overcome obstacles/precipitates.

#### Strengthening Through Particle/Dislocation Interactions

Precipitates act to increase the yield stress by creating an obstacle for dislocation motion. This occurs in one of two ways. If the precipitate is coherent the



dislocation can cut through it, but requires a stress much greater than that required for the dislocation to move through the matrix [43]. If the precipitate is incoherent and relatively strong, it acts as an impenetrable obstacle which the dislocation can move past only by changing shape. For particles which can be sheared by dislocation passage, strengthening arises from the matrix strain resulting from any mismatch between the particle and matrix, including elastic moduli mismatch, the increase in surface area of the particle caused by passage of the dislocation, and the work done to move the dislocation through the particle [43].

In the 1940's Mott and Nabarro developed a solid solution strengthening theory which considered the internal stress created by misfitting solute atoms which had to be overcome before a dislocation could move through the lattice [49]. They divided obstacles to dislocation motion into two categories; diffuse, and localized. Diffuse obstacles were those which could interact with dislocations from a distance because of the strain they created in the matrix surrounding them due to coherence or atomic misfit. Localized obstacles were those which could only affect dislocation motion when they were in direct contact with the dislocation.

Mott [50] solved the problem of a single dislocation interacting with attractive obstacles at a zero applied stress and assumed that all obstacles on a glide plane had

equal strengths. He determined that, when a dislocation interacted with an obstacle, the dislocation would assume a zig-zag configuration with the amplitude determined by the effective obstacle spacing,  $L$ . This solution is based on minimizing the energy of the dislocation.

The Mott/Nabarro theory was also found to hold for soft precipitates of a second phase since these act as diffuse obstacles. They determined that the yield stress was dependant on the magnitude of the internal stress and the mean wavelength over which it fluctuated. The wavelength, which was found to be equal to the separation of solute atoms,  $L$ , was determined in relation to the radius of curvature,  $R$ , to which the internal stress,  $\tau_i$ , was able to bend a dislocation. This curvature was given by:

$$R = \frac{T}{b\tau_i} = \frac{\alpha Gb}{\tau_i} \quad <15>$$

where the tension,  $T$ , equaled  $\alpha Gb^2$  with  $\alpha$ , a constant approximately equal to 1,  $b$ , the Burgers vector, and  $G$ , the shear modulus. For increasing coarseness of the dispersion of solute atoms or precipitates, three regimes were distinguishable: (a)  $L \ll R$ , (b)  $L \approx R$ , (c)  $L \gg R$ .

For  $L$  much less than  $R$ , which is typical of solid solutions, Mott and Nabarro determined that a dislocation could not bend around each individual stress center due to the high density of solute atoms, but followed a line which

minimized the sum of the inherent elastic energy and the potential energy of the dislocation due to interaction with the stress field. Forward motion of the dislocation occurred when a section of the dislocation, several times larger than the inter-solute atom spacing, jumped into the next equilibrium position. The increase in yield stress due to the effect of solute atoms on dislocation motion was calculated as:

$$\Delta \sigma_y = 2.5G \epsilon^{4/3} c \quad <16>$$

where  $c$  is the atomic concentration of solute atoms and  $\epsilon$  is the atomic misfit of the solute atoms with those of the matrix given by the dimensionless parameter:

$$\epsilon = (r_b - r_a)/r_a \quad <17>$$

where  $r_b$  is the atomic radius of the solute atom and  $r_a$  is the radius of matrix atom.

For  $L$  approximately equal to  $R$ , which represents a precipitation-hardened alloy at maximum hardness, Mott and Nabarro [46] found that a dislocation was able to bend around individual stress centers and a section length  $X = L$  moved forward independently. The increase to the yield stress due to dispersion strengthening was determined to be:

$$\Delta \sigma_y = 2G\epsilon c. \quad <18>$$

Finally when  $L$  is much larger than  $R$ , which represents a dispersion strengthened material, a dislocation moves

forward by passing between obstacles leaving a closed dislocation loop behind. This mechanism was suggested by Orowan in 1947 [51] to describe strengthening of alloys by non-deformable particles. The increase in yield stress due to particle "pinning" of a dislocation was determined to be given by:

$$\Delta\sigma_y = \frac{2Gb}{L} \quad <19>$$

The stress to move dislocations between particles increases as each dislocation leaves a loop around the particles it has passed which exert a back stress on other dislocations in the slip plane. This mechanism of dislocation motion causes rapid strain hardening of the matrix. The Ashby-Orowan model [52] is the most widely accepted model of dislocation cutting because it incorporates the random particle spacing distributions of Kocks [53] which is probably the most realistic distribution. Taking this random distribution into account, the stress required to bow a dislocation out between neighboring particles becomes:

$$\tau = (0.16Gb/L) [\ln(\bar{x}/2b)] \quad <20>$$

where:

- $\tau$  = the resolved shear stress required to move a dislocation past the precipitate,
- $\bar{x}$  = the mean planar intercept diameter of the precipitate,
- $L$  = interparticle spacing

G = the shear modulus (which is 80300 MPa for ferrite) [9]  
 b = the Burgers vector (which is  $2.5 \times 10^{-10}$  m for ferrite) [9].

For ferrite this reduces to:

$$\tau \text{ (MPa)} = (2.2 \times 10^{-6}/L) \ln(\bar{x}/5.0 \times 10^{-10}) \quad <21>$$

where L and x are measured in microns. Assuming that the tensile stress is two times the resolved shear stress, as given by the Tresca equation [54], the strengthening due to dislocation bowing between particles becomes:

$$\Delta \sigma_y \text{ (MPa)} = (6.4 \times 10^{-6}/L) \ln(x/5.0 \times 10^{-10}) \quad <22>$$

Figure 3 [9] shows the relationship between precipitate strengthening and volume fraction of precipitates as described by the Ashby-Orowan model. This mechanism of strengthening also results in the formation of a dislocation cell structure created by the tangles of dislocations around the particles. This dislocation structure contributes to the Hall-Petch strengthening as described earlier.

As shown in Figure 3, the strengthening increment is inversely proportional to precipitate size, indicating that a fine dispersion of precipitates is most desirable for high strength. The dispersion strengthening due to carbides and nitrides depends on the heating cycle which governs the amount of niobium/titanium/aluminum taken into solution and the cooling cycle which controls the precipitation of the

carbides and nitrides.

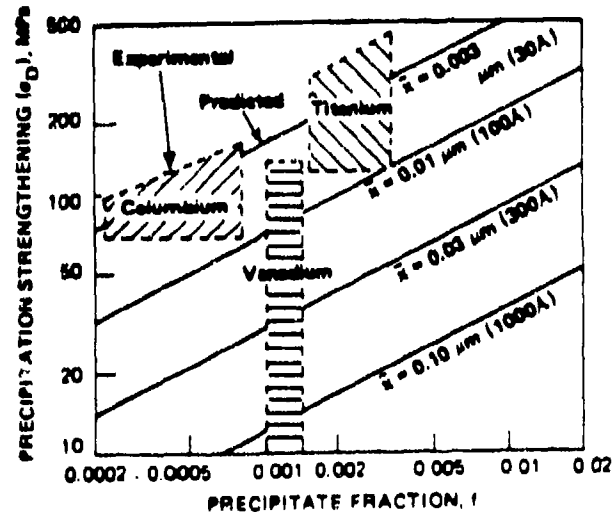


Figure 3. The dependence of strengthening on precipitate size and volume fraction as predicted by the Ashby-Orowan model. From Gladman et al. [9].

#### Effects of Alloy Additions on Precipitation Strengthening of Steels

Alloying element additions act in a variety of ways to strengthen steel [1-5,8]. Manganese and nickel are desirable for solid solution strengthening because they

increase strength while at the same time decrease the DBTT [55]. Niobium contributes to grain refinement by stabilizing austenite in the thermomechanical processing temperature range and contributes to precipitation strengthening [25,26,29,56]. Molybdenum increases hardenability, thereby lowering the austenite-to-ferrite transformation temperature and as a result further refines the grain size [55] while small additions of manganese act to decrease the DBTT by eliminating grain boundary carbide films [57].

Copper alloy additions act to strengthen iron in one of three ways; (a) the copper particles do not shear during plastic deformation and the strengthening effect is given by the average spacing of the particles, b) the particles cause coherency stresses in the matrix and inhibit the motion of dislocations, or c) the zones or particles are sheared and the strengthening is given by the energy necessary for a dislocation to shear a particle or zone [58].

Free nitrogen is detrimental to impact properties but Pickering et al. [10] have found that aluminum additions up to 0.2% reduce impact transition temperature by tying up the free nitrogen. When larger amounts of aluminum are present there is a solid solution hardening effect which is detrimental to impact properties [10].

Manganese-sulfides inclusions can take on extreme aspect ratios (1000/1 being common) due to their plasticity at all steel deformation temperatures [59]. Sulfides usually precipitate in conjunction with oxide compounds [59,60].  $\text{Al}_2\text{O}_3$  and calcium aluminates are also detrimental due to their brittle nature. Dendritic oxides tend to break during hot rolling at strains of about 0.4 and disseminate as stringers, while spherodized oxides require strains exceeding 1.5 for fracture [59]. The use of calcium as a desulphurizer and as a sulfide shape-control agent means that calcium aluminates can form before and during the solidification process. These are harmful because their coefficient of thermal expansion is much lower than that of steel [9,10,59]. Silicate inclusions are intermediate in behavior between the easily deformed sulfides and the refractory oxide compounds. They are readily deformed at temperatures above  $900^\circ\text{C}$  but below  $700^\circ\text{C}$  they are very brittle. Rare earth additions are made to eliminate alumina and Mn-sulfides [59]. Figure 4 shows the effects of various alloy additions on the strength of controlled-rolled, low alloy steel.



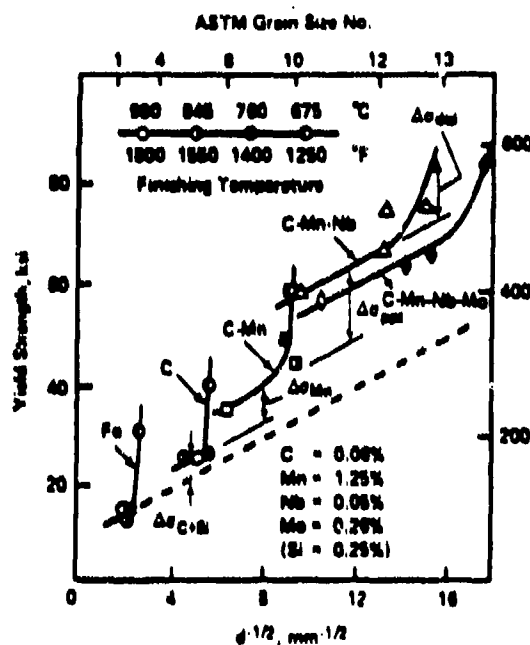


Figure 4. The effects of alloy elements on the strength of controlled-rolled low alloy steels [57].

#### Effects of Precipitates and Inclusions on Toughness

Free nitrogen and carbon are detrimental to toughness as are alloy additions which are in solid solution with the iron, so alloy additions must be carefully made to tie up these elements as stable nitrides and carbides [10].

Aluminum can be added to form stable nitrides but the precipitation kinetics of aluminum nitrides are such that they do not form a fine precipitate on cooling from austenite. Fine niobium carbides increase the DBTT by approximately 0.3 to 0.5 °C for each 1 MPa increase in yield strength brought about by precipitation strengthening [29,60]. This ratio of change in DBTT to change in  $\sigma_y$  is subject to the unpredictability of impact properties, especially in the transition region, so changes in DBTT with alloy addition may be real or they may be a consequence of statistical error. Titanium forms nitrides which are very stable even at high temperatures. Consequently, large cuboid titanium nitride particles are common. Silicon and phosphorous are also detrimental to toughness since they tend to form large, brittle inclusions [59]. Those elements which are responsible for large increases in the yield strength also tend to have the largest detrimental effect on brittle fracture behavior [9,10,59]. Bainite has also been shown to be detrimental to the DBTT, even when only small amounts of it exist within the polygonal ferrite matrix [9].

Inclusions have an effect similar to precipitates on strength and toughness properties. The important parameters used to describe inclusions in relation to strength and toughness are their aspect ratio and the volume fraction. Inclusions have a greater effect on the upper shelf impact

energy than they do on the transition temperature although debonding of the inclusion from the matrix relaxes the stress triaxiality and increases the likelihood of ductile fracture.

Inclusion shape plays a role in toughness, with spherical inclusions promoting a higher toughness behavior than elongated inclusions. Inclusion shape can be modified by additions of titanium, zirconium and rare earth elements which act to reduce the plasticity of the inclusion at the rolling temperature, making them less easily deformed. Figure 5 shows the effects of alloy additions on the ductile-to-brittle transition temperature of low alloy steels.

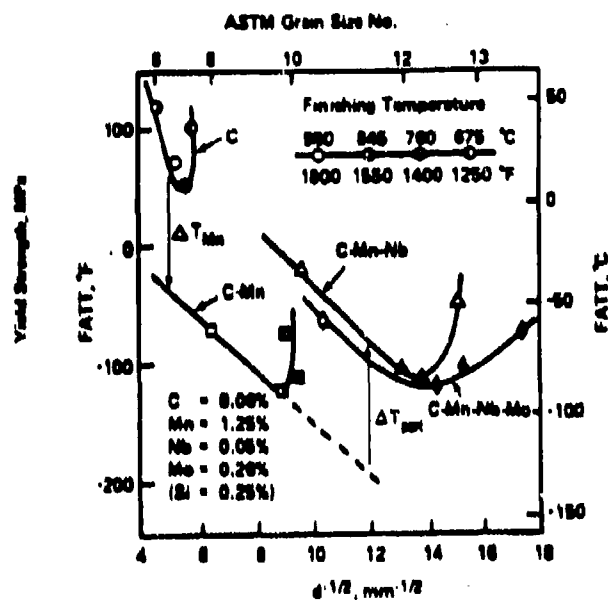


Figure 5. The effects of alloy element additions on the ductile-to-brittle transition temperature in controlled-rolled, low alloy steel [57].

Alloy additions are constantly being decreased in structural steels in efforts to decrease the cost of production of these steels and fabrication of structures using these steels [56]. More emphasis is being placed on thermomechanical processing parameters to most effectively utilize the alloying elements that are added to increase the limits of the strength and toughness properties of these steels. New processing techniques and better control of

processing parameters have allowed the reduction of grain size to several microns in diameter and less. At these small grain sizes, the effects of grain boundary area may become as important, or possibly more important, than precipitation strengthening as they start to control the mean free path of dislocation travel in the ferrite. When the grain size plays a large role in strength and toughness, it becomes important to have a complete understanding of the effects of grain size distribution on these properties. To date, thermomechanical processing has been developed to a point where grain size homogeneity can be maintained in plates with thicknesses to 25.4 mm. However, plates of greater thickness have shown large heterogeneities in grain size distribution with large volume fractions of relatively large grains [61]. These large grains are not accounted for in the equations described above for grain size/strength/toughness relationships.

## THE BRITTLE FRACTURE OF STEELS

Because the primary goals of metallurgy are to provide strong, tough, engineering materials, it must be concerned with the problem of brittle failure. Cleavage fracture is characterized as a low energy, fast, unstable fracture mode which can be described in terms of a critical stress criterion for failure [62]. That is; cleavage failure will occur if some critical stress,  $\sigma_c$ , is exceeded. In most cases cleavage failure occurs when the applied stress is much lower than the theoretical fracture stress of the material due to internal, often microscopic, flaws. A plane strain fracture toughness parameter,  $K$ , is used to describe the magnitude of the crack-tip stress field at the initiation of crack extension for a particular opening mode assuming a homogeneous, linear elastic material.  $K_{IC}$  is the critical value of  $K$  which characterizes the ability of a material to resist fracture in the presence of a sharp crack under an applied load and can be used to estimate the relationship between defect size and failure stress for materials in service [63].

The physical significance of  $\sigma_c$  and  $K_{IC}$  and the importance of their use in material and structural design applications can only be understood through a thorough study of cleavage fracture mechanisms. Even though studies of

fracture mechanisms in steels have been conducted on for decades, the recent advent of new, clean steel technology and the complexity of new steel alloys requires that more work be done in this area to provide a complete understanding of cleavage fracture mechanisms which would then provide the basis for improvements in the fracture toughness and strength of structural steels. Previous models of the cleavage fracture process describe fracture in high carbon, high alloy, relatively large grained materials. Steel technology has advanced considerably in the last decade with advances in processing which allow production of very low alloy steels and a reduction of carbon to 0.02% while still maintaining strength through thermomechanical and composition control of grain size. At these low alloy contents and small grain sizes, microstructural features other than those described for higher alloy steels may play primary roles in determining strength and toughness. Thus, there is a great need to understand how processing advances have affected the fracture process, especially the cleavage fracture process, of steels.

Cleavage fracture occurs in two stages: nucleation of a sharp cleavage crack, usually at some microstructural inhomogeneity such as a particle or grain boundary, and the subsequent growth of that crack.  $\sigma_c$  is determined by the most difficult of these stages. Early work centered on the

discrepancy between the theoretical fracture strength of a material and its actual fracture strength, which often varied by a factor of ten or more. Griffith [62] determined that flaws must exist in materials resulting in local regions of high stress concentrations which depended on the shape of the flaw and its orientation to the applied stress. Failure of the material would then occur under conditions which caused the crack to extend. He based his arguments on the principle that crack propagation would occur when crack growth resulted in a lowering of the free energy of the system. In analyzing the energy balance of the system, Griffith considered two types of energy; the surface energy of the newly created crack surfaces and the strain energy of the system caused by the applied load. The surface energy increases with crack growth while the strain energy is decreased by relaxation of the stress in the material on either side of the crack. Griffith hypothesized that a crack will grow when relaxation of the strain energy is greater than the energy required to create two new surfaces. Thus, for a given normal tensile stress, Griffith found that the condition for crack propagation was achievement of a critical crack size as given by [62]:

$$a_c = \frac{2E\gamma_s}{\pi(1-\nu)\sigma^2} \quad <23>$$

for the plane strain condition, where:

E = Youngs modulus



$\gamma_s$  = crack surface energy  
 $\nu$  = Poissons ratio  
 $a_c$  = crack length  
 $\sigma$  = the normal tensile stress.

Griffith's conclusion that flaws exist in materials prior to failure spurred research into how these flaws or cracks came into existence. Zener [64] described crack formation as a separation of atoms which occurs at slip band/particle or grain boundary intersections due to the stress concentrations in these areas. He used dislocation theory to describe crack initiation as a process which occurs by dislocation coalescence due to strain localization at particles or grain boundaries which act to impede dislocation motion. Thus, he hypothesized that cleavage fracture could not occur independently of deformation since plastic flow was required to increase the strains at particles or grain boundaries needed for crack initiation. Once these cracks were initiated, Zener proposed that further relaxation of the shear stresses in the slip band, as given by the Griffith equation, would act as a driving force for crack propagation, and propagation would continue until all of the shear stress in the slip band had been relaxed. If the crack had a very high stress concentration (from attaining the critical size described in the Griffith equation) with respect to the applied stress then it could become self-propagating and the crack would extend not only throughout the region of high stress

concentration of the slip band but would also propagate under its own stress concentration.

Through review of several experiments that were done to determine the flow and fracture stress of various materials, [65-67] Zener determined that plastic flow was essential to fracture and that enough plastic flow would always occur, even under highly embrittling conditions, to initiate a microcrack. He also determined that the maximum normal component of the stress necessary to produce the first slip was a function of temperature and stress state with the stress concentration factor proportional to the length of the slip path, i.e. the grain size for a simple polycrystal.

Stroh [68] also thought it unlikely that pre-existing cracks played an important part in the fracture of metals and thus thought it necessary to consider how cracks might be produced in a material. Using Mott's [69] suggestion that the stress concentration at the tip of a dislocation pile-up was sufficient to create a crack, he considered the conditions under which a crack would form. Considering only stresses which were normal to the crack and considering that the formation of a crack must be accompanied by a decrease in the energy of the system, Stroh used the dislocation array studied by Eshelby, Frank and Nabarro [70], with a unit length given by;

$$L_n = Gb/4\pi (1 - \nu) \sigma_0, \quad <24>$$

to determine the conditions under which a crack of length  $r$  would form where  $G$  is the shear modulus,  $b$  is the Burgers vector,  $\nu$  is Poissons ratio, and  $\sigma_0$  is the yield stress. He found the crack initiation condition to be satisfied when;

$$n\sigma_0 > 12\alpha G \quad <25>$$

where  $n$  is the number of dislocations, and  $\alpha$  is a constant.

Taking  $\alpha = 0.06$ ,  
 $\sigma_0 = 10^8$  Pa, and  
 $G = 10^{11}$  Pa,

this equation describes crack formation for dislocation pile-ups which contain approximately 1000 dislocations. For a Burgers vector of  $b = 2 \times 10^{-10}$  m, this equation gives a critical crack length of  $10^{-4}$  m which Stroh thought large enough to propagate by the Griffith mechanism, producing immediate fracture of the material. However, the dislocation pile-up model assumed by Stroh was an over simplification of the dislocation structures actually observed in materials and, thus, the stresses calculated using this model are probably much higher than actual grain boundary stresses. In his calculations of the stresses due to the crack, Stroh assumed that once the crack was formed, the  $n$  dislocations of the pile-up would enter the crack such that the extra material at one end would wedge the crack open giving a roughly triangular shape. The result of this

work was the suggestion that the condition for notch brittleness was that all of the dislocation sources were locked such that they could not respond fast enough to inhibit crack formation and growth through plastic flow. With crack growth thus unimpeded, the crack could spread through the material causing brittle failure. Stroh found that dislocation pile-ups at grain boundaries did not always result in failure of the material. In some cases the stresses at the head of the pile-up generated slip in an adjacent grain instead, and what remained unclear was the conditions determining the mechanism of stress relief at the grain boundary.

Cottrell [71] suggested another mechanism of crack nucleation by dislocation coalescence in which dislocations were attracted to each other instead of being forced together by the stresses of the dislocation array behind them as suggested by Stroh [68]. Cottrell presented a scenario in which a crack is formed at the junction of two intersecting slip planes by the coalescence of partial dislocations. He described this process as:

$$\frac{a}{2} [\bar{1}\bar{1}1] + \frac{a}{2} [111] > a[001] \quad <26>$$

The coalescence of the two partial dislocations lowered their elastic energy and this lower energy was seen as the driving force for their coalescence. The  $a[001]$

dislocation produced in this manner was a pure edge dislocation which lay in the cleavage plane, thus producing a microcrack. Using a procedure worked out by Stroh [72], Cottrell calculated the breaking stress of a perfect crystal in the presence of an isolated wedge of length  $nb$ , to be:

$$\sigma_f = \frac{2\gamma}{nb} \quad <27>$$

with  $\gamma$ , the specific surface energy,  $n$  = the number of coalesced  $a[001]$  dislocations, and  $b$ , the Burgers vector. At this early stage the applied stress did not act directly on the microcrack but influenced it by the force exerted on the dislocations moving into the crack. As the crack grew the influence of the applied stress at the crack tip became the predominant factor in crack growth.

Hahn and Rosenfield [73] analyzed the work done by Cottrell and found that the number of dislocations calculated by Cottrell to be involved in the pile-up were 20 times greater than values predicted in other models. They examined the possibility that this discrepancy was due to an incorrect determination of the number of coalesced dislocations. Cottrell had assumed that all of the dislocations in an array coalesced but Hahn and Rosenfield suggested, instead, that the number of dislocations in the wedge could be estimated by regarding all of the

dislocations at the head of the array, whose average spacing in the x-direction was equal to the  $a[100]$  Burgers vector, as coalesced. This led to;

$$n_b = 4.95 N \left( \frac{\tau}{G} \right)^{1.56} \quad <28>$$

as the number of coalesced dislocations, where  $\tau$  = the effective shear stress,  $G$  = the shear modulus, and  $N$  = the length of the dislocation array. Hahn and Rosenfield concluded that the smaller number of coalesced  $a\langle 100 \rangle$  dislocations derived from the dislocation spacing at the head of a pile-up led to values of  $\tau_f$  which were orders of magnitude larger than predicted by Cottrell.

Grain boundaries act as barriers to slip and thus, as found by Zener, are often sites of high strain localization and crack initiation. Using half the grain diameter as the maximum length of a dislocation array, Petch [12] studied the effects of grain size on the cleavage fracture strength of steels. He used Koehlers [74] calculation of the tensile stress intensification due to dislocation arrays to establish the cleavage strength/grain size relationship by determining the relationship between  $n$ , the number of dislocations in an array of like dislocations and  $d$ , the grain size. To do this he assumed that below the yield stress, dislocations did not cross grain boundaries and, thus, the maximum value of  $n$ , the number of dislocations

generated under a stress,  $\tau$ , could be calculated. Using equations determined by Eshelby, Frank and Nabarro [70] for the length of an array of like dislocations, Petch found that the internal stress could be represented by an average shear stress independent of, and in opposition to  $\tau$ , given by:

$$\sigma = \frac{\alpha}{4A} (\tau - \tau_i)^2 d \quad <29>$$

$\tau$  = the applied stress  
 $\tau_i$  = the internal friction stress  
 $\alpha$  = a constant  
 $A = Gb/2\pi(1-\nu)$   
 $d$  = grain diameter.

In terms of the tensile stresses,  $\sigma$  and  $\sigma_i$ , corresponding to  $\tau$  and  $\tau_i$ , and taking  $\sigma = \sigma_f$ , the cleavage stress, a rearrangement of the above equation produces;

$$\sigma_f = \sigma_i + kd^{-1/2} \quad <30>$$

the cleavage strength/grain size relationship assuming no plastic deformation, where  $k$  is the grain size coefficient. Petch concluded that the cleavage strength of polycrystals was controlled by the theoretical cleavage strength in the vicinity of the grain boundaries, and that  $\sigma_i$  and the grain size determined the magnitude of the stress concentration at the grain boundary. This model of cleavage fracture assumed that there were no precipitates acting as stress concentrators within the grains.

Low [75] also studied the microstructural dependence of cleavage fracture in BCC polycrystalline materials, concluding that the Griffith equation, which requires that only surface energy be provided for spontaneous crack propagation, did not hold well for polycrystalline materials. Low looked at secondary cracking in thin sheets of low carbon, rimmed steel, tested at  $-195^{\circ}\text{C}$ , that had been polished and etched to reveal the underlying microstructure. He discovered that many of the secondary cracks had been arrested at unfavorably oriented grain boundaries with considerable plastic deformation apparent at the crack tip. Because of this plastic deformation which was required to propagate a crack into an unfavorably oriented grain, Low found that his results agreed with the equation proposed by Orowan [76] for the critical stress for crack propagation in which a plastic work term was substituted for the surface energy term;

$$\sigma_c = \sqrt{\frac{2E\gamma_p}{\pi(1-\nu^2)a_c}} \quad <31>$$

Thus, Low concluded that stress must exceed some critical value which depended on  $E$ ,  $\nu$ , and the energy absorbed in forming two new crack surfaces,  $\gamma_p$ . He also concluded that the smaller the unit of microstructure which limits the size of the first microcrack, the greater the materials



resistance to brittle fracture. Thus, he postulated that small grain sized materials, or those with a finely dispersed precipitate structure, should be tougher than materials containing large grains and coarse particles, and would exhibit a lower DBTT. This agreed closely with the conclusions of Patch [12].

Stroh [77] examined the temperature dependence of the ductile-to-brittle transition behavior of materials. He proposed that a material would behave in a ductile or brittle manner depending on whether the stresses around a pile-up operated a nearby dislocation source in an adjacent grain or initiated a crack. He postulated that stresses around a dislocation pile-up would cause a Frank-Read source to operate by liberating it from its locking impurities, unless the stresses required to free the dislocation sources were greater than the cleavage fracture stress. If this was the case, Stroh postulated that cleavage cracks would initiate and propagate to relieve the stresses and brittle fracture would occur. He explained the temperature dependence of this behavior by associating thermal fluctuations with the freeing of the dislocation source from its locking atmosphere. High temperatures produced the energy required to free dislocation sources and thus favor ductile behavior while lower temperatures depress thermal fluctuations and decrease the energy available to unlock the

dislocation sources, thus favoring brittle behavior.

Zener [64] advanced the idea that particles, which act to block dislocation movement on slip bands, were similar to grain boundaries in that both act as stress raisers which are capable of initiating cracks. McMahon and Cohen [78] studied cleavage crack initiation sites in low carbon steels to determine the role played by carbides and grain boundaries in the crack initiation process. They identified the origin of cleavage cracking on the fracture surface as well as looked at non-propagating secondary cracks adjacent to the main crack in polished and etched profiles of the fracture surface. Their results showed that even in the very low (0.007%) carbon steels the cementite particles in the ferrite matrix were responsible for initiating cleavage cracking. The mechanism they suggested to describe this process was that plastic deformation occurred in the ductile ferrite matrix before it could occur in the brittle cementite particle creating strain localization at the cementite/ferrite interface. This strain localization set up large enough stresses at the interface to cause crack initiation in the cementite which could then propagate as a Griffith crack across the cementite particle. When the crack reached the carbide/ferrite boundary it was either arrested, if the ferrite could deform to relax the stress, or it continued as a Griffith crack across the ferrite grain. Cleavage of the ferrite occurred either at the

instant the carbide crack reached the carbide/ferrite interface or not at all, which was supported by experimental evidence [78].

In further studies, McMahon and Cohen [79] concluded that the cracking of carbides was the primary source of cleavage microcracks when the specimen underwent general plastic deformation and that the critical event in the cleavage fracture process was the propagation of the carbide particle sized microcrack into the ferrite matrix. The probability of ferrite cleavage resulting from the carbide crack increased with increasing carbide thickness and decreasing temperature. They found that barriers to microcleavage propagation included, in order of decreasing effectiveness; grain boundaries, preexisting mechanical twins, and initiation of slip bands and/or twins at the tip of the advancing crack. They also found that the statistical distribution of crystallographic orientations of the grains contributed to the propagation process, with propagation being enhanced in regions having an alignment of favorable cleavage paths.

Describing the critical event in the cleavage fracture process as the propagation of the carbide crack into the surrounding ferrite matrix instead of crack nucleation suggested that the effective fracture surface energy was increased above the free surface value as the crack grew

across the grain. Cottrell [71] and Petch [12] calculated the stress required for a crack to propagate across a grain and compared that stress with the yield stress to derive a criteria for the ductile-to-brittle transition. The value of the fracture surface energy determined from this method was higher than the free surface energy for ferrite but no mechanism was proposed for this increase.

Smith [80] proposed that the increase in the effective work to fracture was due to the appreciable plastic deformation that accompanied crack propagation in the ferrite matrix, except at very low temperatures. Smith also felt that cleavage crack propagation from the carbide into the surrounding ferrite matrix was the critical step in the cleavage process and thus proposed that carbide thickness was the controlling microstructural parameter of cleavage fracture. He studied cleavage fracture in two steels in which the only difference was carbide particle thickness. He proposed a model in which the inhomogeneous plastic deformation in the ferrite nucleated a cleavage crack in the brittle carbide particle which spread across the particle with an effective surface energy equal to the free surface energy of the particle due to its inability to deform. The ferrite matrix was then presented with a sharp crack of length equal to the carbide thickness, and would propagate the cleavage crack if the crack tip stresses were high

enough to overcome the work to fracture the ferrite, or would blunt the crack if the ferrite could deform to allow the crack tip stresses to relax. Smith expressed the dependence of the fracture stress on the carbide thickness as:

$$\frac{C_0}{d} \sigma_f^2 + \tau_{eff}^2 \left( 1 + \frac{4}{\pi} \left( \frac{C_0}{d} \right)^{1/2} \frac{\tau_f}{\tau_{eff}} \right)^2 \left( \frac{\pi(1-\nu^2)d}{4\gamma_p E} \right) > 1 \quad <32>$$

- $C_0$  = carbide particle thickness
- $d$  = grain size
- $\sigma_f$  = cleavage fracture stress
- $\tau_{eff}$  = effective shear stress
- $\tau_f$  = friction stress
- $\gamma_p$  = effective surface energy
- $E$  = Young's modulus
- $\nu$  = Poisson's ratio.

Smith included a term for the grain size because of its role in the crack nucleation process through dislocation pile-ups. The number of dislocations increased with grain size for a constant effective shear stress and thus, the stress intensification at a particle which impedes dislocation motion increased with grain size, thus increasing the likelihood of crack nucleation at that particle. The model that Smith proposed also described the influence of temperature and strain rate on the cleavage fracture process by taking into account the effect of these parameters on the effective shear stress.

Smith's equation suggested a critical fracture stress criterion for cleavage [80]. That is, the stress at the

crack tip must exceed the critical fracture stress of the material before cleavage fracture would occur. This critical fracture stress corresponded to a critical density of slip dislocations which would serve to fracture carbides in steels, either by stress induced at the end of a pile-up, or by plastically straining the matrix and producing sufficient strain localization at the carbide/matrix interface to crack the particle by a fiber-loading mechanism. This crack nucleus would then propagate across the carbide due to the inability of the of the brittle carbide microstructure to arrest crack growth through deformation. The Smith model described the critical event in the cleavage fracture process as the presentation of a crack of size equal to the carbide thickness to the ferrite matrix [80]. Smith did not propose that cleavage fracture could not occur unless carbides were present in the matrix but instead pointed out that brittle carbides provided an avenue by which a crack could grow to a sufficient length to ensure self-propagation under the applied tensile stress, assisted by the local stress fields of the dislocations.

Ritchie, Knott and Rice [81], using the crack tip stress determination of Hutchinson [82], Rice and Rosengren [83] (called the HRR crack tip stress distribution) for a power law hardening material, noted that if a critical stress criterion for fracture were used, as described by the

Smith model, fracture could be produced very close to the crack tip by vanishingly small applied loads. Experimental results disagreed with this theory so Ritchie, Knott and Rice postulated that not only did the crack tip stresses have to exceed the critical fracture stress of the material but that this critical stress must be achieved over some microstructurally significant distance. Experimentation suggested that a characteristic distance of two grain diameters agreed quite closely with the experimental variation of  $K_{IC}$ . It was thus concluded that the critical event controlling the cleavage fracture in mild steels was the attainment of a critical stress over a distance of two grain diameters in front of the crack tip.

Curry and Knott [84] examined the microstructural significance of the characteristic distance by observing the variation of the fracture toughness and critical tensile stress with grain size in a mild steel at a constant low temperature. Their results indicated that when the grain diameter was over 40 microns, the characteristic distance increased with grain size but that at smaller grain sizes the characteristic distance remained constant. They used the Smith equation <32> to explain the significance of their findings. Eliminating the grain size dependence of the Smith equation by assuming that the diffusional processes controlling grain growth were the same as those controlling carbide size, they evaluated the carbide thickness

responsible for crack initiation. They used statistical sampling to describe the initiation process as a competition between thinner carbides in a smaller region of higher stress and the less numerous, thicker carbides in a larger region of lower stress. They concluded that if the ratio of carbide thickness to grain size remained constant then as the grain size is reduced, more grains have to be sampled to provide a particle of sufficient thickness and correct orientation to nucleate a crack. Thus, they suggested that as the grain size is decreased to very small diameters at a constant characteristic distance, the critical fracture event may change from propagation of a crack from the carbide into the ferrite matrix to propagation of the crack from one ferrite grain to another.

In further work, Curry and Knott [85] found that fracture occurs when the largest favorably oriented cracked particle is subjected to sufficient local tensile stress to satisfy the crack propagation energy balance. They found a dependence of the fracture stress on the 95<sup>th</sup> percentile of carbide radii. Using the thickness of the top 5% of the carbides measured in their steels in the Smith equation, they calculated a value for the effective surface energy, ( $\gamma_p$ ) of 9 to 14 J/m<sup>2</sup> which is 5 times the free surface energy for ferrite. Knott [86] proposed that this difference between the effective surface energy required for



crack growth and the actual measured free surface energy in bcc iron was due to the dislocation motion required for achievement of the critical crack mouth opening needed to fracture successive atomic bonds ahead of the crack tip. Using this mechanism, Knott estimated the increase in effective surface energy during fracture to be five times the free surface energy, a value which agreed closely with measured values. The success of the statistical model proposed by Curry and Knott [85] suggests that the characteristic distance has to be considered as an expectance value which depends on the carbide population.

Ritchie et al., [81] demonstrated that, although there was no simple relationship between the microstructure of a steel and the characteristic distance, it was possible to describe the microstructural sampling process using a single parameter,  $\sigma_{11}(X)$ . They proposed a microscopic cleavage fracture criterion which they expressed as:

$$\sigma_{11}(X) > \sigma_f \quad <33>$$

where  $X$  is the distance ahead of the crack tip but within the plastic zone. Combining this expression with the crack tip stress distribution of Hutchinson [82], Rice and Rosengren [83], gives a general expression for the cleavage fracture toughness,  $K_{Ic}$ :

$$K_{IC} = \beta^{-(N+1)/2} X_0^{1/2} \frac{\sigma_f^{(N+1)/2}}{\sigma_y^{(N+1)/2}} \quad <34>$$

where  $\beta$  is the amplitude of the stress singularity,  $N = 1/n$ , the inverse of the work hardening exponent, and  $X_0$  is the characteristic distance. This analysis only holds for  $X_0$  smaller than the plastic zone.

The above models all present the microstructural dependence of the cleavage fracture stress without describing dependence on the temperature and strain rate. Smith [80] ascribed a small amount of the temperature and strain rate dependence of  $\sigma_f$  in his equation, <32>, to the sensitivity of dislocation motion to these variables. This sensitivity shows up in the friction stress term,  $\tau_i$ , with  $\tau_i$  increasing with decreasing temperature and increasing strain rate causing a reduction in  $\sigma_f$ . This variation of  $\tau_i$  with temperature and strain rate did not totally describe the temperature dependence exhibited by  $\sigma_f$  at temperatures below  $-100^\circ \text{C}$ , so Smith concluded that the increase in  $\sigma_f$  was due to an increase in the effective surface energy of the ferrite matrix.

Armstrong [87] proposed that the yield stress of a mild steel varied with temperature as:

$$\sigma_y = \sigma_1 + \sigma_2 \exp\{-(B_1 - B_2 \log \dot{\epsilon})/T\} \quad <35>$$

$\sigma_1$  is the athermal term (a constant) which combines solid solution hardening effects with structural hardening effects,  $\dot{\epsilon}$  is the strain rate,  $T$  is temperature, and  $B_1$  and  $B_2$  are constants. Using this equation for the yield stress, Armstrong wrote an equation for the fracture toughness as:

$$K_{IC} = \frac{\beta^{-(N+1)/2} x_0^{1/2} \sigma_f^{(N+1)/2}}{(\sigma_1 + \sigma_2 \exp(-BT))^{(N-1)/2}} \quad <36>$$

Writing this equation to include the effect of grain size (using  $\sigma_1 = \sigma_3 + k_y d^{-1/2}$ ) gives:

$$K_{IC} = \frac{\beta^{-(N+1)/2} x_0^{1/2} (k_y d^{-1/2})^{(N+1)/2}}{(\sigma_3 + k_y d^{-1/2} + \sigma_2 \exp(-BT))^{(N-1)/2}} \quad <37>$$

This equation predicts that the fracture toughness will increase with increasing temperature and decreasing strain rate and grain size.

Ritchie et al. [81] explained the temperature variation of  $K_{IC}$  in mild steel by assuming that the critical distance varied with temperature. Taking an experimental value for the fracture stress, which was found not to vary with temperature over the range investigated, predictions of  $K_{IC}$  were made using various fixed values of the critical distance. They reasoned that, since the cleavage fracture process was propagation controlled, it depended on the level

of local tensile stresses. Using a precracked specimen, they determined that the absolute magnitude of the local tensile stresses at the crack tip did not increase with increasing plastic zone size but, instead, the stress distribution extended over a larger distance. At low temperatures, a crack nucleus can propagate when the plastic zone size is small because the yield stress is high and little crack tip stress elevation by constraint is necessary to satisfy the local propagation condition. At higher temperatures, the yield stress is smaller and deformation occurs more readily, so more constraint is required at the crack tip to achieve the critical fracture stress.

Curry [88] found that the temperature dependence of the cleavage fracture toughness could be accurately predicted by assuming a fixed value of the characteristic distance as two grain diameters. Since the yield stress increases with decreasing test temperature, a greater stress intensity factor has to be applied to obtain the critical combination of stress and distance ahead of the crack tip to satisfy crack propagation conditions. He thus concluded that the temperature dependence of the cleavage fracture toughness was due to the variation of the yield stress with temperature observed in ferritic steels.

Wallin et al. [89] found that the temperature dependence of  $K_{IC}$  predicted using the constant value of  $14 \text{ J/m}^2$  for the

work term, that was proposed by Curry and Knott [85], was unsatisfactory. They suggested that, since dislocation mobility depended on temperature, the plastic work term must also depend on test temperature. They found that a correct fit was found if a Peierls-Nabarro force/temperature dependence was used for  $\gamma_p$ , which relates  $\gamma_p$  and  $K_{IC}$  to the temperature dependence of the yield stress. Their model described the carbide induced cleavage fracture process in steels as a statistical competition between cracked carbides of various sizes at various orientations ahead of the crack tip, with cleavage fracture occurring when the critical combination of tensile stress and carbide size was achieved. The critical carbide size depended on the maximum tensile stress obtainable at the crack tip and thus by the yield strength of the ferrite matrix, with higher yield stress and strain hardening capacity creating stronger stress intensification at the crack tip and a lower critical carbide size.

Lin et al. [90] used a weakest link statistical model to give microstructural significance to the characteristic distance and to predict  $K_{IC}$  as a function of temperature and microstructure. Using the HRR crack tip stress solution for the stress distribution near the crack and a linear elastic solution for stresses near the elastic/plastic interface they found that the failure probability given by

weakest link statistics is:

$$p = 1 - \exp\left(- \int_0^V [dV \int_0^{\sigma} g(S) dS]\right) \quad <38>$$

V is plastic zone volume,  $\sigma$  is the applied stress, and S is the carbide strength. This model assumed that the critical event in the cleavage fracture process was the propagation of a microcrack from a carbide into the ferrite matrix. It did not hold if the rate limiting step was propagation of a crack from one ferrite grain into another.

Rosenfield et al. [91] used detailed fractography to study cleavage initiation sites in an effort to better understand the statistical variations of  $K_{IC}$ . For specimens which showed no stable crack growth, their results agreed with the RKR model in which a critical tensile stress is required over a characteristic distance to initiate a cleavage crack. However, a significant finding of their study is that a large portion of the cleavage nucleating particles were manganese-sulfide particles of approximately 1 micron in diameter, which crack at considerably lower strains than do carbides. These results indicated that a secondary microstructural feature is more important than carbide or grain size in determining where cleavage fracture occurs. They suggested that this secondary structure may be a collection of synergistically orientated ferrite grains, possibly within the same prior-austenite grain. The

conclusion that the carbides may not be the primary factor in determining cleavage initiation is supported by the work of Zhang, Armstrong and Irwin [92] who found that cleavage cracks did not initiate in the carbides due to strain in the surrounding ferrite matrix but, that the crack actually initiated at the carbide/ferrite boundary, propagated through the ferrite grain, and then caused fracture of the brittle carbide. They suggest that the critical distance for cleavage initiation ahead of the crack tip is more closely related to several large ferrite grain diameters, and that in materials with a nonhomogeneous distribution of grain sizes, regions of large grains are the weak spots. Although their work was done primarily on weld microstructures, these ideas suggest use of models other than those which describe the cleavage fracture process in terms of critical carbide size may be more applicable for any non-homogeneous microstructure.

## EXPERIMENTAL PROCEDURE

The objective of this research program was to determine the microstructural parameters controlling the strength and toughness properties; in particular, the cleavage fracture process of a microalloyed structural steel. Towards this objective, elastic-plastic fracture mechanics testing was combined with detailed microstructural and fractographic analysis to give a complete characterization of the fracture process in these steels.

### MATERIAL

Material, in the form of two 2.5 m by 3.7 m, 50 mm thick plates of ASTM, A710, Grade A steel, in the Class 3 heat treat condition, which had been re-solutionized, quenched and aged for 2 hours at 595° C, was obtained from two different producers of steel plate. The plate chemistries were determined using wet chemical analysis techniques.

### MICROSTRUCTURAL CHARACTERIZATION

A detailed analysis of the microstructures of the two plates was carried out using optical, scanning electron



(SEM) and transmission electron microscopy (TEM) techniques to characterize the grain geometry and size distribution, particle geometry and size distribution, grain boundary structures, and dislocation structures and densities. The microstructures of the two plates were then compared, and differences were noted and used in equations relating strength to microstructure to determine the effects of the microstructural differences.

#### Optical Microscopy and Metallography

Metallographic specimens were taken from the mid-thickness of each plate. Surfaces, in the three orthogonal directions (longitudinal, long and short transverse directions), were polished, etched and then examined in the optical microscope for microstructure characterization. Polishing was done by hand so that these same specimens could also be analyzed in the SEM.

Rough polishing was accomplished on the grinding wheel using decreasing grit sizes from 120 grit to 600 grit. Polishing at each grit size was carried out until the lines produced by the previous grit were removed. Fine polishing was accomplished using a nylon, napless cloth, with diamond paste which was wetted with lapping fluid. The steps in the fine polishing process were 6 micron, 3 micron, 1 micron and 1/4 micron, with a final polish carried out using an OP-S

slurry. The specimens were rinsed with methanol between each polishing step so that grit from the previous step would not contaminate the subsequent step. Following the final polish the specimens were rinsed in methanol and then hot air dried.

Two different etchants were used to bring out different features of the microstructure. A two percent nital solution was used to bring out the general microstructural features, while a five percent picral solution was used to enhance the carbides. Specimens were immersed in the etchant for about 1 and 1/2 minutes, then taken out and rinsed in distilled water to stop the reaction. Several specimens required heating under the hot air blower for a minute to start the etching reaction.

Photomicrographs were taken at 50X, 250X, 500X and 1000X using a Zeiss Axiomat inverted optical microscope to determine if there was a rolling structure present in either plate and to characterize grain size and geometry. Actual grain diameters were measured to determine the distribution in grain sizes. Measurements were made until each additional measurement changed the percentage of the total at each diameter less than 1/2 percent.

## Scanning Electron Microscopy

The polished and etched metallographic specimens were put into a JEOL JSM 35CF scanning electron microscope (SEM) for higher resolution analysis and X-ray microanalytical identification of the grain structures and particles. Secondary and backscattered electron techniques were used to characterize microstructural features and to help in precipitate particle identification.

Wavelength dispersive x-ray microanalysis was carried out on polished specimens in a Camebax microprobe made by Cameca which allowed for quantitative surface compositional analysis. This system was used primarily for large particle identification since the resolution was limited to approximately 2 microns.

Energy dispersive x-ray microanalysis was conducted in the SEM using a KEVEX-7000 computer controlled x-ray analysis system. X-ray spectra, from areas of interest, were collected for 150 seconds and then the background noise removed and the peaks analyzed using KEVEX software. This technique does not give quantitative data but the semi-quantitative results were enough to identify particles in most cases.

## Transmission Electron Microscopy and Specimen Preparation Techniques

Transmission electron microscopy (TEM) was performed using a Philips 420 STEM with an EDAX-9900 x-ray microanalytical system attached. Particle identification, size, distribution and interaction with dislocations was characterized using bright field, dark field, and selected area diffraction techniques. Diffraction patterns were recorded from single ferrite grains, and precipitates with dark field images recorded using spots from the precipitate diffraction pattern. Grain boundary structures were also identified and characterized. Precipitate size distributions were determined from TEM photomicrographs using the grid method described in the ASM Desktop Handbook.

TEM specimens were prepared by cutting thin slices (1/2 to 3/4 mm.) from Charpy V-notch specimens from each plate using a diamond saw at medium speed with Buehlers cutting fluid for a lubricant. The slices were then chemically thinned by immersing them into a mixture of 5 ml sulfuric acid, 8 g oxalic acid, 100 ml distilled water and 100 ml of hydrogen peroxide until they were reduced to about 50 to 80 microns in thickness. Three millimeter discs were then punched from the thinned sheets. Electropolishing was done using a Struers Tenupol jet polisher until perforation occurred. The electropolish solution was a mixture of 33 volume percent nitric acid in methanol, with

electropolishing conducted at 15V at a temperature of -30°C.

#### MECHANICAL PROPERTY CHARACTERIZATION

Tensile, Charpy V-notch and quasi-static fracture toughness properties were measured for specimens from each of the two plates over a temperature range of 22° C to -160° C to characterize the fracture behavior of these plates as a function of temperature.

##### Tensile Testing

Tensile testing was done according to ASTM E8 procedures using a standard, round, 12.8 mm diameter specimen with a 50 mm gage section, Figure 6. Three specimens each were taken in the long transverse (T) and through thickness (S) plate directions, shown in Figure 7, to characterize the extent of anisotropy of the tensile properties. The remaining specimens were taken in the longitudinal direction (L) from each plate to minimize the effects of rolling on the tensile properties. Two specimens were tested at each temperature over the range from room temperature down to -160° C at 27° C intervals. 16 specimens in all were tested from each plate. All testing was conducted on a Tinius Olsen screw driven test apparatus with a 0.267 MN load cell and a variable strain rate controller which was set at  $1.7 \times 10^{-5}$  m/s. A well

insulated cold box, into which liquid nitrogen could be bled through copper coils, was used for testing specimens at just below room temperature, down to  $-160^{\circ}\text{C}$ . The specimen temperature was determined using a type T thermocouple attached to the specimen but insulated from the chamber with tape. The chamber temperature was determined using a type T thermocouple attached to the grips but with the end exposed to the chamber atmosphere. The chamber temperature was used as the reference for computer control of the  $\text{LN}_2$  valve. This system enabled temperature control to within  $\pm 1^{\circ}\text{C}$  at higher temperatures and to within  $\pm 2.8^{\circ}\text{C}$  at temperatures below  $-73^{\circ}\text{C}$ .

All data collection, as well as temperature control, was handled by a computer and software developed at the David Taylor Research Center, with the capability of reading multiple channels of data. The channels of data collected included: load, crosshead displacement, time, gage length extension via two extensometers and one strain gage, specimen temperature and chamber temperature. The temperature was controlled using the more sensitive chamber temperature thermocouple.

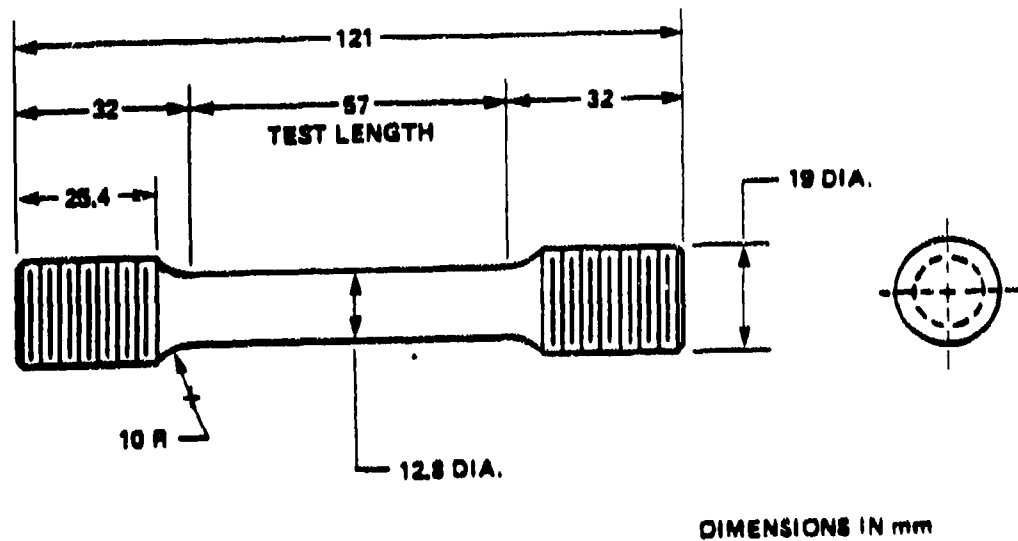


Figure 6. Schematic of the ASTM specified, 12.8 mm diameter tensile specimen used for determining tensile properties.

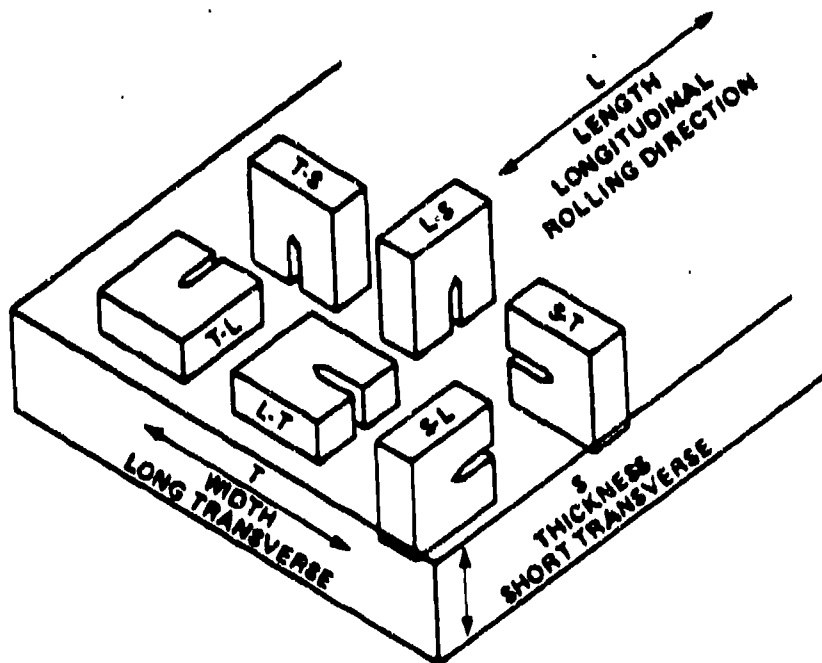


Figure 7. Schematic of plate material with plate and specimen directions labelled. After ASTM E399-81.

The extensometers were made using two 6.25 mm thick aluminum plates with holes at the center that were spring loaded at the inner diameter to allow attachment to the ends of the gage section. Transducers were inserted through holes in one plate and held with a set screw such that they were within 1/10 mm of the plate on the other side of the gage length. The transducers were connected through an amplifier to a voltmeter which was then attached to the computer. Calibration of the transducers was 0.635 mm/volt producing a total range of approximately 12.5 mm of extension.

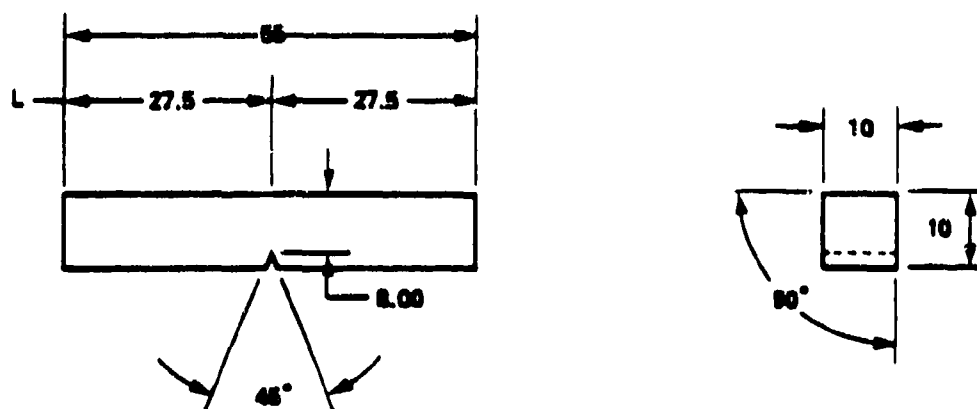
The strain gages were EP-08-250BG-120 gages from Micro Measurement Division which were attached to the specimens using AE-15 low temperature bond and rated at 10 percent to 15 percent extension. These gages were limited in the amount of strain that could be measured and thus were only used to verify the strain to yield.

The strain hardening exponent was determined using a regression analysis fit to the  $\log \sigma / \log \epsilon$  plot between the lower yield stress and the ultimate tensile stress. Young's modulus was determined using regression analysis on the elastic loading region of the load/elongation curves. The percent elongation and reduction in area were measured directly from the specimens and correlated to the displacement readings taken during the test.



## Charpy V-Notch Testing

Charpy V-notch testing was done according to the procedure specified in ASTM E23. The specimens were standard size, with all dimensions shown in Figure 8. All specimens from each plate were taken in the L-T orientation from the quarter thickness of each plate to minimize the effects from plate rolling on impact properties. Cooling was done using an alcohol bath and the temperature monitored using type T thermocouples attached to a dummy specimen in the bath. Specimens were mounted in the machine and loaded, via a hammer, and the total energy absorbed by the specimen during the test read directly from the dial indicator. Three specimens from each plate were tested at each temperature over a range from 38° C to -160° C at intervals of 17° C. This temperature range ensured a full ductile-to-brittle transition curve characterization for each plate.



DIMENSIONS IN mm

Figure 8. Schematic of the ASTM specified Charpy V-notch specimen used in all impact toughness testing.

## Elastic-Plastic Fracture Toughness Testing

J<sub>IC</sub> fracture toughness was determined for both plates using the ASTM E813 single specimen technique. The specimens were 25.4 mm thick, compact tension specimens which were notched and fatigue pre-cracked to a crack depth of approximately 0.65 a/W where a is the crack length and W is the specimen width. The fatigue precracking was carried out according to ASTM E813-81 on a hydraulic test apparatus at a frequency of 25 Hz with  $\Delta K$  kept below 30 MPa $\sqrt{m}$ . The specimens were side-grooved, with a 45° included angle to a depth of 10 percent of the specimen width, as shown in Figure 9, to keep the crack front relatively straight. The specimens were made in the L-T orientation of the plates to minimize the effects of plate rolling. Crack growth was measured via a clip gage mounted on razor edges attached at the load line of the specimen, Figure 9. Testing was done over a range of temperatures to characterize the ductile-to-brittle transition of the fracture toughness behavior.

The quasi-static J-R curve testing was conducted on a screw driven test machine with a 0.237 MN load cell. The cross head speed was  $1.7 \times 10^{-5}$  m/s. Testing was conducted using the computer-interactive unloading compliance test procedure of Joyce and Gudas [93]. Crack mouth opening displacement was measured using an MTS clip gage calibrated to a sensitivity of 0.38 mm of opening per volt for a total

range of 7.62 mm of crack opening. The compliance was used to calculate crack length and changes in crack length using the elastic compliance expression of Saxena and Hudak [94].  $J$  was calculated according to Ernst et. al. [95] which utilizes the incremental area under the load displacement record between lines of constant displacement. A curve of  $J$  versus  $\Delta a$  was then determined from the area under the load-displacement curve, a blunting line drawn, and  $J_{IC}$  calculated. For specimens which failed to exhibit stable crack growth, a value of  $J_C$ , the value of  $J$  at cleavage, was taken.

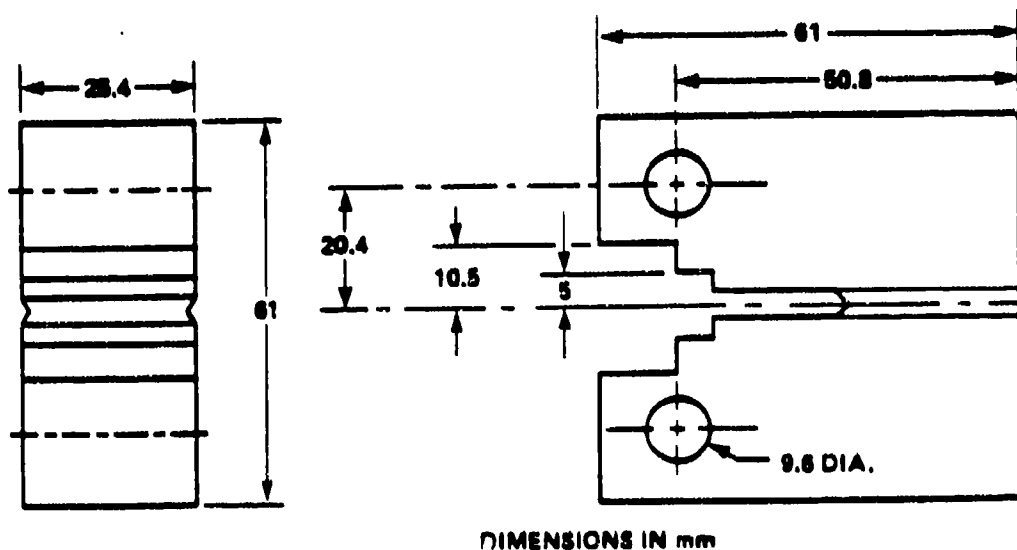


Figure 9. Schematic of the ASTM E813 specified compact tension specimen used in quasi-static fracture toughness testing.

Fracture toughness was measured over a range of temperatures to characterize the transition behavior of the two plates. Two specimens were tested at each temperature with the range of temperatures and intervals different for the two plates due to the difference in the ductile-brittle transition temperatures exhibited by the plates. Specimens from the plate exhibiting the lower DBTT were tested over a range from 22° C to -130° C at 14° C intervals while specimens from the plate exhibiting the higher DBTT were tested over the range 22° C to -73° C at 14° C intervals over much of the range and 5° C intervals through the transition region. The temperature was measured using type T thermocouples. The specimen thermocouple was peened into a small hole on the upper surface of the specimen, while the chamber thermocouple was attached to the upper grip. The more sensitive chamber temperature was used for computer control of the liquid nitrogen (LN<sub>2</sub>) valve which was used to bleed LN<sub>2</sub> into the chamber. This method of temperature control allowed control to within  $\pm 3^{\circ}$  C at temperatures below -73° C and to within  $\pm 1^{\circ}$  C at higher temperatures.

#### Fractography and Fracture Characterization

Once the specimens were fractured, by whatever method, the the specimens were cut approximately 12.5 mm away from the fracture surface and the fracture surface mounted into the scanning electron microscope for detailed stereo

fractography. Fracture mode was determined, and void or crack initiation sites were characterized. The cleavage initiation region was thoroughly examined to characterize the size,  $d$ , and geometry of the cleavage facet containing the cleavage initiating particle, and to identify the initiating particle or structural element. The distance from the sharp crack, for fracture toughness specimens, or blunt notch for impact specimen,  $X$ , to the cleavage initiation site was measured on each specimen exhibiting cleavage fracture to determine if there was an identifiable characteristic distance as described by Curry and Knott [85]. The distance between the growing ductile crack tip and the cleavage initiation site,  $r$ , was also measured. The cleavage initiation sites were identified using stereo fractography of the matching surfaces and following the "river pattern" characteristic of cleavage fracture in the stereo fractographs back to the origin of cleavage fracture as shown in Figure 10. In all cases, stereo fractography made identification of the cleavage initiation site easier, in some cases it was the only way identification of the initiation site could be made.

Energy dispersive x-ray analysis enabled identification of the particle initiating cleavage in most cases. Exceptions arose when the initiating particle was very small or no initiating particle was observed.

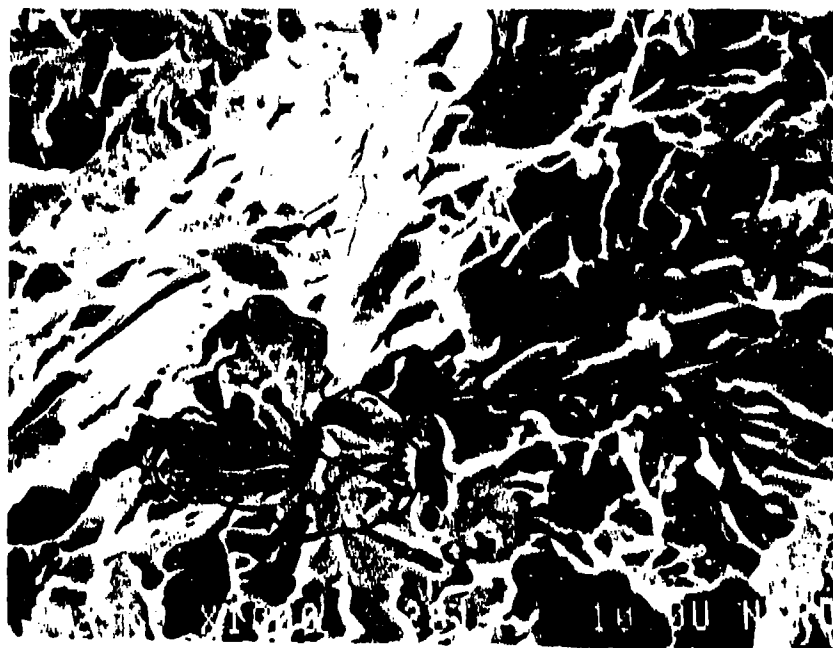
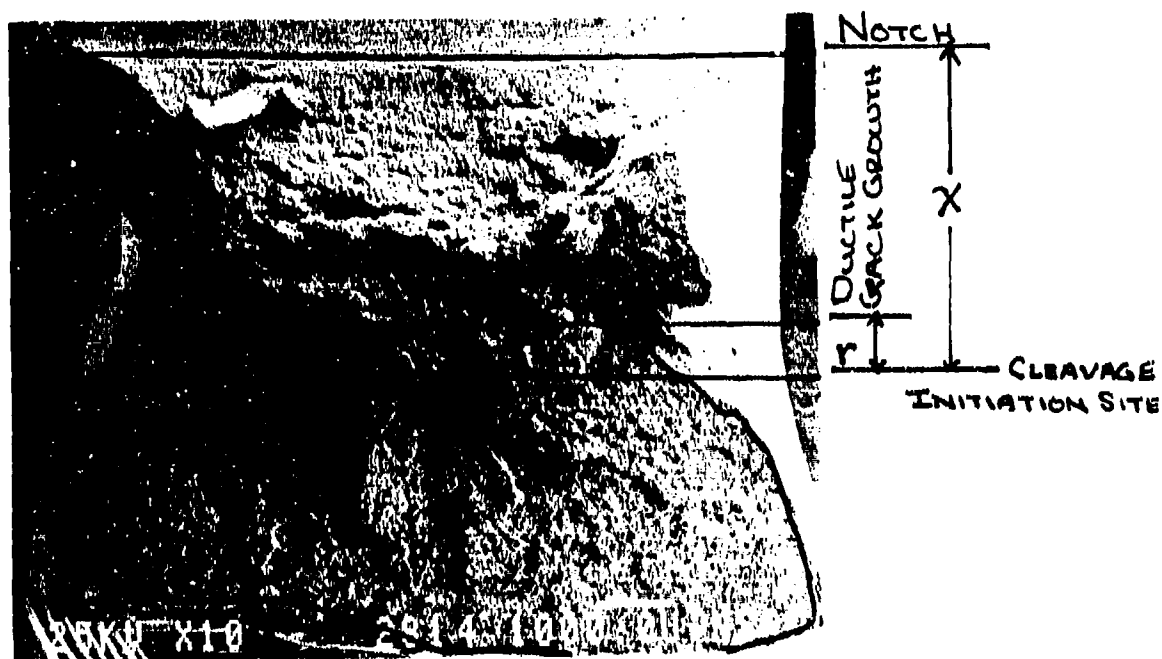


Figure 10. (a) SEM photomicrograph of the fracture surface of an impact toughness specimen with the distances that were measured labelled (10X). (b) SEM photomicrograph of the fracture surface of a compact specimen with the initiating cleavage facet outlined and the diameter marked (1000X).

Subsequent to fractographic examination, the fracture surfaces were electroplated with nickel for protection, cut with a slow speed diamond saw, polished and etched to reveal the microstructure, and examined in the SEM. The polish and etch techniques used were the same as those described earlier in the section on metallography. This technique allowed examination of the plastic zone associated with each fracture and measurement of secondary crack lengths. Secondary cracking was apparent on all specimens, and, following polishing and etching, the microstructural features associated with these secondary cracks could be observed, including the initiating microstructural feature. Secondary crack lengths were measured directly from SEM micrographs with enough being measured to ensure statistical significance.

## RESULTS

### MATERIAL

Chemistry and thermomechanical processing history play a large role in determining the complexity of the microstructure of high strength, microalloyed, age hardenable steels. The two plates studied in this program were produced to the same ASTM specification (ASTM A710, Grade A, Class 3 heat treat) but were produced by different producers using slightly differing techniques. The plate identified as GFF was ingot cast, rolled to a 203 mm slab, reheated to 1200° C, hot rolled to the final 50 mm thickness, and air cooled. The plate identified as GGN<sup>a</sup> was continuously cast into a 203 mm slab, reheated to 1200° C, rolled to the final 50 mm thickness, and air cooled. This difference in thermomechanical processing history resulted in a variation in grain size distribution that will be described later. The ASTM specification for this material allows small variations in chemistry, and, as shown in Table 1, the two plates exhibit slight differences in chemical composition. Plate GFF had a lower carbon content than plate GGN but had higher phosphorous, manganese, aluminum, and nitrogen contents.



# CHEMICAL COMPOSITION

Plate	C	Mn	P	S	Si	Ni	Cr	Mo	Cu
GFF	0.04	.586	.0052	.0043	.246	.900	.701	.188	1.17
GGN	0.058	.536	.0063	.0014	.269	.913	.759	.219	1.26
ASTM A710	.06	.40-	.025	.025	.40	.70-	.60-	.15-	1.0-
	max	.70	max	max	max	1.00	.90	.25	1.3

Element	Sn	V	Ti	Nb	Al	Ca	N
GFF	.006	.003	.002	.0333	.0412	.0023	.0146
GGN	.014	.005	.004	.0476	.0365	.0022	.0099
ASTM A710	-	-	-	.02 min	-	-	-

Table 1. Chemistries of the two ASTM A710, Grade A, Class 3, steels plates used in this research along with the ASTM specifications for A710.

## MICROSTRUCTURAL CHARACTERIZATION

Polished and etched microstructures were examined in the optical and scanning electron microscopes to characterize grain size distribution and geometry, as well as particle size distribution, geometry and spacing. Particle identification was characterized using wavelength and energy dispersive x-ray analysis, as well as transmission electron microscope (TEM) diffraction

techniques.

### Grain Structure

The grain structure for both plates consisted of polygonal ferrite interspersed with small regions of low carbon bainite (also called acicular ferrite). There were also very small regions of higher carbon which exhibited a structure composed of lath ferrite with interlath precipitation of carbide and cementite precipitates. Polished and etched surfaces, taken in the three major plate directions (longitudinal, long and short transverse), were studied in the optical microscope at low magnification to determine if any banding structures were apparent. No obvious banded structures were observed in either plate, figures 11 and 12, indicating that segregation of elements did not occur on a macroscopic level during the rolling process and that deformation during rolling was relatively homogeneous, and suggesting a finish rolling temperature that was probably above the ferrite transformation temperature.

Higher magnification observation of the microstructures revealed small areas of high carbon content between the polygonal ferrite grains. High magnification SEM photomicrographs showed these areas to be small lath ferrite grains with a higher density of carbide or cementite

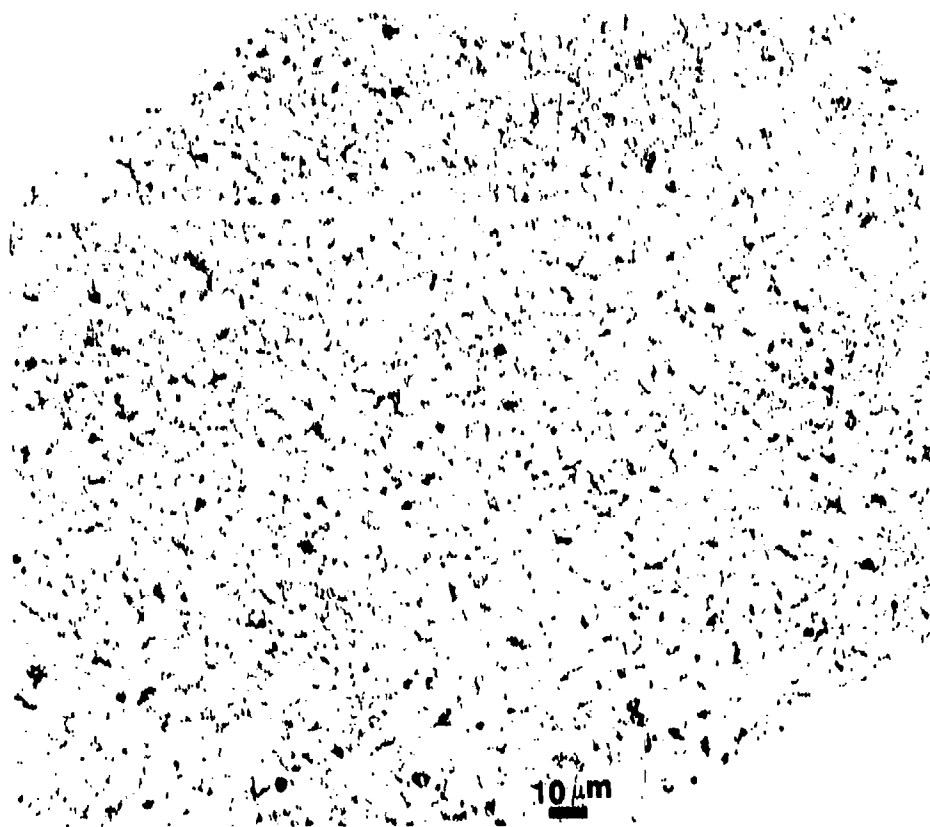


Figure 11. Optical photomicrographs, taken in the three orthogonal, plate directions of the microstructure of plate GFF (500X).

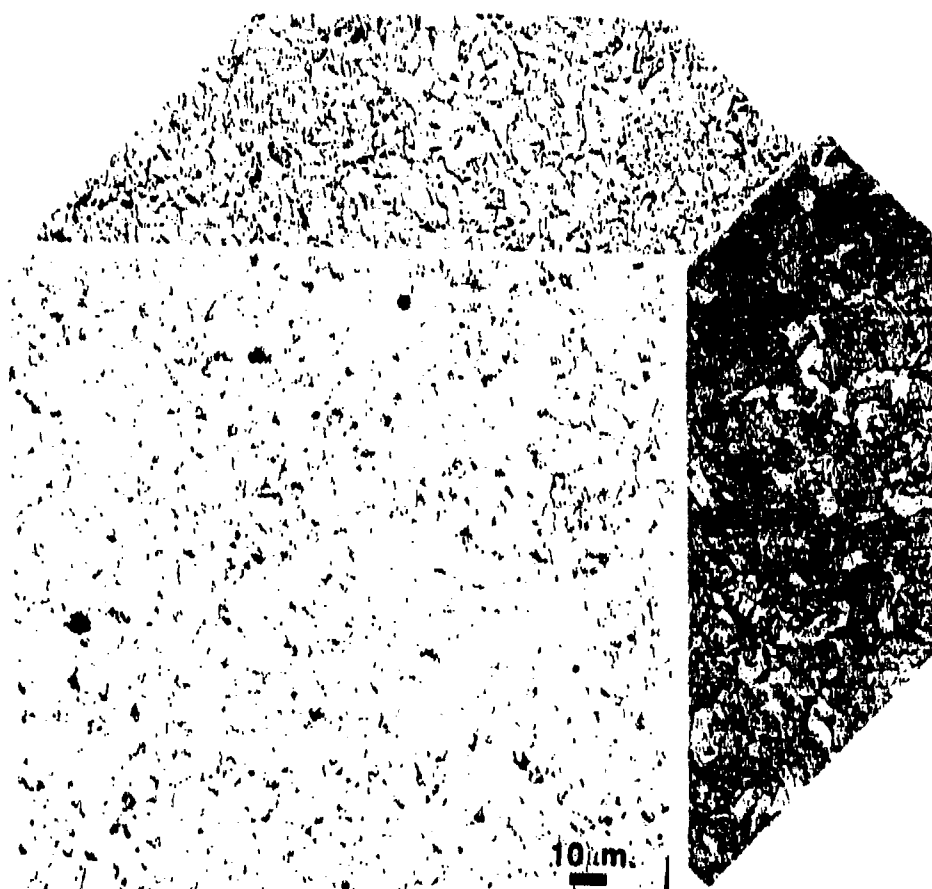
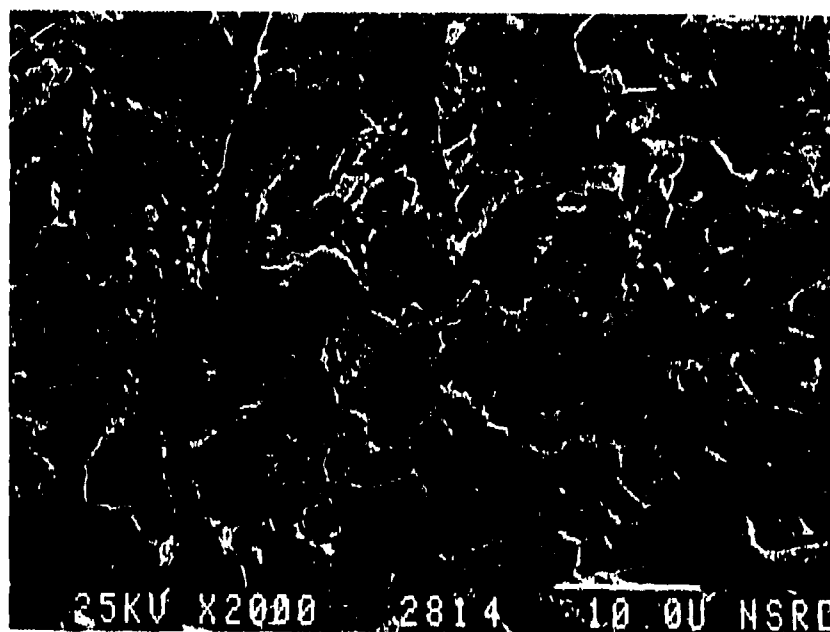


Figure 12. Optical photomicrograph, taken in the three orthogonal plate directions, of the microstructure of plate CGN (500X).



**a**



**b**

Figure 13. Scanning electron photomicrographs of polished GGN specimens etched in a 2% nital solution (a) 2000X (b) 10,000X.

precipitation than was observed in the low carbon acicular, and polygonal, ferrite grains figure 13. Grain boundary carbide films shown by arrows in Figure 13, were also apparent at many of the grain boundaries of both plates with the volume fraction of these carbides larger for plate GGN due to its higher carbon content. The presence of grain boundary carbide films was confirmed using transmission electron microscopy techniques.

Grain size distribution was determined for each plate from optical and SEM photomicrographs of polished and etched specimens, taken at 500X and 1000X, using a direct diameter measurement approach. The average grain size for each plate was determined by dividing the total diameter length measured by the total number of measurements taken. The average grain size for the two plates was similar with an average grain diameter of 7.8 microns for plate GFF and an average grain diameter of 8.7 microns for plate GGN. To get a better idea of the distribution of grain sizes, the largest diameter of each grain in several, random, photomicrographs were measured. These measurements were repeated until each additional measurement changed the distribution by less than one percent. The difference in grain size of the two plates was found in the distribution of grain sizes between the plates as shown in figure 14. Plate GFF exhibited a single peak distribution with the peak centered at 3 microns and skewed right with the largest

# GRAIN SIZE DISTRIBUTION

## Plates GGN and GFF

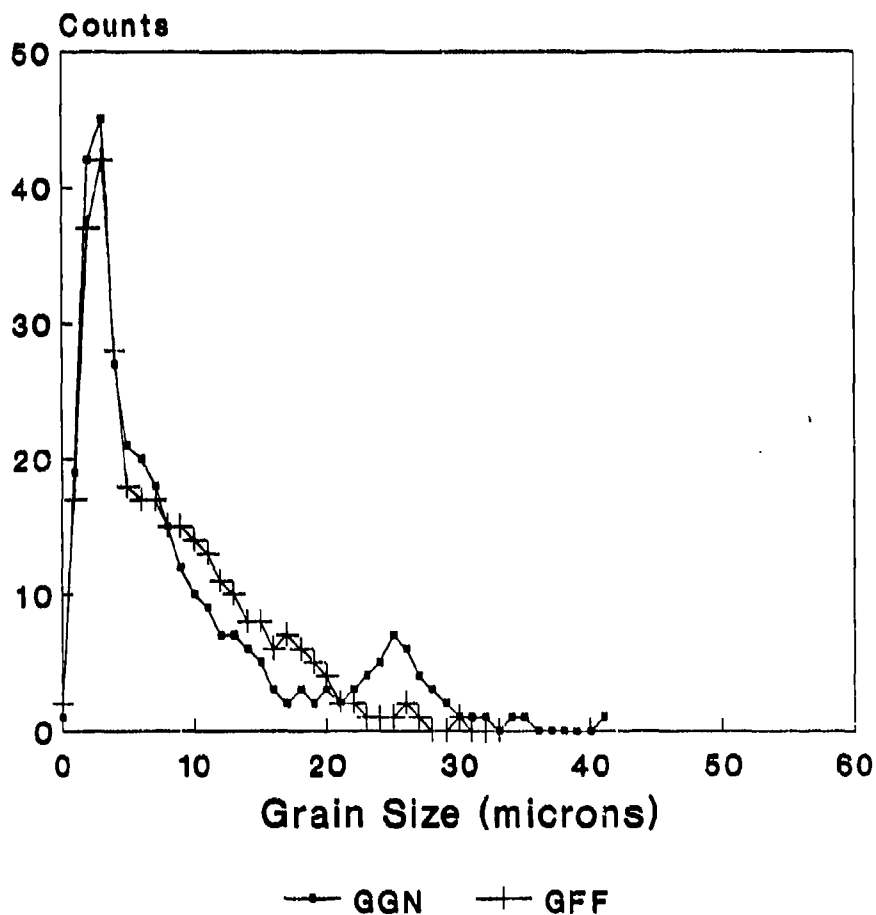


Figure 14. Plot of the grain size distributions for the two plates characterized in this study.

grain diameter measured at 30 microns. Plate GGN exhibited a bimodal distribution of grain diameters with the largest peak centered at 3 microns and a secondary peak centered at 25 microns and skewed right, with the largest grain diameter measured for this plate at 41 microns. Grain size plays a large role in both strength and toughness of a material but the effect of grain size distribution on toughness has not yet been determined. Using the Hall-Petch equation <4> it might be expected that plate GFF would have a slightly higher strength than plate GGN. That this is not true will be shown later and provides supporting evidence for microstructural features, other than grain size, contributing to strength.

#### Precipitate and Inclusion Characterization

Precipitates and inclusions were characterized using x-ray and transmission electron microanalytical techniques such as bright and dark field imaging and selected area diffraction. Elemental x-ray mapping techniques identified elongated niobium (assumed here to be carbonitrides), cuboid titanium nitrides, spherical as well as some elongated manganese sulfides, and oxides of aluminum and iron. Table 2 lists the precipitate size ranges, average size and interparticle spacing for each of the particle types identified. The sulfides were usually associated with



oxides in sulfide-oxide complexes (lower melting sulfides coating the high melting oxides). These complex particles tended to be large and ranged in size from 0.2 to 20 microns in diameter. Smaller equiaxed oxides and sulfides were also identified, Figure 15. Both plates contained a fine dispersion of copper precipitates ranging in size from 25 to approximately 200 angstroms in diameter, Figure 16. TEM electron diffraction patterns were used to identify the precipitate structures as FCC as shown in Figure 17, indicating that the copper precipitates were present in a slightly overaged condition [45,46]. The distribution of copper precipitates was nonuniform with the fine precipitates tending to form clusters ranging in size from 5 to 25 nanometers, Figure 18.

TABLE 2

## PARTICLE SIZE AND SPACING

particle	mean size		mean spacing		volume fraction	
	GFF nm (2r)	GGN nm (2r)	GFF nm (L)	GGN nm (L)	GFF (f)	GGN (f)
NbCN	16	18	67	62	0.19	0.27
TiN	28	31	610	525	0.005*	0.007*
MnS	31	25	350	365		
FCC Copper	12	11	77	65	0.040	0.067
	+/-5nm		+/-20nm			

\* Total volume fraction of large particles.

Table 2. Particle sizes and interparticle spacings for all the particles identified using TEM microscopy techniques.

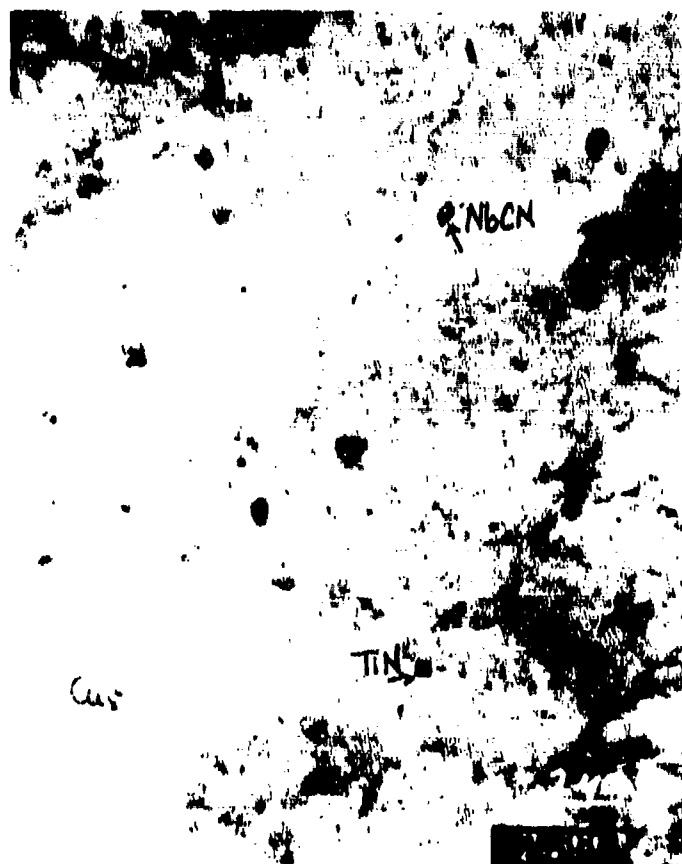


Figure 15. Transmission electron photomicrograph showing the particle distribution in plate GGN.

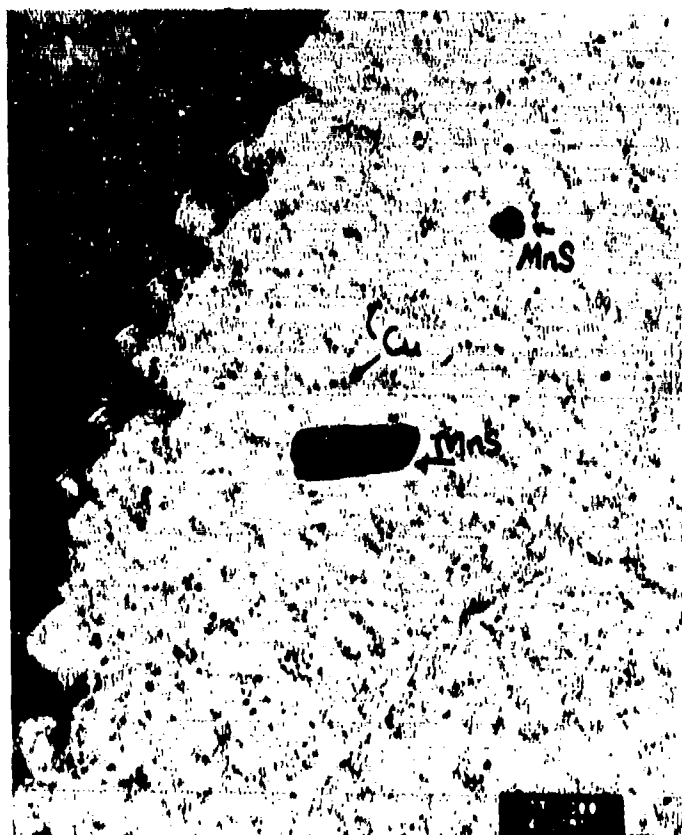


Figure 16. Transmission electron photomicrograph showing copper precipitates in the microstructure of plate GGN.

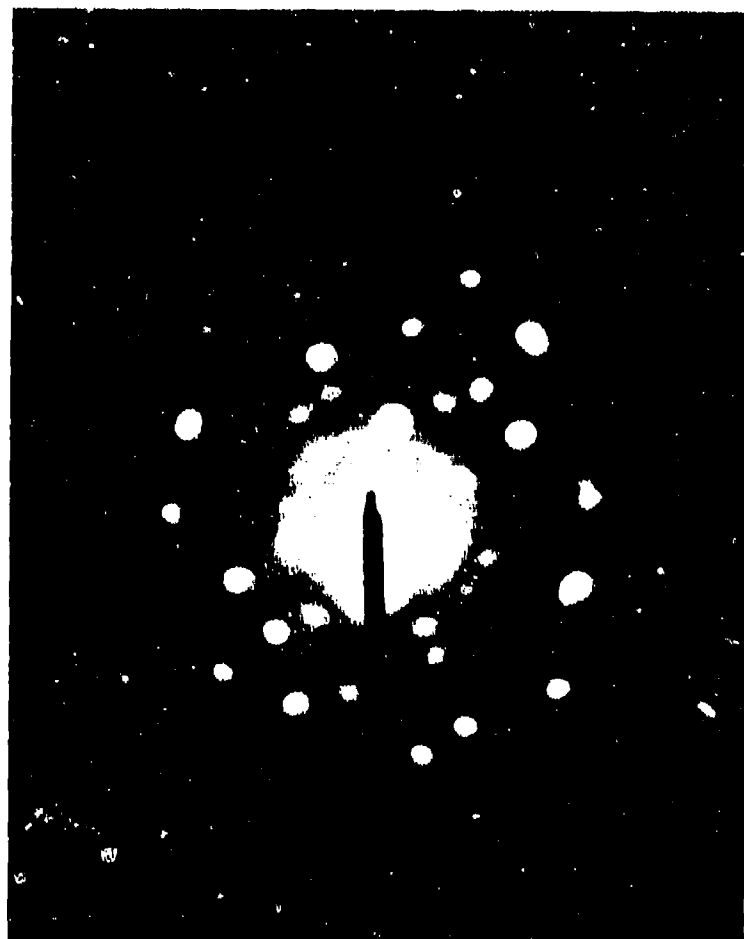


Figure 17. Transmission electron diffraction pattern taken from a region of fcc copper precipitates.

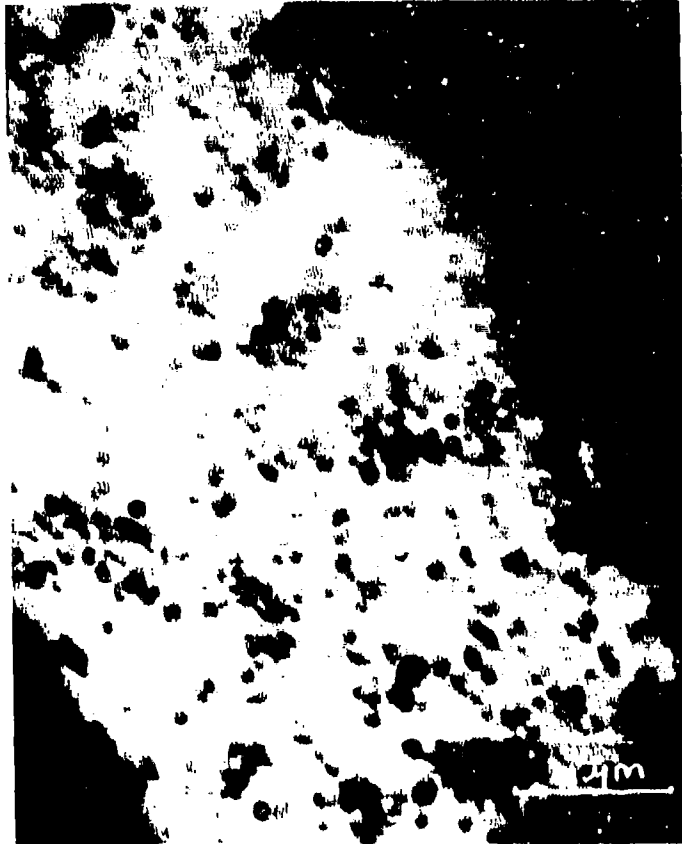


Figure 18. Transmission electron photomicrograph showing clusters of copper precipitates in the microstructure of plate GFF.

## MECHANICAL PROPERTIES

### Tensile Properties

Figure 19 shows typical load-displacement curves for one specimen from each of the two plates with the strain to fracture for the two plates noticeably different. Figure 20 shows the tensile properties of the two plates as they vary with test temperature. The 0.2% offset yield, ultimate tensile, and true fracture stresses were higher for the specimens from plate GGN over the range of temperatures tested than they were for the specimens from plate GFF. The tensile property/temperature relationship of both plates exhibited a change in slope at approximately  $-100^{\circ}\text{C}$ . However, as shown in Figure 20, this change in slope was steeper for tensile properties of plate GGN than for plate GFF.

The strain hardening exponent was determined for each specimen using the strain gage data and determining a regression analysis fit of the log true stress/log true strain curve between the lower yield stress and the ultimate tensile stress. Figure 21 shows the variation with temperature of the strain hardening exponent for both plate materials. The strain hardening exponent was higher at all temperatures for specimens from plate GFF which exhibited a strain hardening exponent of 0.18 at room temperature, while the strain hardening exponent for GGN at room temperature was 0.13.

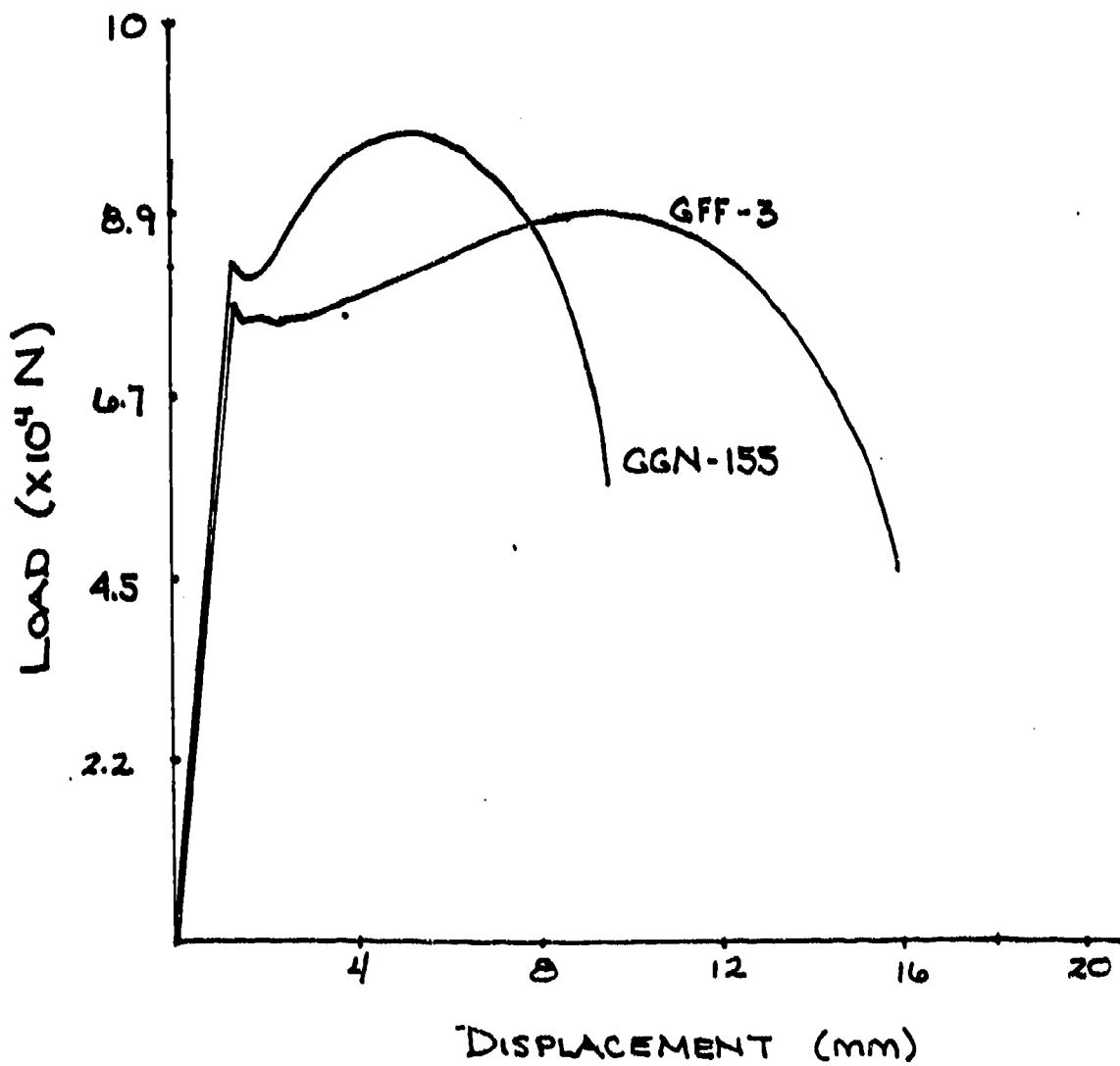


Figure 19. The load/displacement curves for one tensile specimen from each plate, tested at -40° C.



# TENSILE PROPERTIES VS TEST TEMPERATURE Plates GFF and GGN

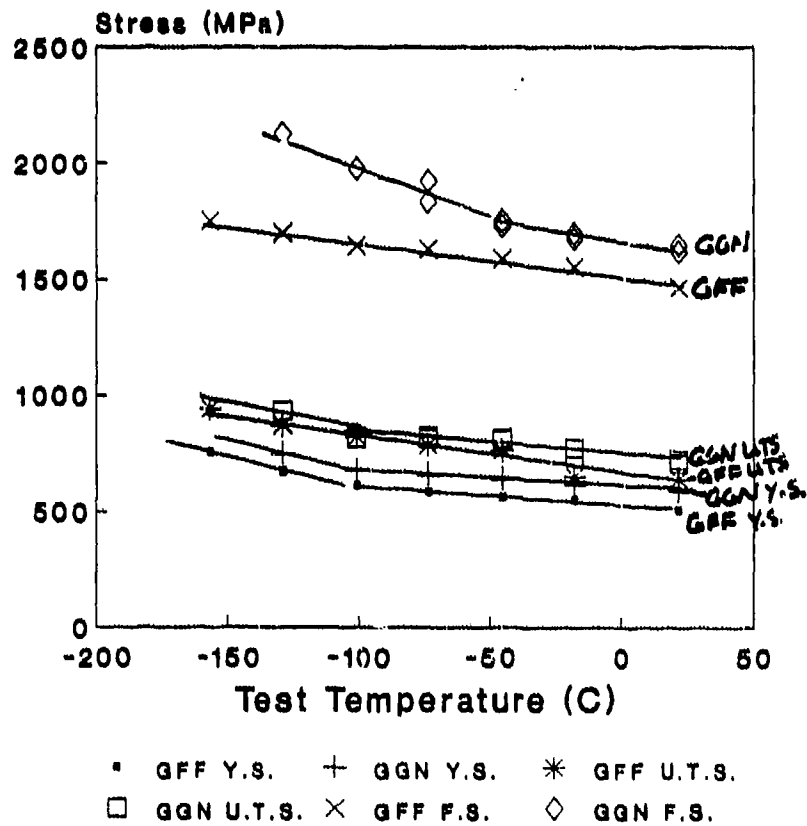


Figure 20. A plot of the tensile properties for plate GGN and GFF versus test temperature. (Bridgeman corrected [96])

# Strain Hardening Exponent Plates GFF and GGN

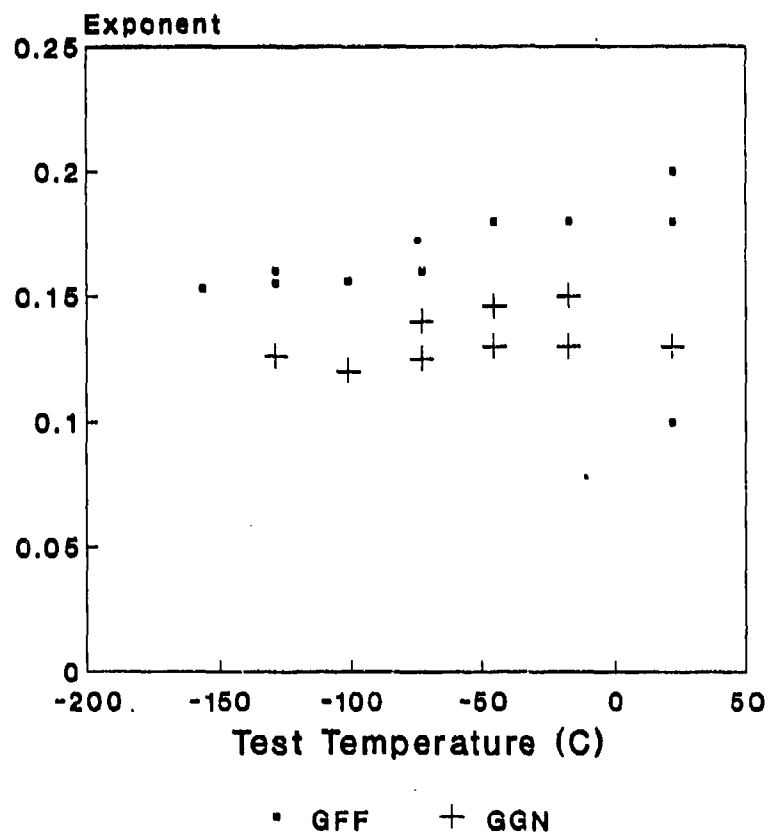


Figure 21. A plot of the strain hardening exponent for tensile specimens from plates GGN and GFF versus test temperature.

The strain hardening exponent for both specimens decreased slightly with decreasing temperature, with GFF exhibiting a larger temperature dependence.

Strain to fracture is shown in Figure 22, which contains percent elongation and percent reduction in cross section area (RA) vs test temperature curves for specimens from both materials. Specimens from plate GGN exhibited a slightly lower percent elongation and reduction in area over the range of temperatures tested than did GFF specimens, with the difference between the two plates increasing with decreasing temperature. This is consistent with strain hardening data. The percent elongation and reduction in area properties for both plates decreased with decreasing temperature but this decrease was modest for plate GFF specimens while both properties decreased rapidly for plate GGN specimens below test temperatures of  $-73^{\circ}\text{C}$ .

Above  $-73^{\circ}\text{C}$  the tensile properties of both plates varied with temperature in roughly the same way. At the lower test temperatures, plate GGN tensile properties showed a stronger dependence on test temperature.

Room temperature transverse (T) and through thickness (S) tensile tests were done on both plates in an earlier study [97] with results showing the transverse properties to be similar to those measured in the longitudinal direction (L). The properties measured in the through thickness plate

## Tensile Ductility Properties vs Test T Plates GFF and GGn

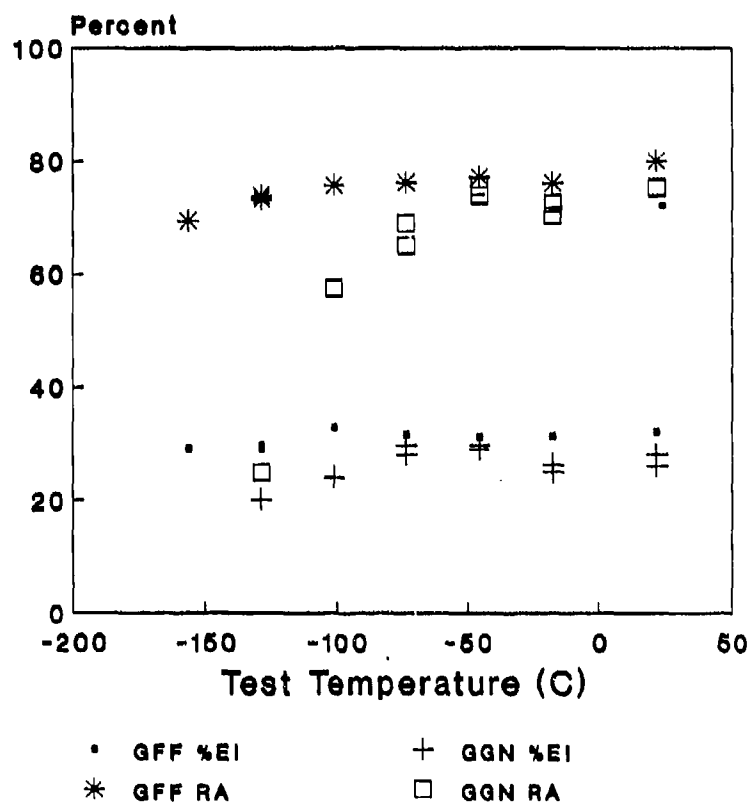


Figure 22. A plot of the tensile ductility properties (% elongation and reduction in area at fracture) for specimens from both plates versus test temperature.

direction (S) differed from those of the other two directions in that the yield strength and ultimate tensile strength were higher and percent elongation to fracture tended to be lower as shown in Table 3.

TABLE 3

Longitudinal L			Transverse T			Through Thickness S		
0.2% YS MPa	UTS MPa	%RA	0.2% YS MPa	UTS MPa	%RA	0.2% YS MPa	UTS MPa	%RA
Plate GFF 506	641	77%	511	603	80%	539	672	63%
Plate GGN 606	706	75.2%	600	711	74.3%	621	739	49%

Table 3. Tensile properties in the three orthogonal plate directions, measured at room temperature (22°C).

## Charpy Impact Properties

Figure 23 shows the impact energies versus test temperature for specimens from both plates. Specimens from the high strength plate, GGN, showed a lower upper shelf energy, a wider transition range and a higher transition temperature than did specimens from the lower strength plate, GFF. However, due to the maximum load limit of the test apparatus, the maximum upper shelf energy for plate GFF could not be completely characterized. GFF specimens tested at room temperature stopped the hammer without completely fracturing. The impact energy transition region was somewhat narrower and the lower shelf energies much lower for plate GGN specimens than for plate GFF specimens. Plate GFF showed completely upper shelf, ductile behavior at temperatures as low as  $-85^{\circ}\text{C}$  while plate GGN specimens exhibited only lower shelf, brittle behavior at these low temperatures.

## Fracture Toughness Properties

Quasi-static fracture toughness specimens were precracked to an  $a/W$  ratio of 0.65 as shown in Figure 9 of the previous section. Testing was conducted over a range of test temperatures to characterize the effect of temperature on the fracture toughness and fracture mode. Figure 24 shows the relationship between  $J_{IC}$ ,  $J_C$  and test temperature.

## CVN ENERGY vs TEST TEMPERATURE Plates GGN and GFF

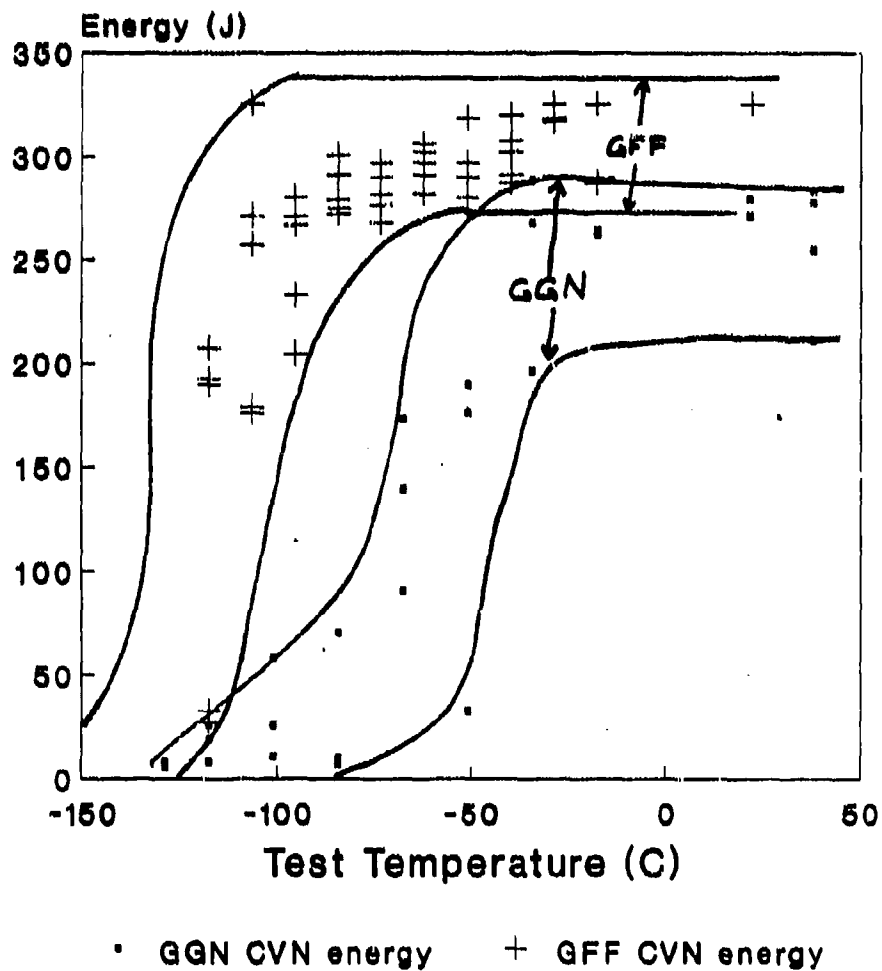


Figure 23. A plot of the Charpy V-notch impact energies for specimens from both plates GFF and GGN versus test temperature.

## J<sub>Ic</sub> AND J<sub>c</sub> VERSUS TEST TEMPERATURE Plate GFF and GGN Specimens

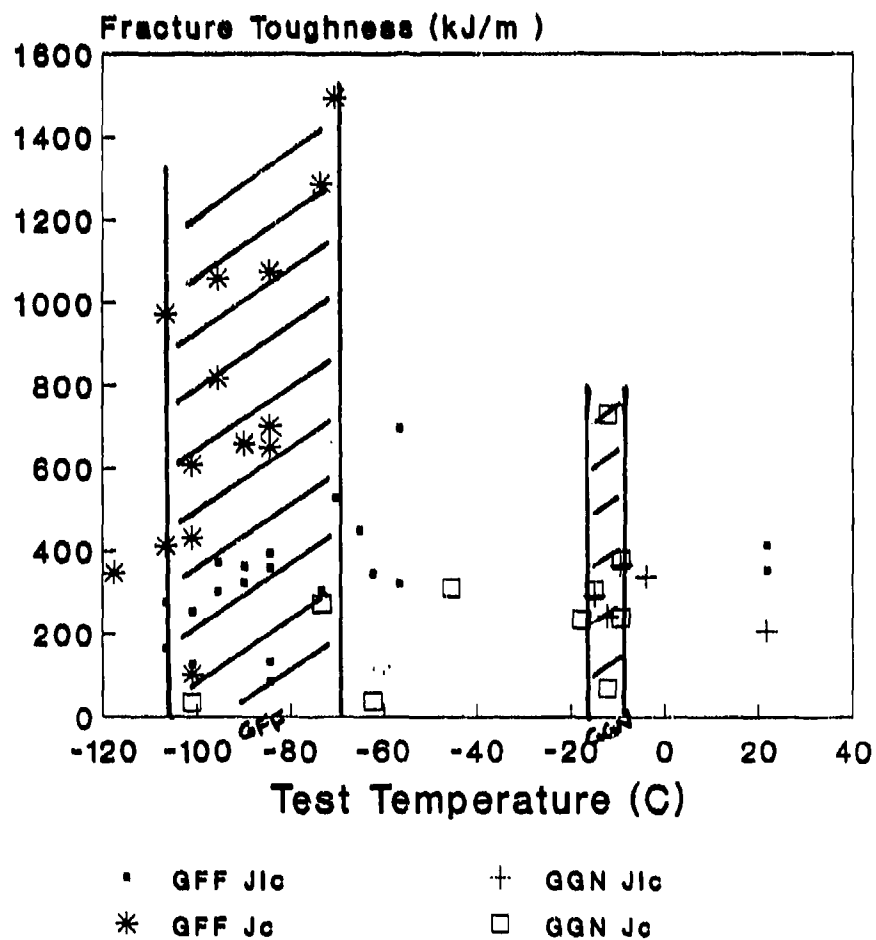


Figure 24. A plot of J<sub>Ic</sub> and J<sub>c</sub> fracture toughness versus test temperature for specimens from both plates GFF and GGN.



In this curve,  $J_{IC}$  is the work required to initiate stable crack growth, while  $J_C$  is used to denote the work to initiate unstable, cleavage fracture. The temperature range over which both fracture modes occurred (specimens with both a  $J_{IC}$  and  $J_C$  value) was considered to be the fracture mode transition region and is shown for both plate materials on this curve as a hash-marked region. As can be seen in Figure 24, the transition temperature region for the specimens from the lower strength plate, GFF, was much wider and occurred at a much lower temperature than for plate GGN specimens. Below a temperature of  $-112^{\circ}\text{C}$  all of the GFF specimens tested exhibited only cleavage failure, while above  $-60^{\circ}\text{C}$  the fracture mode was only ductile. In the fracture mode transition region,  $J_{IC}$  values of plate GFF specimens decreased with decreasing temperature. Above the transition region ( $-60^{\circ}\text{C}$ ), GFF  $J_{IC}$  values decreased slightly with increasing temperature, from a maximum value of  $696\text{ kJ/m}^2$ , to an average value of  $378\text{ kJ/m}^2$ , which is consistent with results obtained by Hasson and Joyce [98] on HY-80 steel.

Table 4 shows a comparison of the impact and quasi-static toughness transition properties with the transition temperature defined as the temperature at which there was approximately 50% cleavage (FATT) for impact specimens and stable crack growth to approximately 200 microns followed by

cleavage failure for quasi-static fracture toughness specimens.

TABLE 4

Plate	CVN FATT °C	J FATT °C	Room Temperature Yield Strength MPa
GFF	-110	-85	503
GGN	-60	-10	510

Table 4. A comparison of fracture appearance transition temperatures and room temperature yield strength properties for the two plates used in this study.

#### FRACTOGRAPHY AND FRACTURE CHARACTERIZATION

##### Tensile Fracture Mode Characterization

The fracture behavior of the two plates tested was similar with both plates exhibiting a distinct fracture appearance transition as test temperature was varied. At temperatures above room temperature, (21° C) specimens from both plates exhibited cup-and-cone, ductile fracture modes. At lower temperatures the fracture appearance consisted of microvoid coalescence combined with cracks in a plane which was parallel to the loading direction. These were termed longitudinal cracks since they were observed in the

longitudinal plate direction, Figure 7.

Longitudinal cracking was observed to be a temperature dependent occurrence with specimens exhibiting a more common cup-and-cone type of fracture at higher (upper shelf) temperatures. As the temperature was decreased, longitudinal cracking appeared in the form of a starburst pattern with the final transverse fracture occurring in the necked region by microvoid coalescence. These longitudinal cracks, which appeared in the upper transition region, were ductile in nature with both mode one and two dimples [99], Figure 25, indicating that the opening stresses were both in the direction of loading as well as in the direction of tangential stresses. The dimples also indicate that growth of the longitudinal cracks occurred in a stable, manner. The starburst type of longitudinal crack did not extend past the necked region, and longitudinal crack growth occurred well after necking had begun, possibly just prior to final fracture. As test temperature was decreased through the transition region, the number of longitudinal cracks in the starburst pattern decreased and the crack depths increased, extending almost to the end of the plastically deformed, necked region of the specimen. The fracture mode of both the final transverse fracture and the longitudinal cracks changed from microvoid coalescence to cleavage at the lower test temperatures.

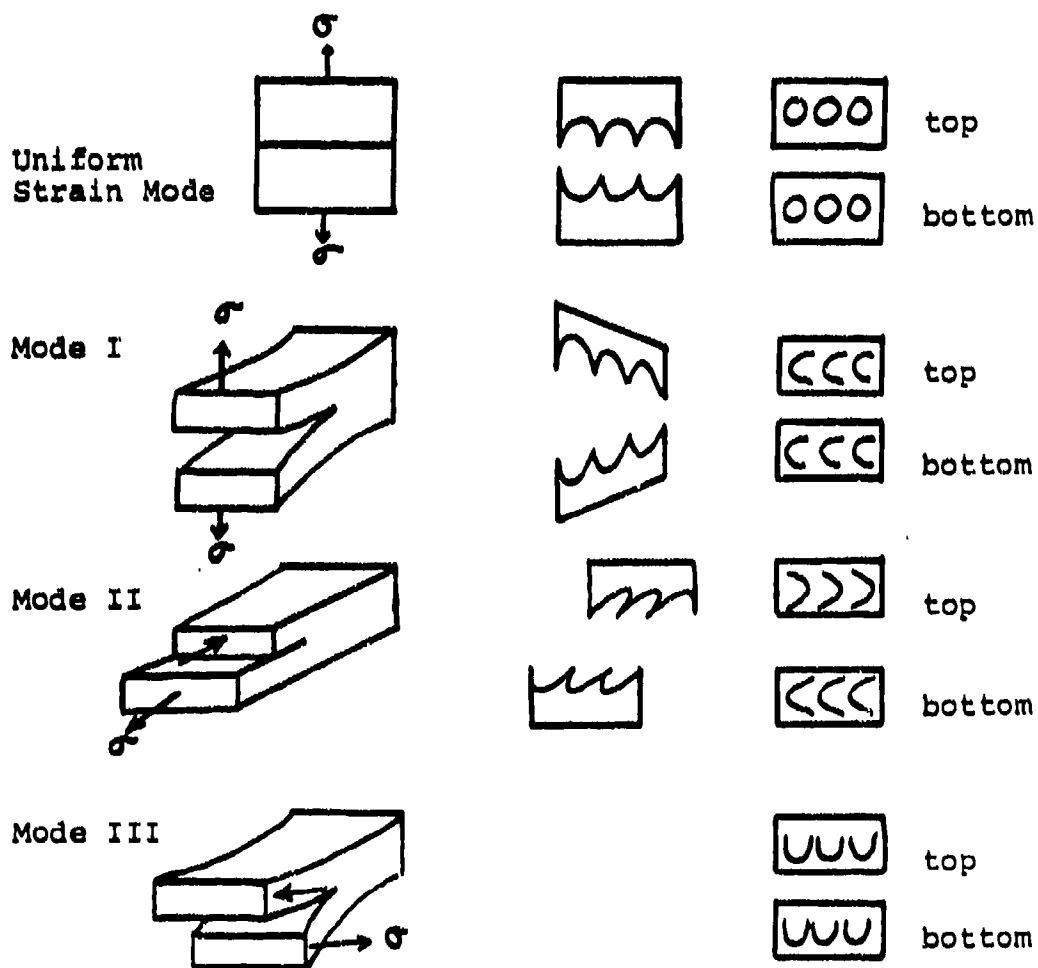


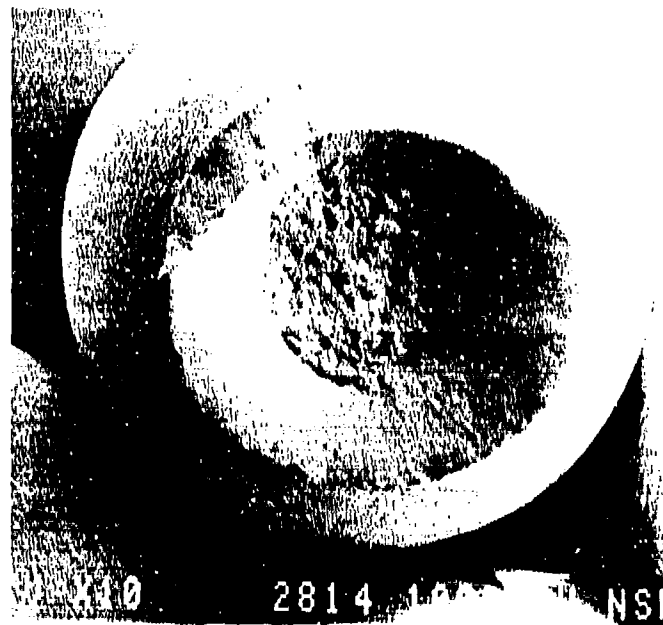
Figure 25. Line drawings showing the crack opening directions and the corresponding dimple shapes of the uniform strain mode and the three primary crack opening modes. After Beachem [99].

At the lowest transition temperatures one, or at most, three longitudinal cracks were observed which extended in a brittle manner throughout the necked region, at the center of the specimen diameter, and into the non-necked region of the specimen. The cleavage fracture surface appearance followed the deformation pattern of the grains indicating that fracture may have been intergranular along ferrite, or prior austenite grains, in the longitudinal crack, and that the longitudinal crack propagated after a critical amount of strain. The crack arrest region of the longitudinal cracks had a ductile appearance indicating that once the crack grew out of the necked region the material could strain harden enough to blunt the crack. Final fracture in these specimens occurred in a cleavage mode, outside of the necked region, at either, or both ends of the longitudinal crack. Fractographic analysis of the final fracture surfaces in the region of longitudinal crack arrest showed that the longitudinal cracks transitioned to a ductile fracture mode just prior to arresting and that the final, transverse cleavage fracture initiated at the point of longitudinal crack arrest. The lower limit of cold temperature testing in the apparatus used was  $-160^{\circ}\text{C}$  which was not low enough to evaluate the lower shelf behavior of the two plate materials. However, in tests done by other researchers [100,101], specimens tested at lower shelf temperatures did not exhibit longitudinal cracking.

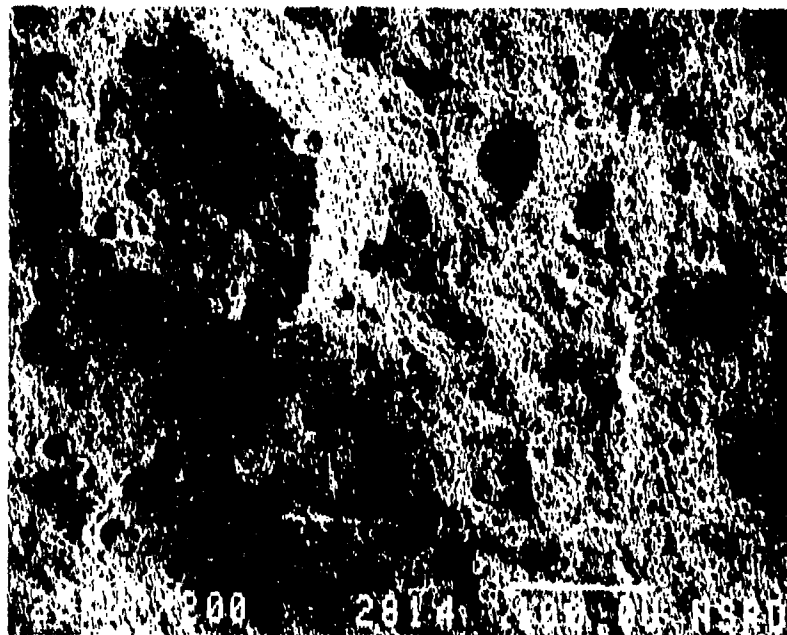
The fracture mode transition temperatures for specimens from plate GFF differed slightly from those of plate GGN. The ductile, cup-and-cone fracture mode occurred between 22° C and -20° C as shown in Figures 26. Dimple diameters varied in size from 0.1 micron to over 150 microns with dimple ligament direction indicating that crack growth occurred in a mixture of modes one and two, Figure 27.

The transition, starburst, fracture mode occurred between -20° C and -130° C as shown in Figures 28-30. The fracture mode in this region was characterized by mode one, opening dimples towards the center of the fracture surface and between longitudinal cracks. In the areas directly adjacent to the longitudinal cracks, mode two and three shear dimples were apparent, Figure 31. Areas of shear lip were found around the outer circumference of these specimens between the longitudinal cracks (which extended to the outside circumference in most cases), Figure 32. The longitudinal crack growth mode in this temperature region was also ductile void coalescence as shown in Figure 33.

Specimens containing a single, longitudinal crack and final, transverse, cleavage fracture outside the necked region were those tested at temperatures below -130° C shown in Figures 34 and 35. In all cases at the lowest test temperatures, the final transverse fracture occurred

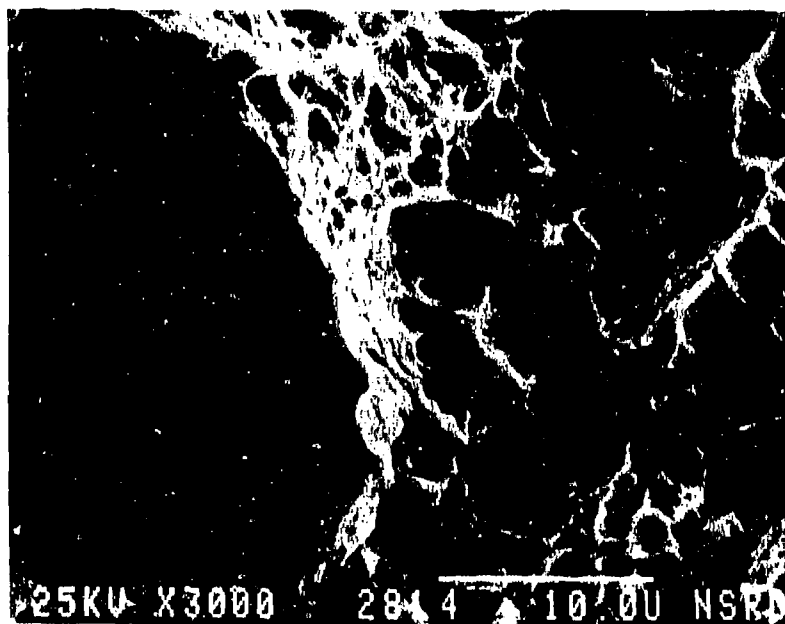


**a**

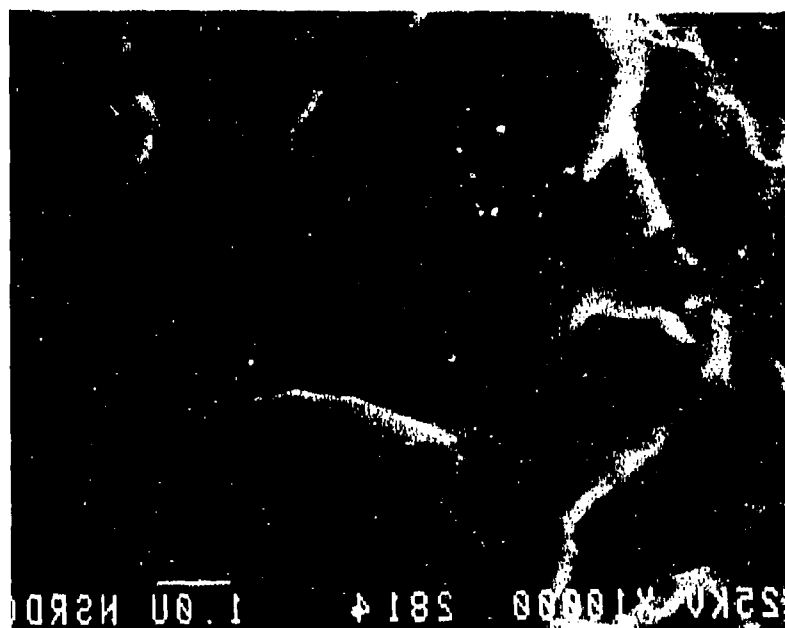


**b**

Figure 26. Scanning electron photomicrograph of the fracture surface of tensile specimen GFF-1 tested at 24°C. (a) Typical cup-and-cone appearance (10X). (b) Central fracture region with both large and small dimples (200X).



a



b

Figure 27. Scanning electron photomicrograph of the dimple morphology of tensile specimen GFF-1. (a) Large, deep dimple adjacent to region of small, equiaxed dimples (3000X). (b) Higher magnification shows the large size range of even the small dimples (10,000X).



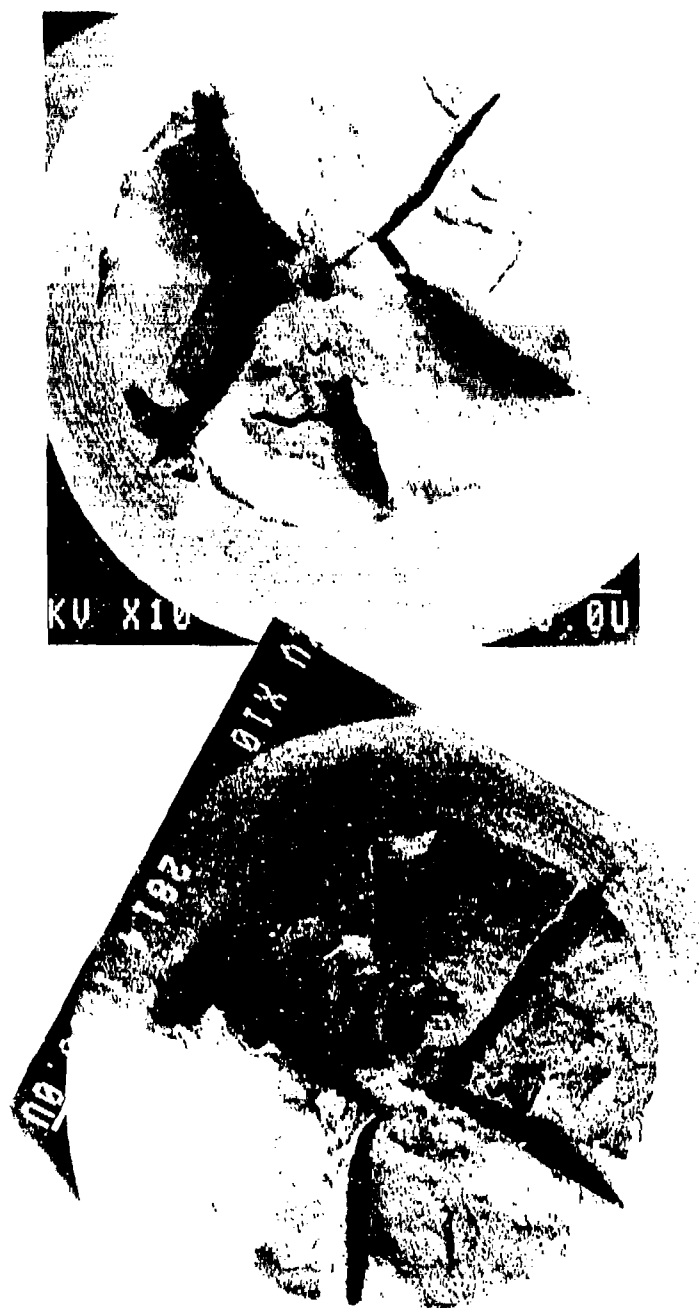


Figure 28. Scanning electron photomicrographs of the matching fracture surfaces of tensile specimen GFF-2 tested at  $-18^{\circ}\text{C}$  showing longitudinal cracks (10X).





**a**

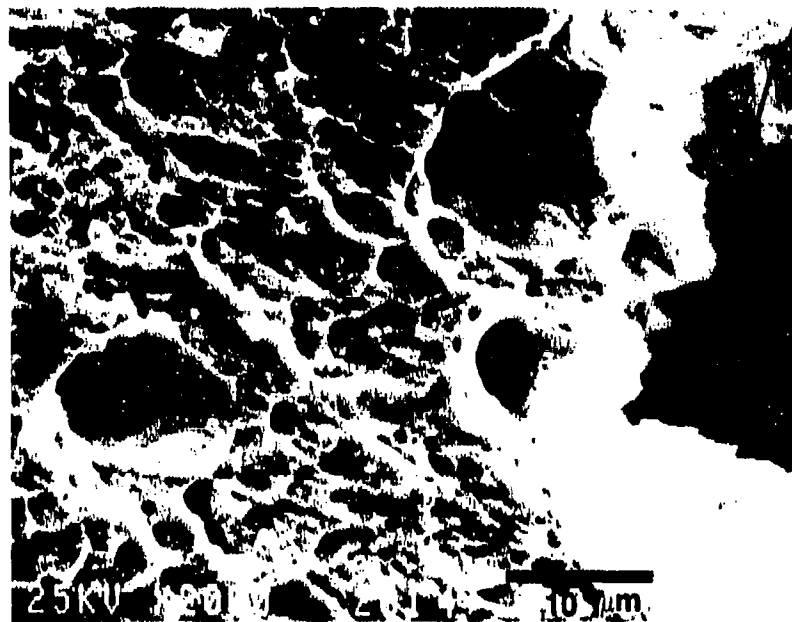


**b**

Figure 30. Scanning electron photomicrograph of tensile specimen GPF-4 tested at  $-75^{\circ}\text{C}$ . (a) Entire fracture surface showing the starburst pattern of deep, longitudinal cracks (10X). (b) Fracture surface morphology at the center of the fracture surface (200X).



a



b

Figure 31. Scanning electron photomicrograph of tensile specimen GFF-4. (a) Arrow points to a small longitudinal crack exhibiting ductile tearing (1000X). (b) Arrow points along the edge of a large longitudinal crack marked X in Figure 30a.(2000X).

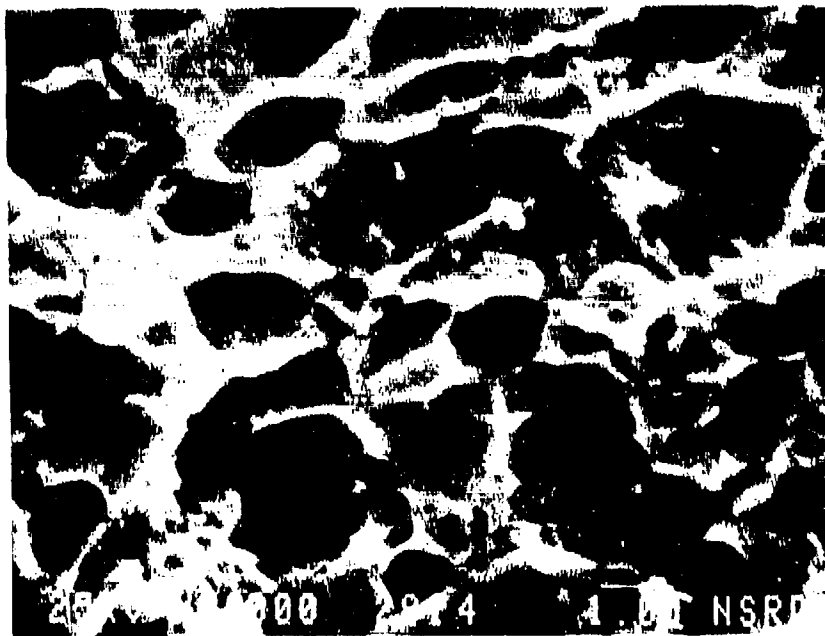
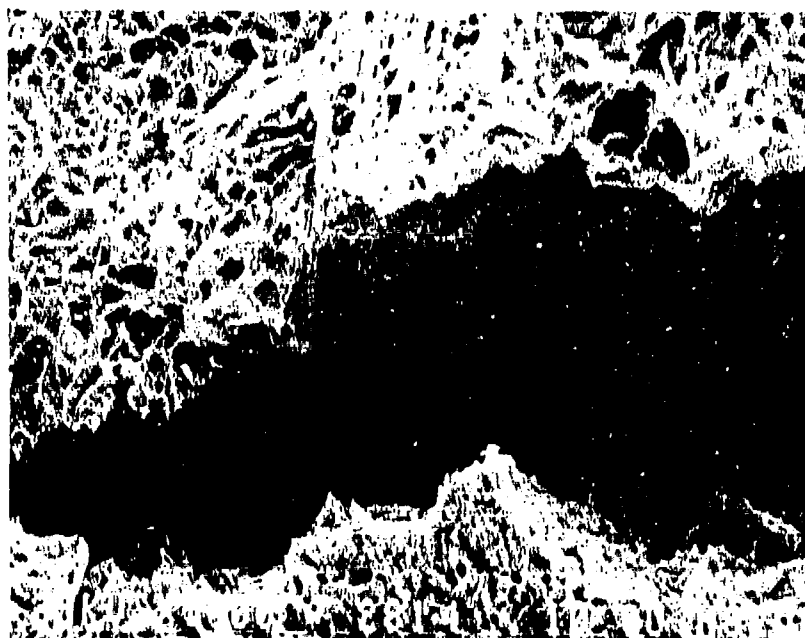
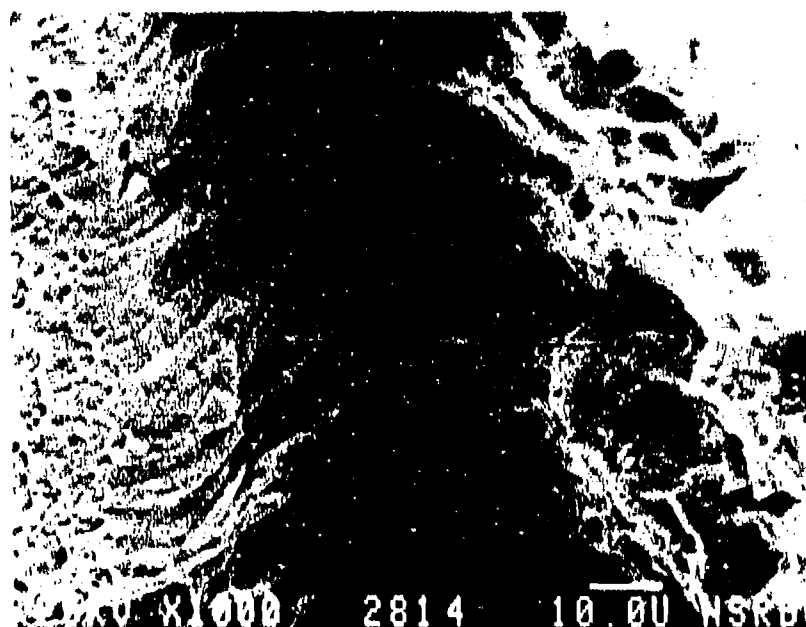


Figure 32. Scanning electron photomicrograph of the shear lip fracture area of tensile specimen GFF-2 tested at  $-18^{\circ}\text{C}$ . Average dimple diameter in this region is 1 micron (10,000X).



**a**



**b**

Figure 33. Scanning electron photomicrographs of regions of longitudinal cracking in tensile specimen GFF-2 tested at  $-18^{\circ}\text{C}$  showing the fracture mode to be microvoid coalescence (a) 1000X; (b) 1000X.

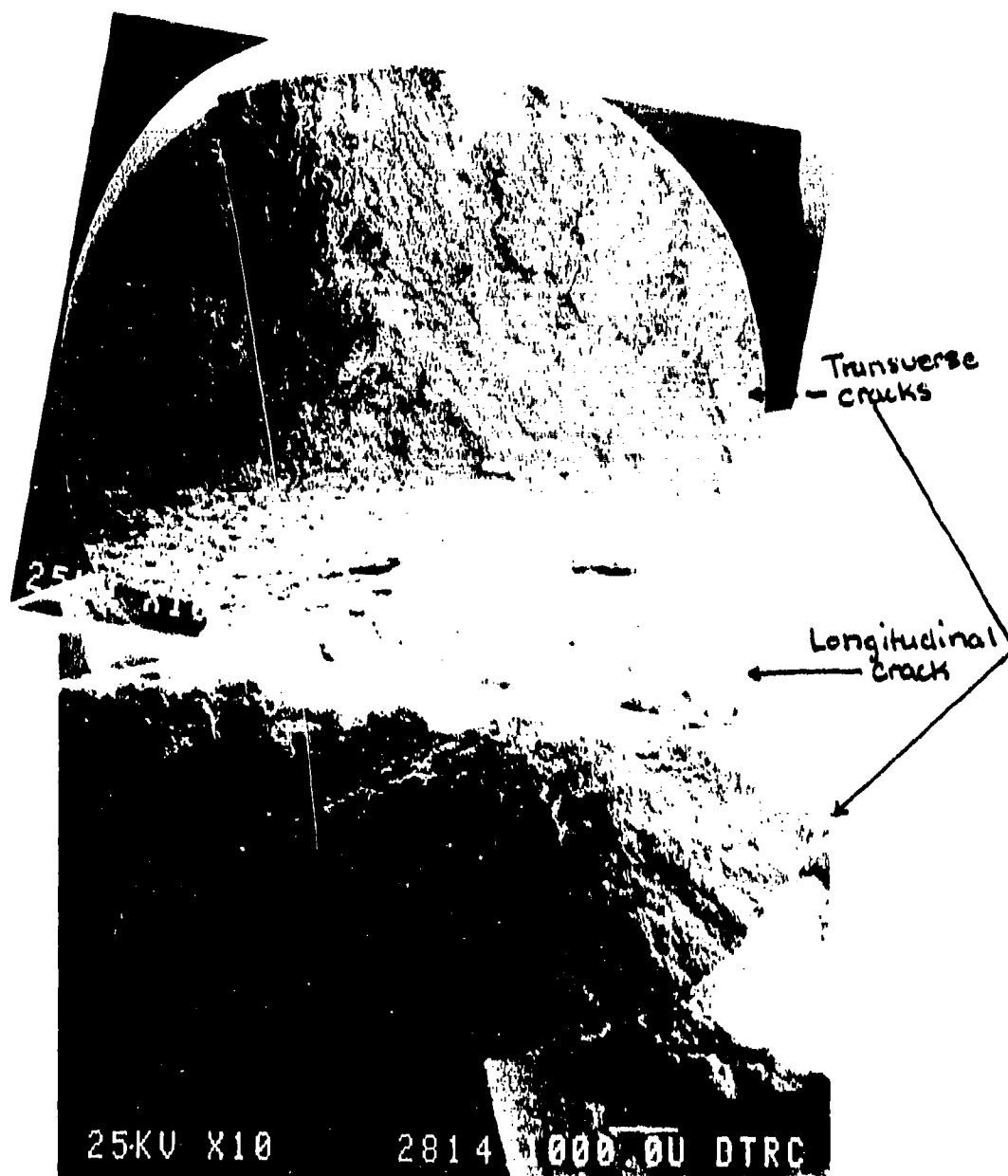
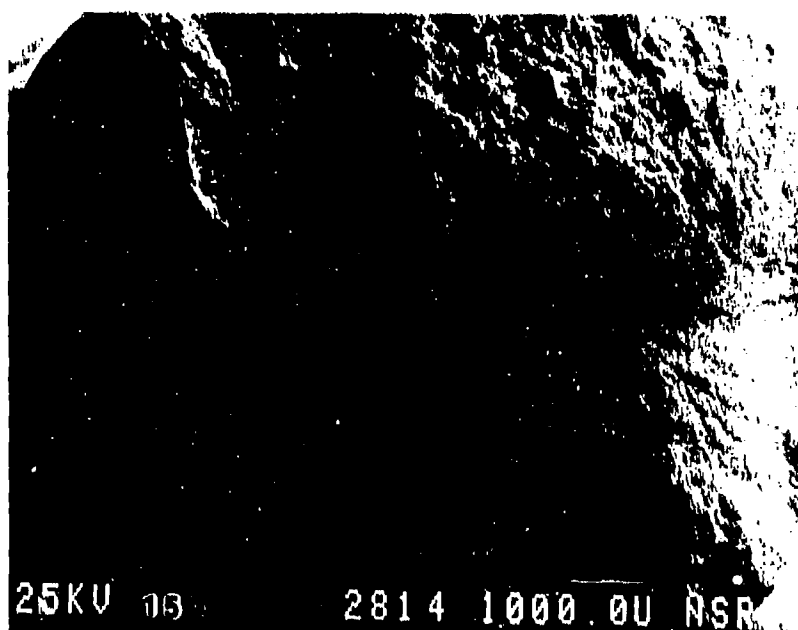


Figure 34. Scanning electron photomicrographs of one fracture surface from tensile specimen GFF-6 tested at  $-130^{\circ}\text{C}$  showing the transverse fracture surfaces on either side of the necked region of the specimen (10X).



**a**



**b**

Figure 35. Scanning electron photomicrographs of the matching fracture surfaces of tensile specimen GPF-7 tested at  $-130^{\circ}\text{C}$  (a) 10X; (b) 15X.



at either end of the necked region with cleavage crack initiation occurring in the area of the arrested longitudinal crack as shown in Figures 36 and 37. Figure 38 shows the appearance of the longitudinal crack region. The failure mode was cleavage but the cleavage facets exhibit the deformed fiber appearance, Figures 39 and 40, indicating that cleavage cracking did not occur until after appreciable plastic deformation.

Specimens from plate GGN did not exhibit a cup-and-cone fracture mode when tested at room temperature (22° C). Between 20° C and -75° C fracture occurred ductily, but with the starburst pattern of longitudinal cracks as shown in Figures 41-44. As in the specimens from plate GFF the crack growth mechanism in the center of the specimens was ductile, mode one, void coalescence, Figure 45. Some of the voids in this region exhibit an elongated appearance similar to the longitudinal cracks indicating that the mechanism of longitudinal crack growth was occurring at many places on the fracture surface to a small extent. This elongation of voids was more apparent towards the quarter diameter of the specimens as shown in Figure 46. Dimple diameter in this region varied greatly with the smallest dimple diameters on the order of 0.2 microns across while the largest dimples exceeded 150 microns. The longitudinal cracks had a ductile appearance with opening mode dimples apparent in some cracks, as in Figure 47, while others had



Figure 36. Scanning electron photomicrograph of the longitudinal crack in tensile specimen GFF-7 with ductile tearing exhibited at the edge of the crack while the rest of the fracture mode is cleavage (200X).

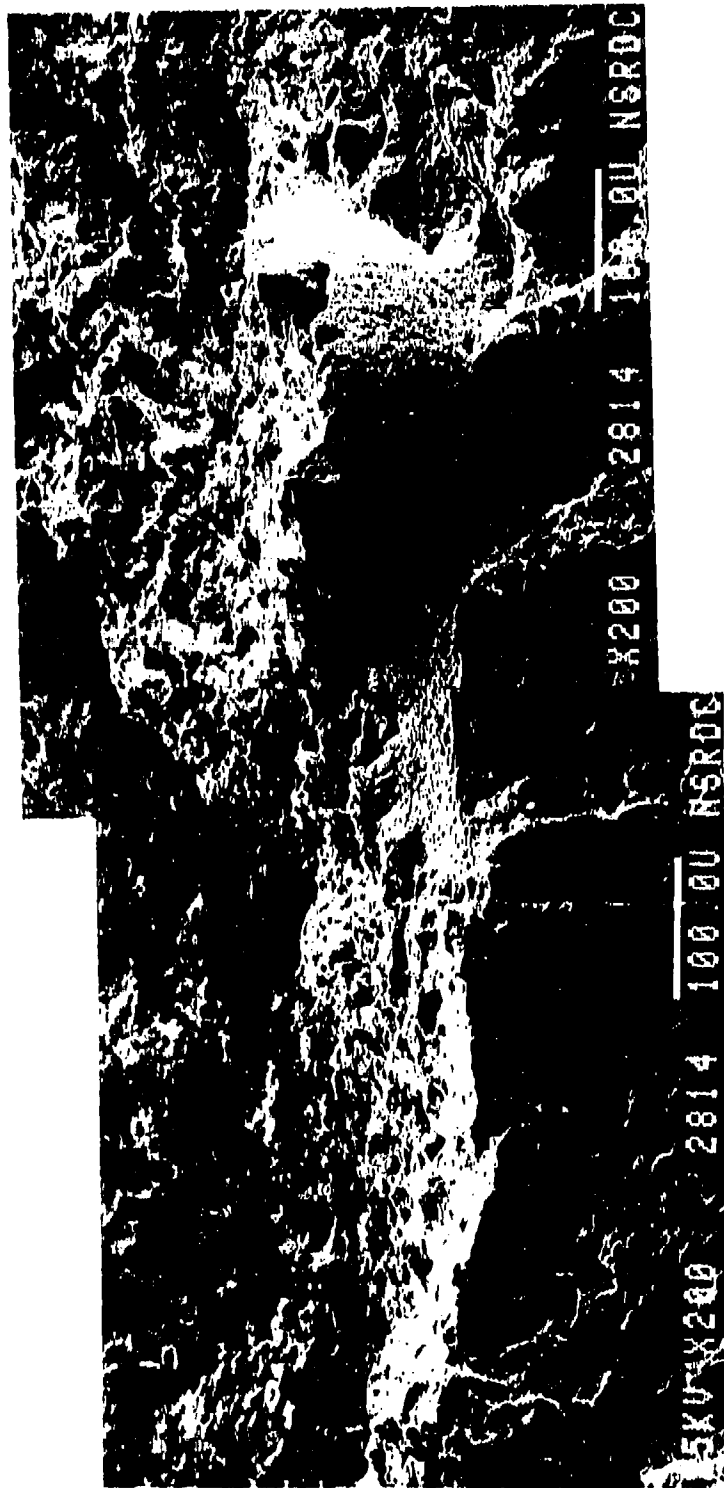


Figure 37. Scanning electron photomicrograph of the matching fracture surface to that in Figure 36 (200X).

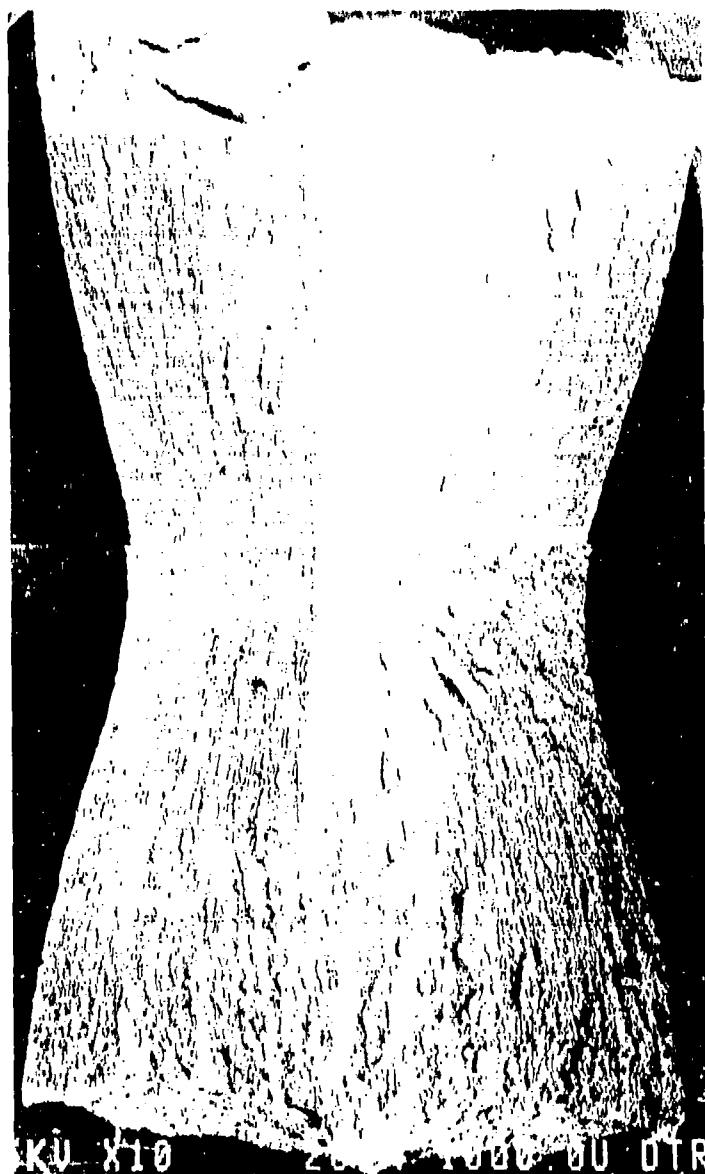


Figure 38. Scanning electron photomicrograph of the longitudinal crack in the necked region of tensile specimen GFF-8 tested at  $-150^{\circ}\text{C}$  showing mechanical fibering due to plastic deformation (10X).



Figure 39. Scanning electron photomicrograph of the longitudinal crack, shown in the previous figure, taken in the center of the necked region. Cleavage facets have a fine appearance due to the increased amount of deformation in this region (200X).

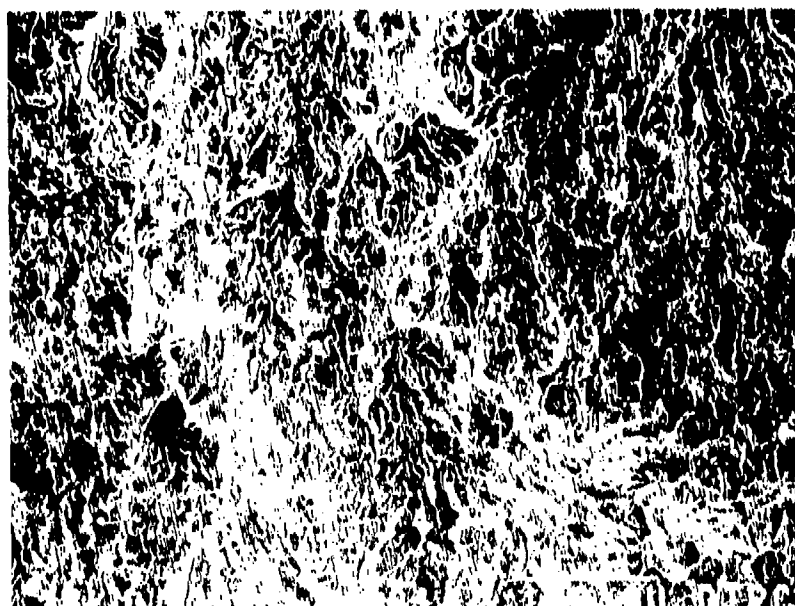


Figure 40. Scanning electron photomicrograph of the longitudinal crack, shown in the previous figure, in the region of crack arrest. Cleavage facets have a coarser appearance due to the limited amount of plastic deformation outside the neck (200X).



Figure 41. Scanning electron photomicrograph of matching fracture surfaces of tensile specimen GCN-150 tested at 22°C (10X).

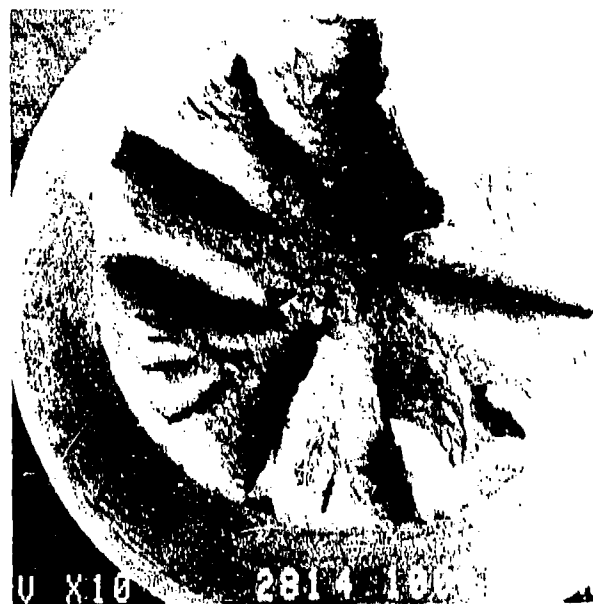


Figure 42. Scanning electron photomicrograph of matching fracture surfaces from tensile specimen GCN-151 tested at 22°C showing radial pattern of longitudinal cracks (10X).

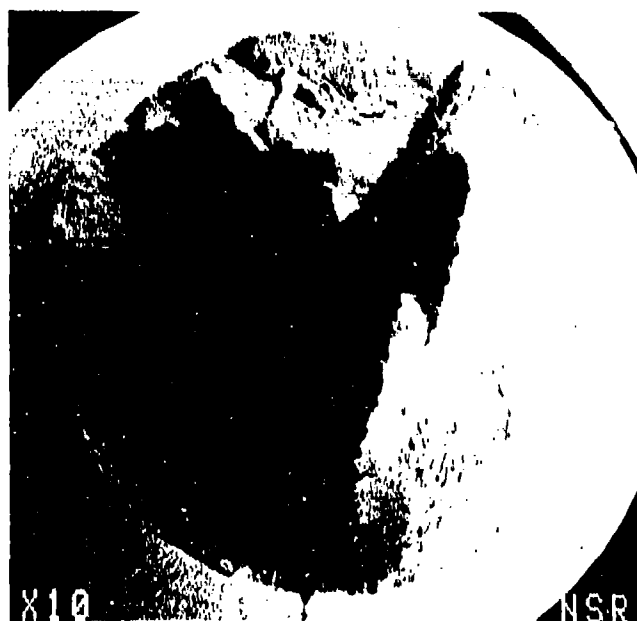


Figure 43. Scanning electron photomicrograph of matching fracture surfaces from tensile specimen GCN-152 tested at  $-18^{\circ}\text{C}$  showing a single, through diameter longitudinal crack with smaller, radial longitudinal cracks (10X).



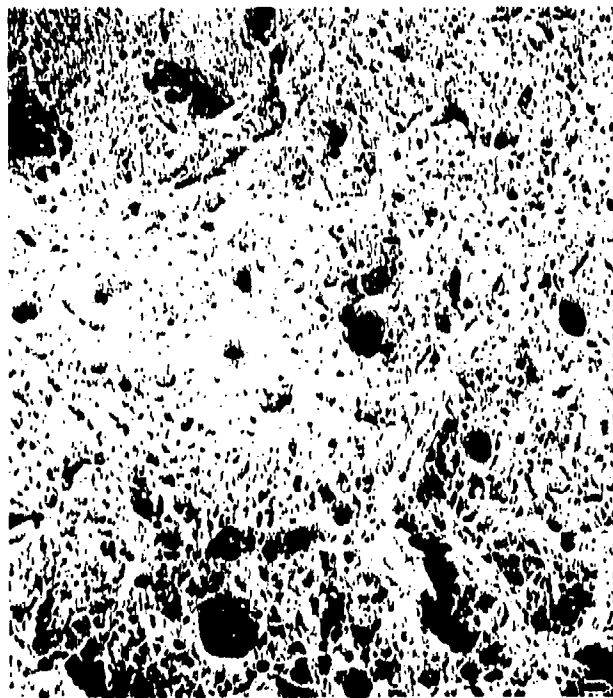


**a**

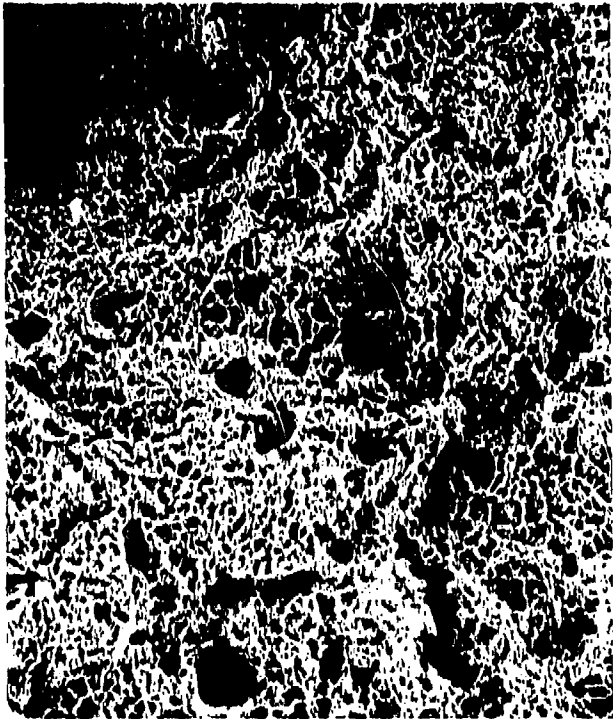


**b**

Figure 44. Scanning electron photomicrographs of matching fracture surfaces from tensile specimen GCN-153 tested at  $-200^{\circ}\text{C}$ . (10X)



**a**



**b**

Figure 45. Stereo electron fractographs of the central part of the fracture surface from tensile specimen GCN-153 tested at  $-20^{\circ}\text{C}$  (400X). (a)  $7^{\circ}$  tilt angle; (b)  $0^{\circ}$  tilt angle.



**a**



**b**

Figure 46. Stereo electron fractographs of the fracture surface near the outer edge of tensile specimen CGN-153 (400X).  
(a)  $7^{\circ}$  tilt angle; (b)  $0^{\circ}$  tilt angle.

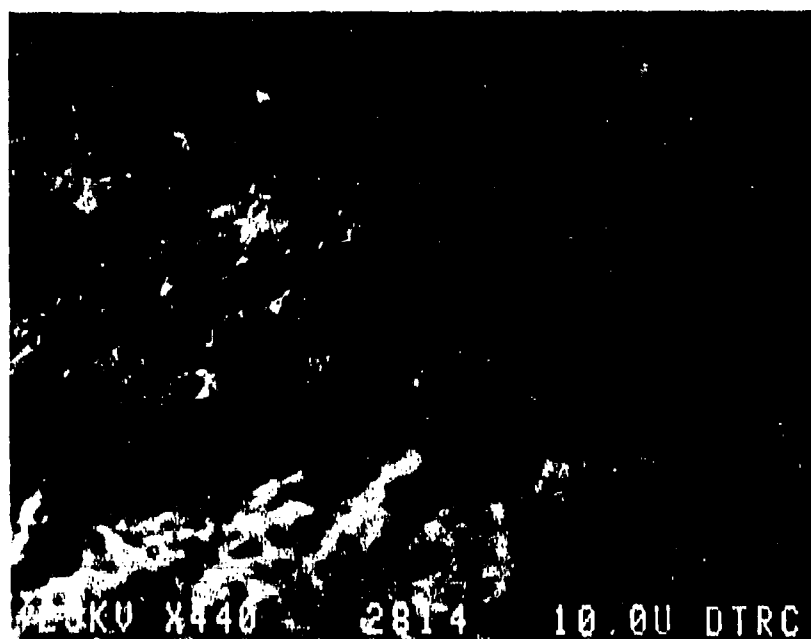
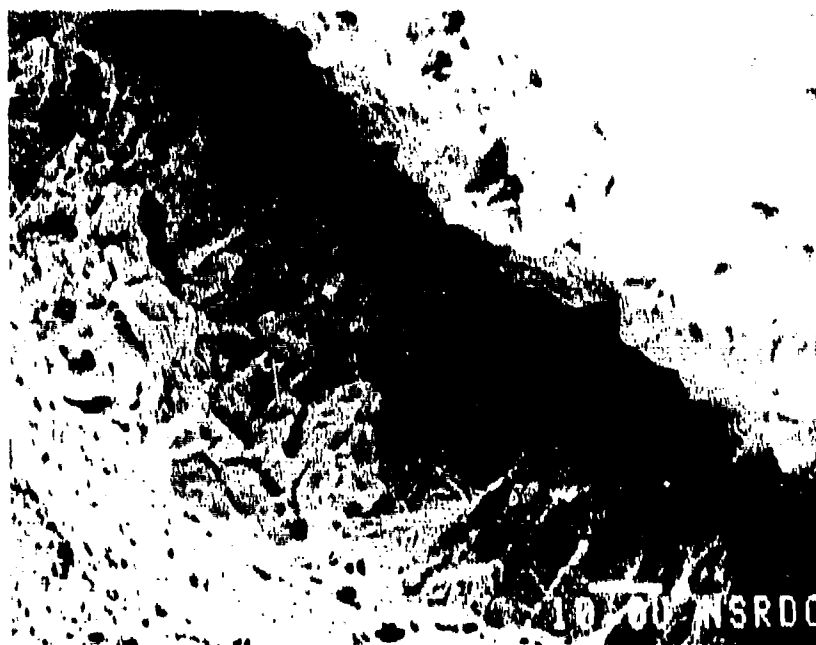


Figure 47. Scanning electron photomicrographs of the fracture surface of the longitudinal cracks in tensile specimen CGN-151 showing opening mode dimples (440X).

the appearance of extreme shear, as shown in Figure 48. In some areas around the outer circumference between longitudinal cracks, shear lip areas were apparent. The dimples on these areas were very small and more uniform in size than those found at the center of the fracture surface, Figure 49.

At temperatures between  $-75^{\circ}\text{C}$  and  $-125^{\circ}\text{C}$ , the fracture of both the longitudinal and transverse crack regions was a mixture of ductile void coalescence and cleavage cracking. These specimens tended to exhibit only one primary longitudinal crack as shown in Figures 50 and 51. The fracture area adjacent to the longitudinal crack had very elongated shear dimples as shown in Figure 52, while the rest of the transverse fracture surface had a mixed, cleavage and ductile, fracture mode appearance as shown in Figure 53.

Below  $-75^{\circ}\text{C}$  fracture was entirely cleavage in mode and occurred at either end of the single longitudinal crack which extended through the necked region of the specimen. Figure 54 shows the appearance of the transverse, final crack region of a specimen tested at  $-160^{\circ}\text{C}$ , while the fracture appearance of the longitudinal crack region is shown in Figure 55.

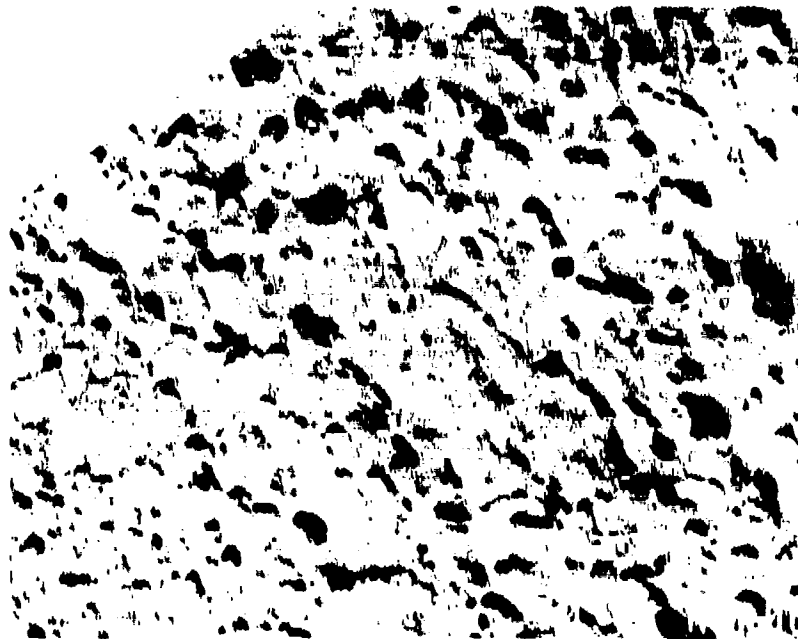


a

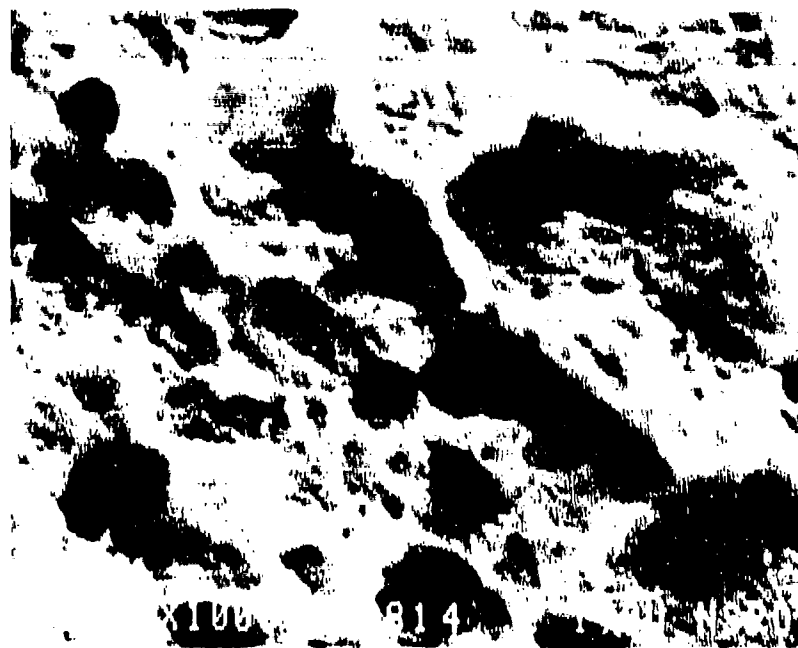


b

Figure 48. Scanning electron photomicrographs of the longitudinal crack fracture surfaces from specimen GCN-151 showing shear mode dimples. (a) 1000X; (b) 1000X.



**a**



**b**

Figure 49. Scanning electron photomicrographs of fracture surface of specimen CGN-150 in the shear lip area. Average dimple diameter is 1 micron. (a) 2000X; (b) 10,000X.

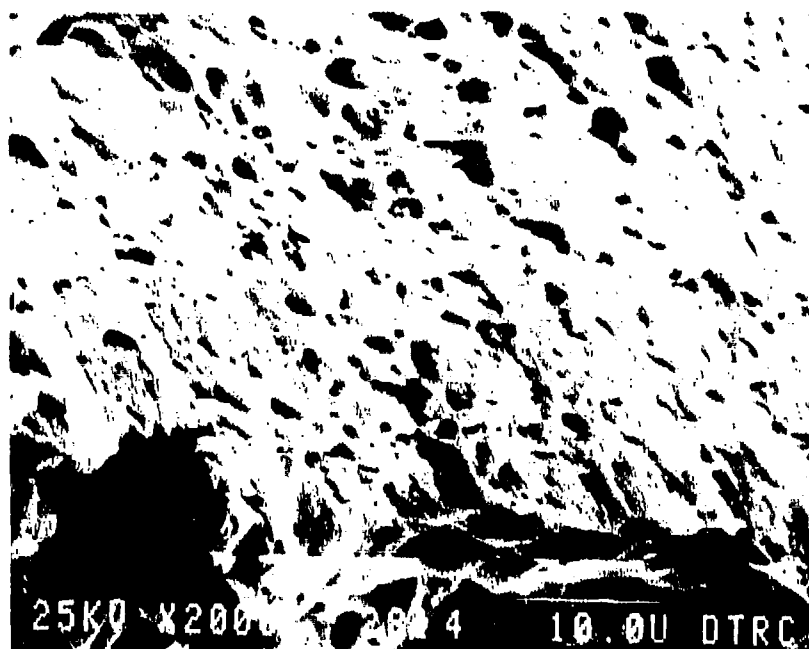


Figure 50. Scanning electron photomicrograph of matching fracture surfaces of tensile specimen GGN-155 tested at  $-45^{\circ}\text{C}$  showing a single, through diameter longitudinal crack (10X).

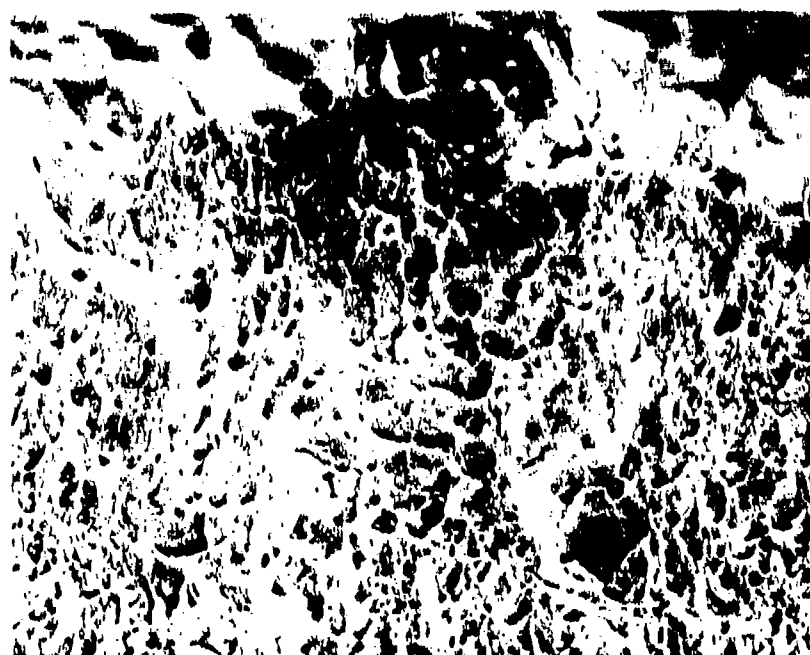




Figure 51. Scanning electron photomicrographs of matching fracture surfaces of tensile specimen GGN-156 tested at  $-73^{\circ}\text{C}$  showing a single through diameter longitudinal crack with a deep radial crack also apparent (10X).



a



b

Figure 52. Scanning electron photomicrographs of shear dimples on the transverse fracture surface adjacent to the longitudinal cracks on specimen GGN-156 (a) 1000X; (b) 2000X.

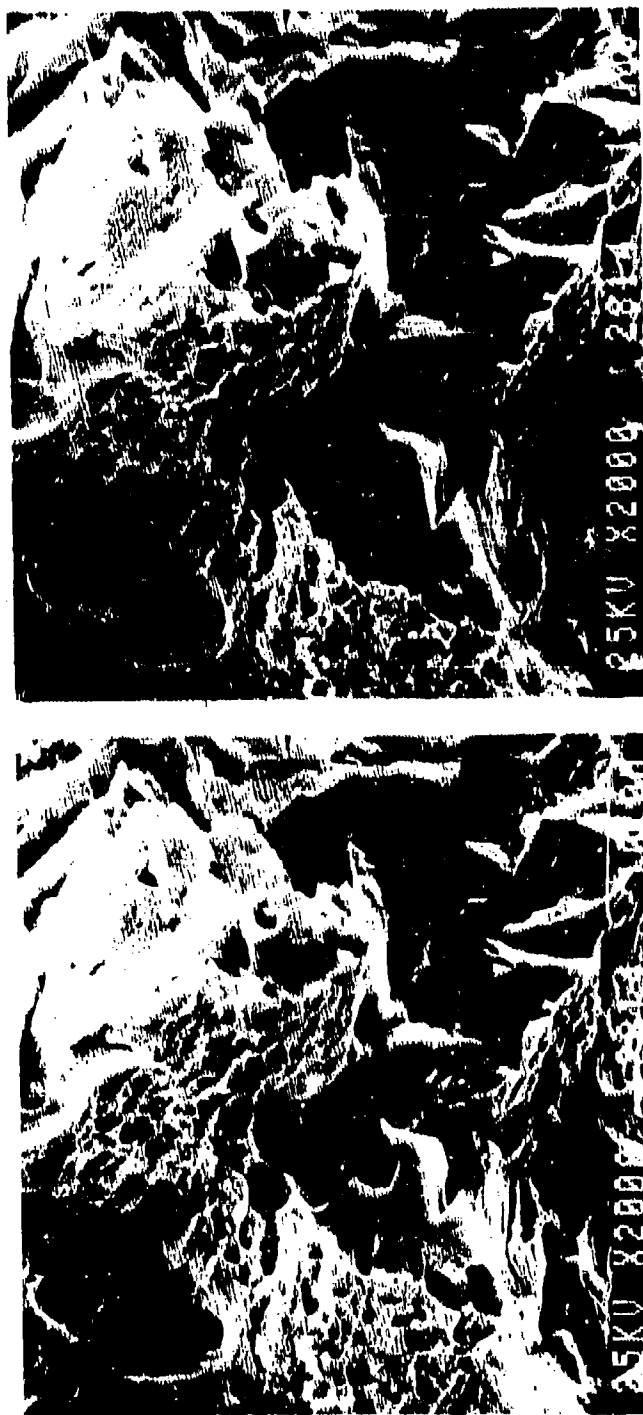


Figure 53. Scanning electron stereo-photomicrographs of the transverse fracture surface of specimen GCN-156 showing the fracture mode to be mixed cleavage and microvoid coalescence at  $-73^{\circ}\text{C}$  (2000X).

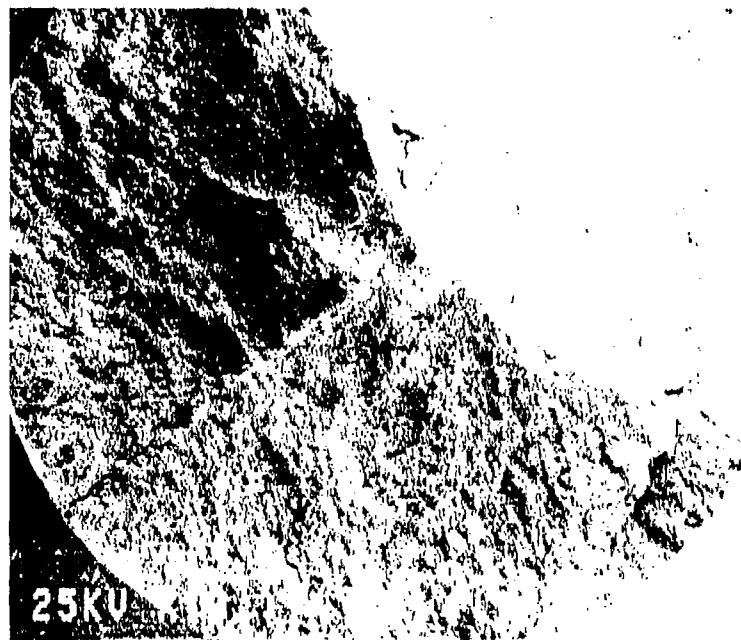
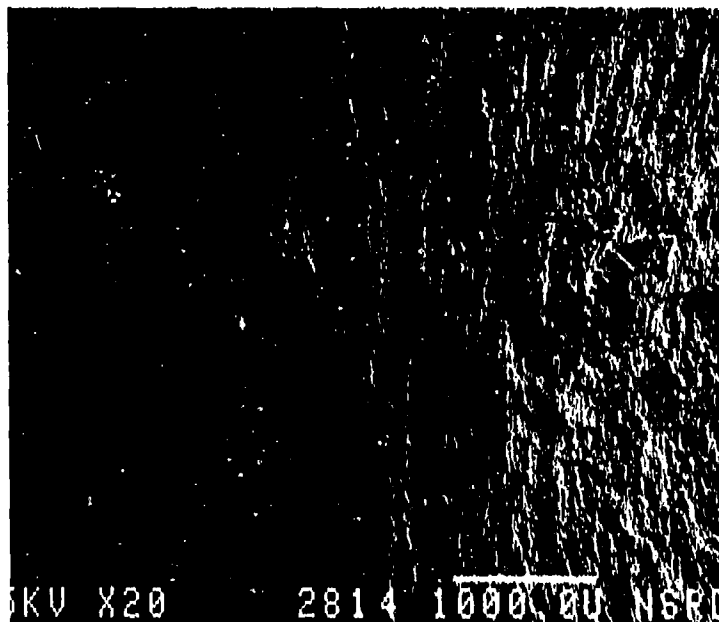


Figure 54. Scanning electron photomicrographs of matching transverse fracture surfaces of tensile specimen GCN-160 tested at  $-130^{\circ}\text{C}$  showing three longitudinal cracks which meet at the center of the specimen (10X).



**a**



**b**

Figure 55. Scanning electron photomicrographs of the longitudinal crack surface from tensile specimen GGN-160. (a) 20X; (b) 500X.

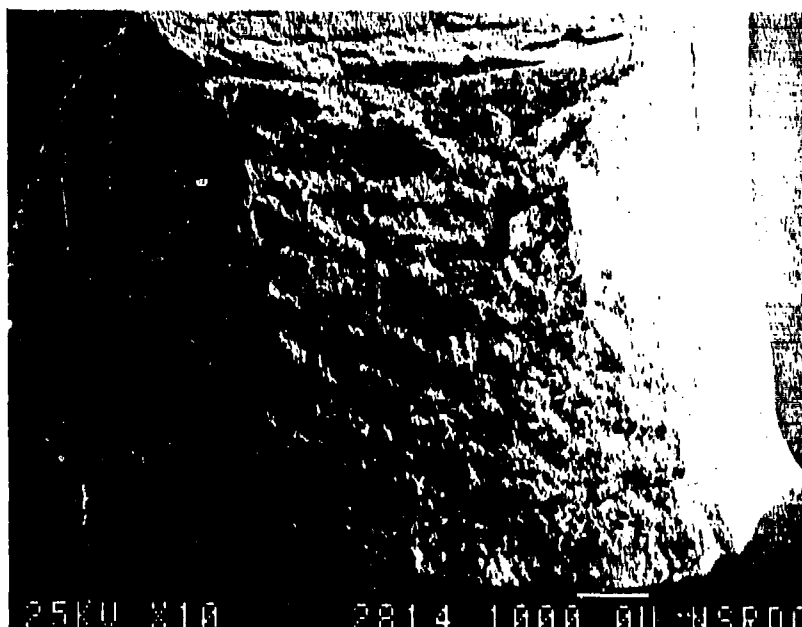
## Charpy Impact Fracture Mode Characterization

Testing of specimens from both plates was carried out over a range of temperatures to allow characterization of the full transition behavior of these plate materials.

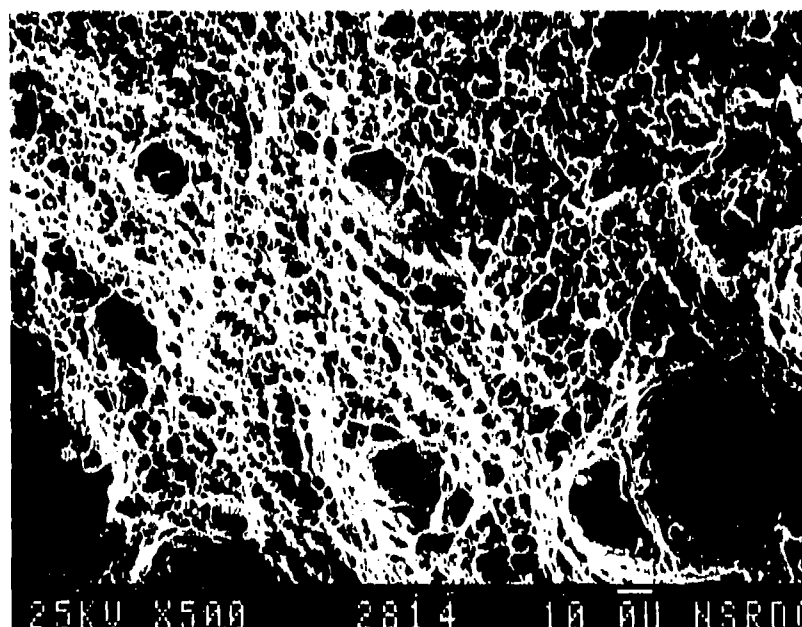
While it is not believed that the upper shelf energy for specimens from either plate was reached due to the limit of the Charpy impact apparatus and the number of specimens available for testing; full upper shelf fracture appearance was observed for specimens from both plates at room temperature, or slightly above.

The fracture appearance of specimens from both plates in the upper shelf energy region consisted of microvoid coalescence with lateral shear lips apparent. Figures 56-58 show the typical fracture appearance of Charpy impact specimens from each plate in the upper shelf region. The voids ranged in size from 1 to 140 microns with the majority of initiating particles identified as sulfides, oxides, or titanium nitrides.

In the transition region the fracture appearance transitioned from total microvoid coalescence to increasing amounts of cleavage fracture at the center of the specimens with decreasing test temperature. Fracture initiated in a ductile manner at the notch and then transitioned to cleavage at a distance from the notch. This distance (from the notch to the cleavage crack initiation site) decreased

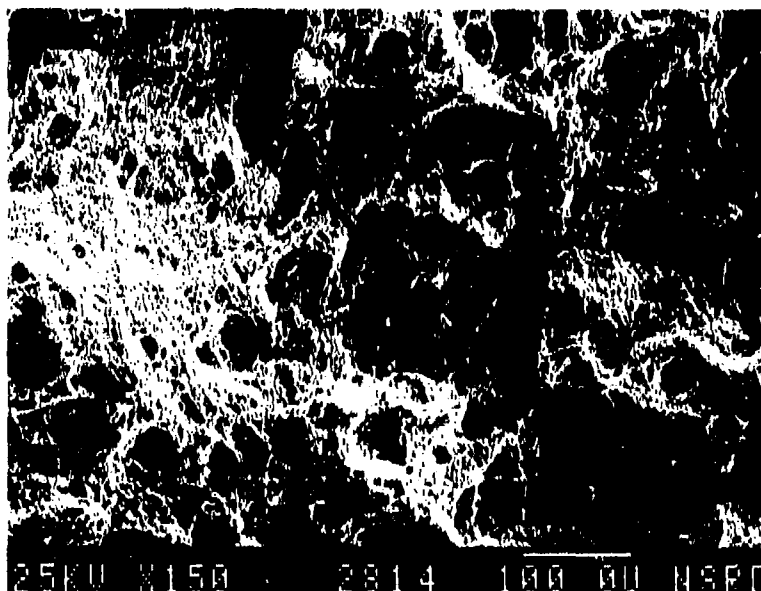


a

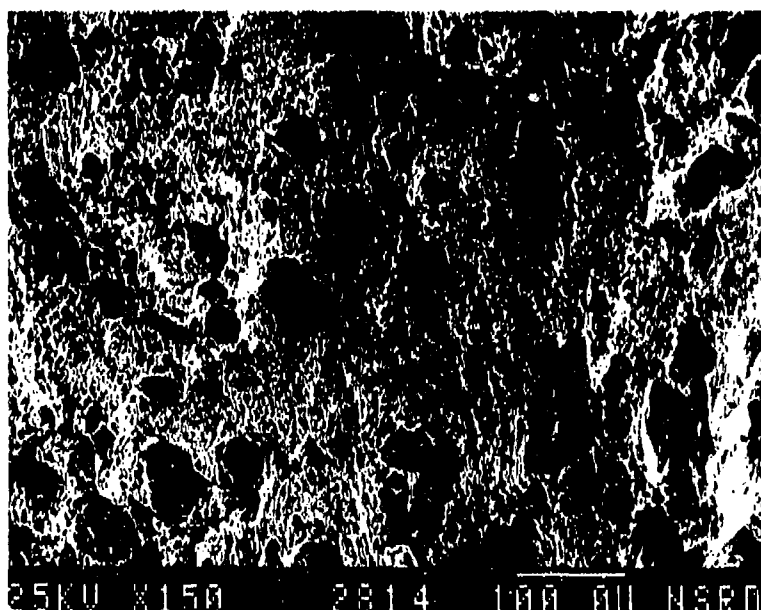


b

Figure 56. Scanning electron photomicrograph of the fracture surface of Charpy impact specimen GFF-116 tested at  $-62^{\circ}\text{C}$ . (a) Entire fracture surface at low magnification showing an appearance typical of upper shelf fracture behavior (10X). (b) Higher magnification of the central fracture surface showing a small area of cleavage fracture highlighted by the arrow (500X).



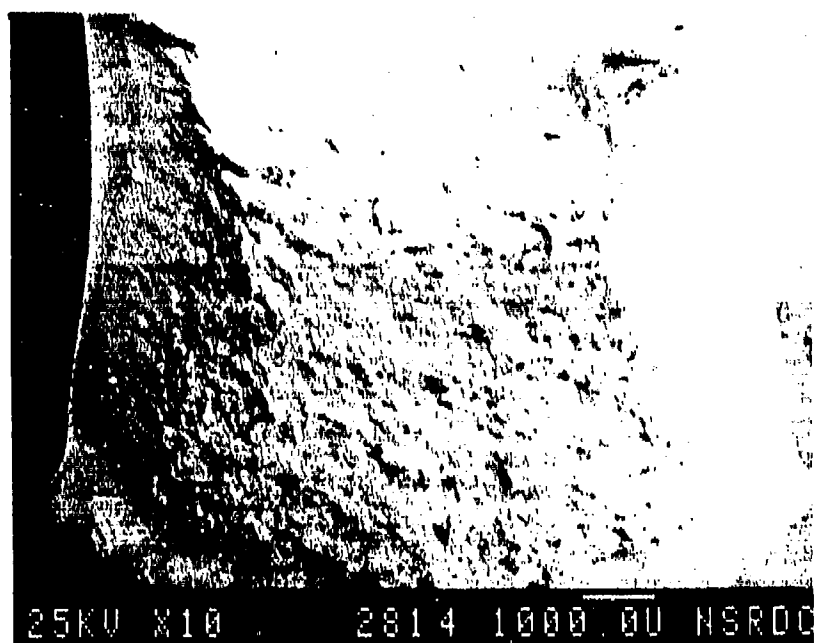
**a**



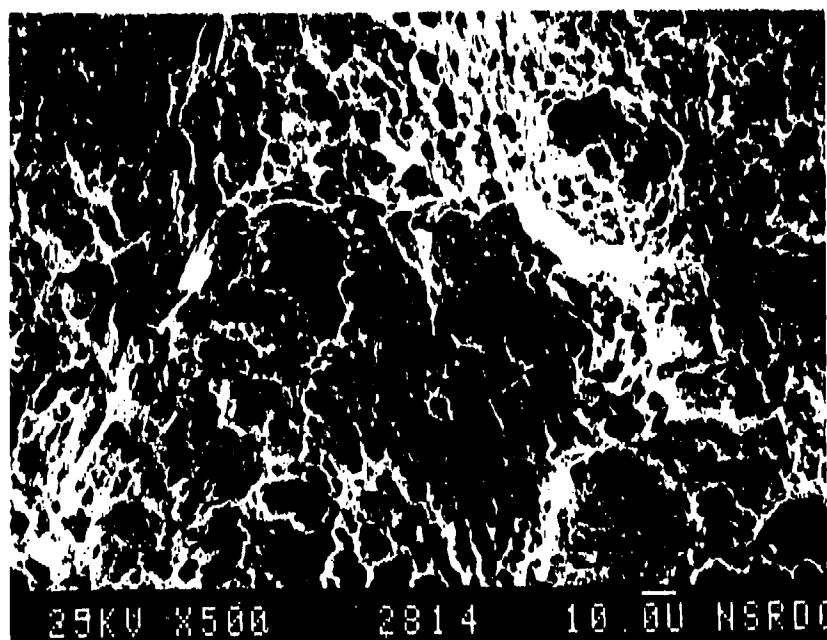
**b**

Figure 57. Scanning electron photomicrographs of the fracture surface of Charpy impact specimen GFF-116. (a) Typical fracture surface appearance at the center of the specimen (150X). (b) Typical fracture appearance at the edges of the specimen (150X).





**a**



**b**

Figure 58. Scanning electron photomicrographs of the fracture surface of Charpy V-notch specimen GGN-128 tested at 22°C showing the fracture mode at this temperature to be microvoid coalescence (a) 10X, (b) 500X.

with decreasing test temperature. At the lowest test temperatures ( $-160^{\circ}\text{C}$ ) specimens from both plates failed in an entirely brittle manner.

The cleavage initiation sites were characterized throughout the transition region with the initiating facet size, initiating particle and the distance of the initiation site from the notch, identified and measured. These parameters are listed versus test temperature for specimens from each plate in Table 5.

TABLE 5

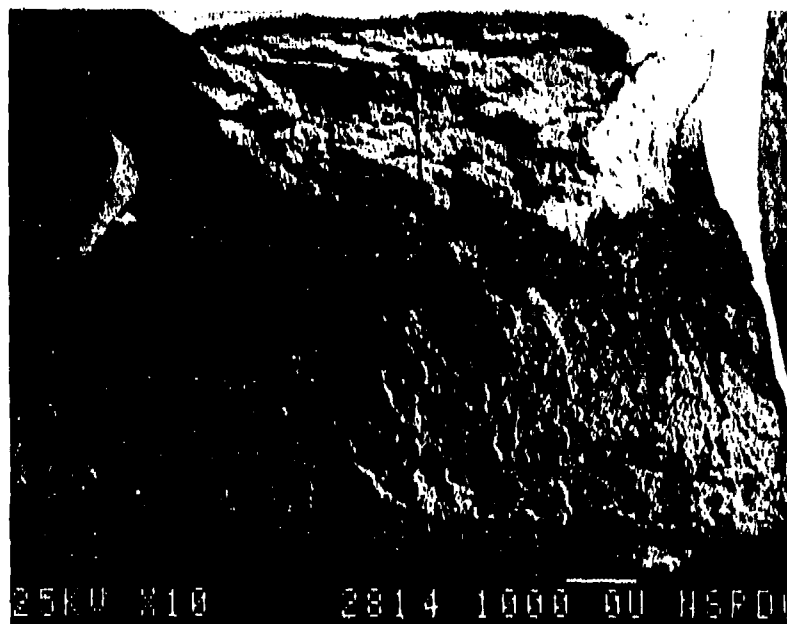
Specimen	Test T (°C)	Energy (J)	Initiation Facet Size (microns)	Initiating Particle	Cleavage Initiation Distance*	
					(r)	(X)
Plate GGN						
129	-130	7	35	oxide		200
119	-130	8		oxide	200	300
107	-118	19	32	nitride		750
127	-100	26	17	sulfide	140	550
117	-100	58	34	carbide	700	1400
106	-100	11	34	**		800
126	-84	71	41	oxide	400	710
116	-84	7	57	nitride		260
105	-84	9	64	**		280
115	-68	91	60	nitride	750	2100
104	-68	174	35	carbide	140	320
124	-51	176	37	carbide	450	3200
114	-51	33	25	oxide	140	500
103	-51	190	72	nitride	300	3300
120	38	211	55	oxide	1000	4200
Plate GFF						
100	-118	27	35	**	320	500
111	-118	33	40	**	350	600
133	-118	207	34	carbide	250	3900
143	-118	193	55	carbide	420	3410
112	-107	179	57	oxide	800	3600
134	-107	176	73	sulfide	280	3200
135	-95	205	42	**	140	4900
145	-95	233	30	nitride	120	4800
146	-84	275	40	nitride	70	4600
104	-73	297	28	nitride	100	5800
115	-73	290	75	oxide	300	4800

\* Cleavage initiation distance is the distance to the cleavage initiation site from either the notch (X), or the growing ductile crack tip (r).

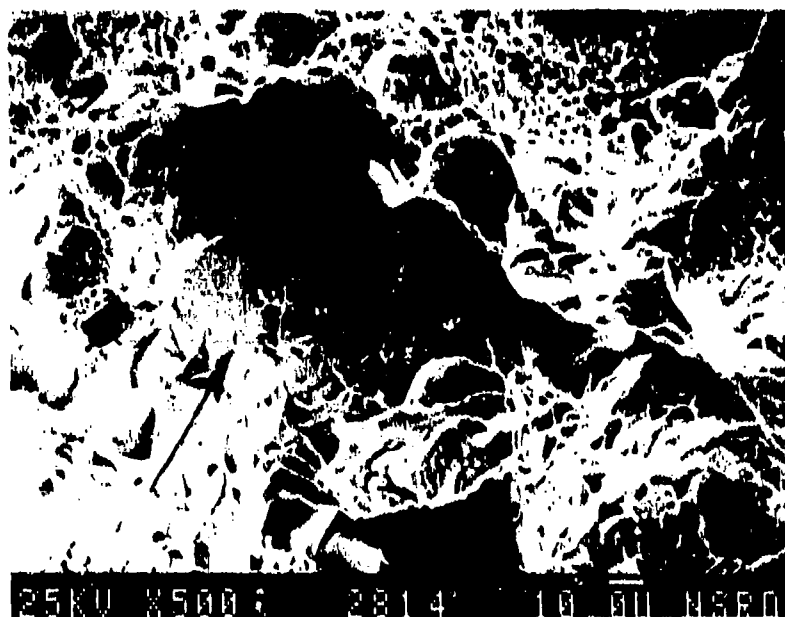
\*\* No cleavage initiating particle identified.

Table 5. Charpy V-notch cleavage initiation data measured from fractographs taken of each specimen.

The cleavage initiating facets and particles were identified by following the cleavage "river" pattern back to the point of initiation. Stereo fractographs made this identification easier at higher magnifications since it allowed full topographic characterization of the fracture surfaces. Figures 59-62 show the fracture surface characteristics of specimens from each plate tested in the ductile-to-brittle transition region. Cleavage crack initiating precipitates were identified as titanium nitrides and manganese sulfides in most cases but in some, Figure 62, no precipitate was observed. Cleavage initiation occurred within several hundred microns of the ductile crack growth region but the distance between the cleavage initiation site and the notch decreased with decreasing test temperature. The region of ductile crack growth also decreased with test temperature, while the distance between the growing ductile crack and the cleavage initiation site remained about constant over the transition temperature range. At the lowest test temperatures, very little, or no ductile crack growth was observed prior to the onset of cleavage fracture initiation, Figures 63-66.

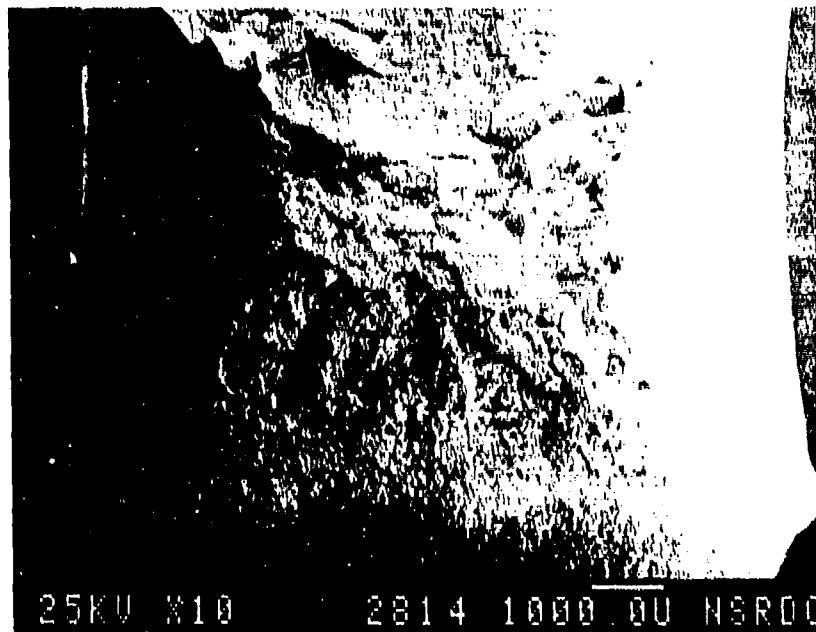


**a**

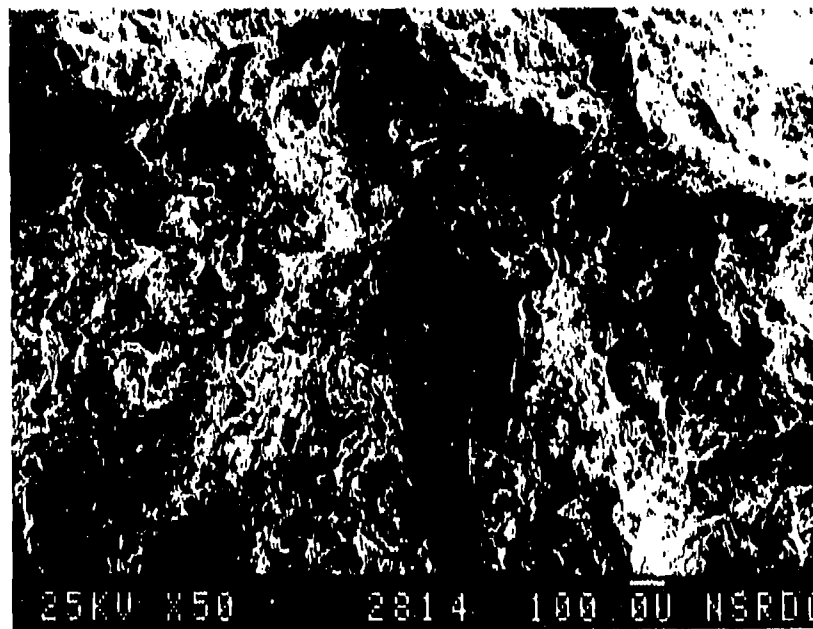


**b**

Figure 59. Scanning electron photomicrograph of the fracture surface of Charpy impact specimen GPF-134 tested at  $-105^{\circ}\text{C}$ . (a) Entire fracture surface with the arrow showing the cleavage initiation region (10X). (b) Cleavage initiation site (arrow) (500X).



**a**



**b**

Figure 60. Scanning electron photomicrographs of the fracture surface of Charpy impact specimen GGN-120 tested at 37°C. (a) Entire fracture surface at 10X. (b) Cleavage initiation region (50X).

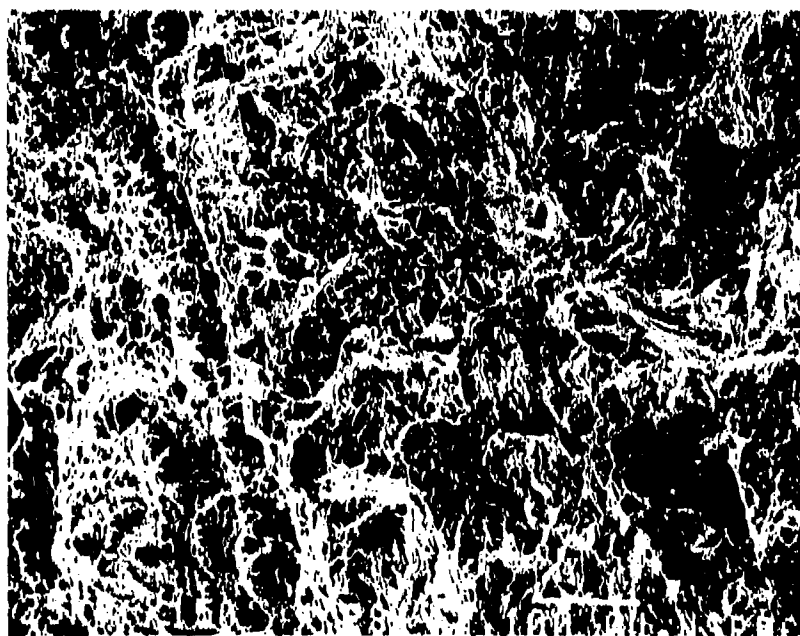
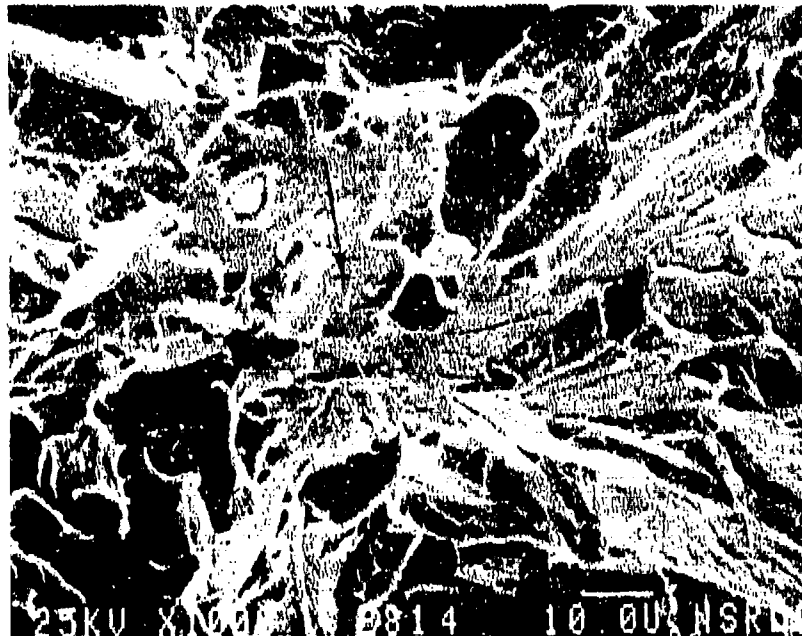


Figure 61. Scanning electron photomicrograph of the fracture surface of Charpy impact specimen GGN-124 tested at  $-50^{\circ}\text{C}$ . (a) Entire fracture surface (10X). (b) Ductile-to-brittle transition zone with the cleavage initiation site shown by the arrow (150X).



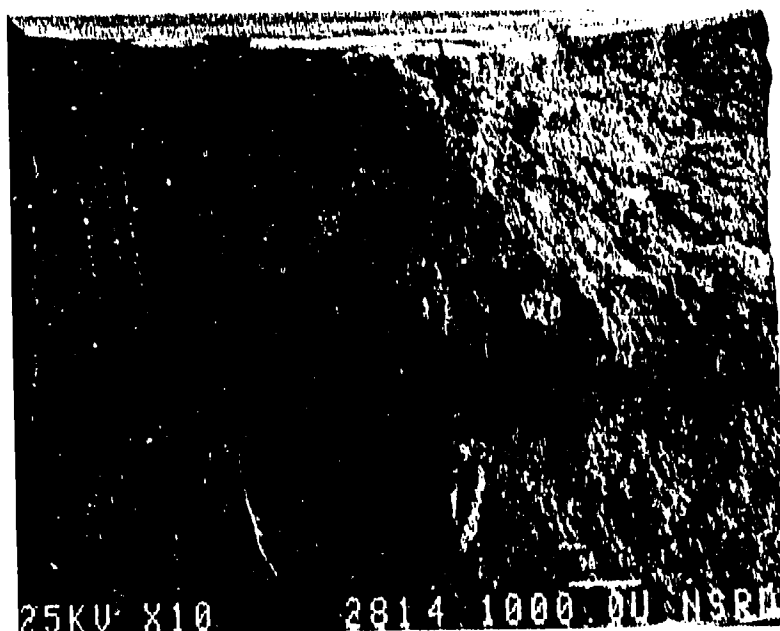
**a**



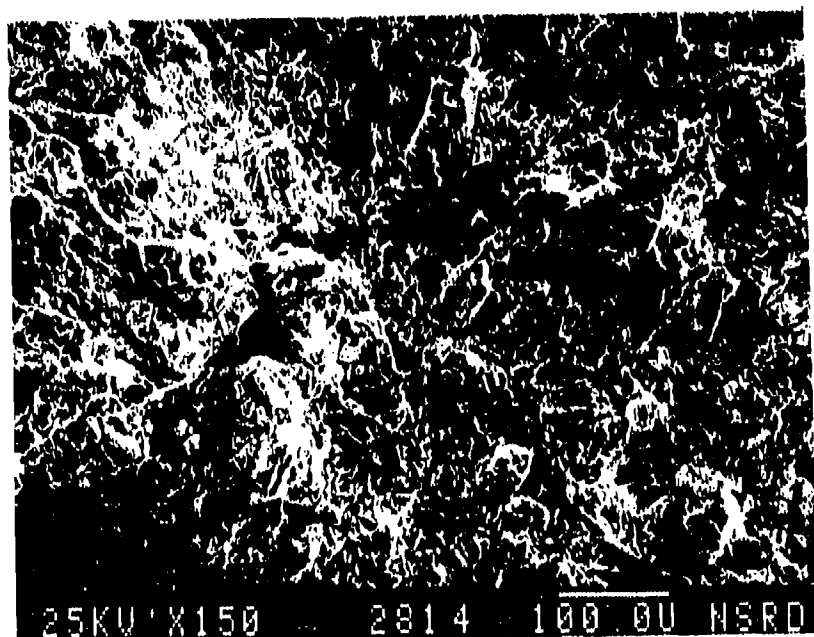
**b**

Figure 62. Scanning electron photomicrograph of the fracture surface of Charpy impact specimen GGN-124. (a) The cleavage initiation facet shown by the arrow (100X). (b) The cleavage initiation site shown by the arrow (10,000X).





**a**



**b**

Figure 63. Scanning electron photomicrograph of the fracture surface of Charpy impact specimen GFF-111 tested at  $-120^{\circ}\text{C}$ . (a) Entire fracture surface with the arrow showing the cleavage fracture initiation region (10X). (b) Higher magnification of the cleavage fracture region (150X).

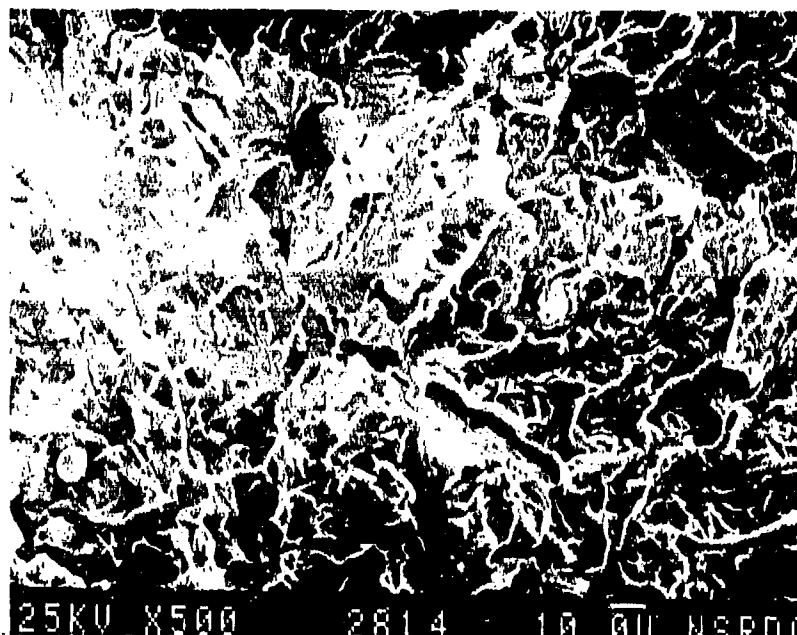
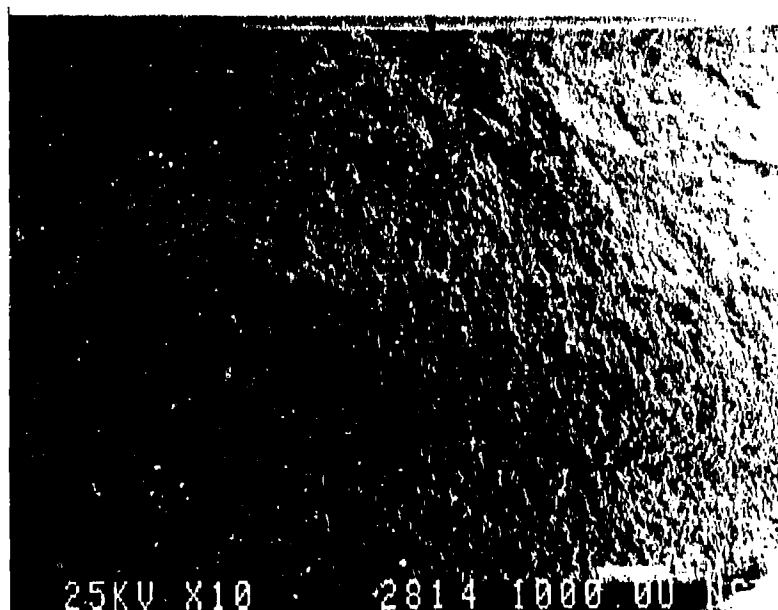


Figure 64. Scanning electron photomicrograph of the cleavage initiation site of Charpy impact specimen GFF-111 tested at  $-120^{\circ}\text{C}$  (500X).



**a**



**b**

Figure 65. Scanning electron photomicrograph of the fracture surface of Charpy impact specimen GGN-108 tested at  $-130^{\circ}\text{C}$ . (a) Low magnification of the entire surface with the arrow pointing to the cleavage crack initiation site (10X). (b) Higher magnification of the cleavage initiation site (150X).

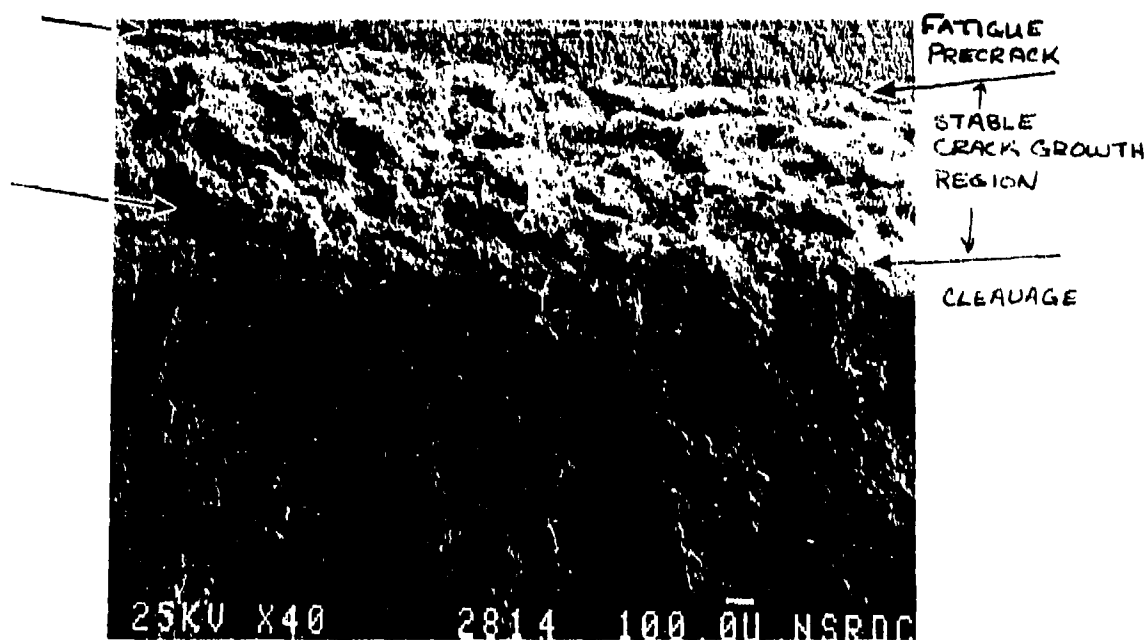


Figure 66. Scanning electron photomicrograph of the cleavage initiation site on the fracture surface of Charpy impact specimen GGN-108 tested at  $-130^{\circ}\text{C}$  (3000X).

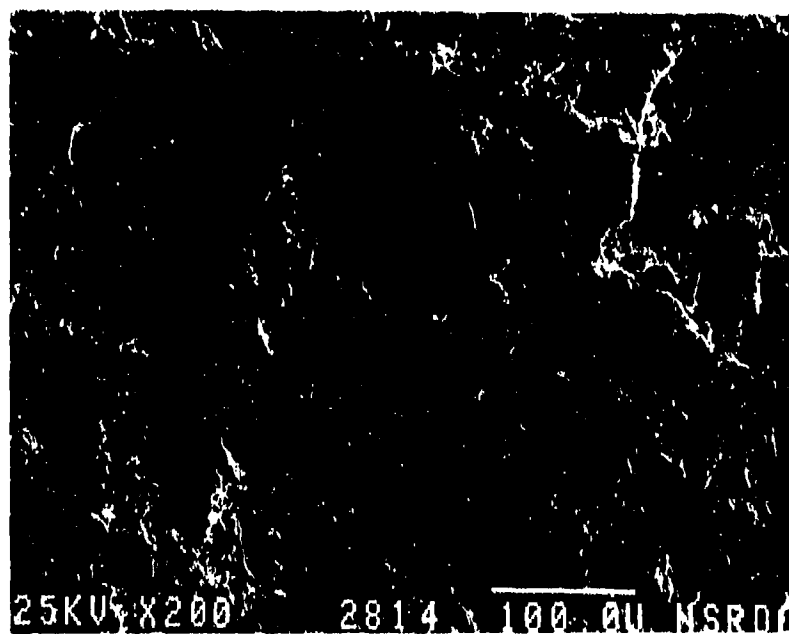
## Fracture Toughness Specimen Fracture Mode Characterization

25.4 mm thick compact specimens were tested over a wide range of test temperatures to allow full characterization of the transition fracture toughness behavior of the two plates. The ductile, upper shelf, and brittle, lower shelf temperature ranges were determined and then the bulk of testing was done between these temperatures to evaluate the ductile-to-brittle transition behavior of the specimens. At room temperature, specimens from both plates exhibited stable ductile crack growth behavior.

The ductile-to-brittle transition temperature ranges were different for the two plate materials with specimens from plate GFF exhibiting a wide transition temperature range centered about  $-90^{\circ}\text{C}$ , as shown in Figure 24, while specimens from plate GGN exhibited a very narrow transition temperature range, centered about  $-10^{\circ}\text{C}$ , also shown in Figure 24. The fracture behavior of specimens from both plates varied widely in the transition regions with no apparent relationship between decreasing test temperature and decreasing length of the ductile zone. This is shown both in the wide range of scatter between the energies required for the initiation of stable crack growth and the initiation of unstable cleavage in the same specimens, and in the measurement of the width of the ductile crack growth region on each specimen. Figures 67 and 68 show the



a



b

Figure 67. Scanning electron photomicrograph of the fracture surface of fracture toughness specimen GGN-27 tested at  $-10^{\circ}\text{C}$ . (a) Low magnification of the cleavage initiation region (arrow), including the region of stable crack growth (40X). (b) Cleavage initiation region (200X).

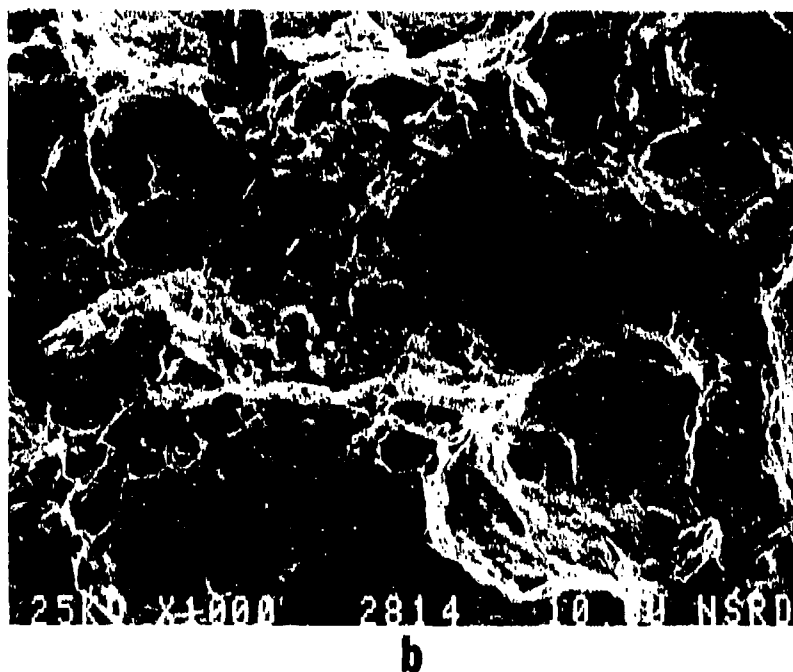
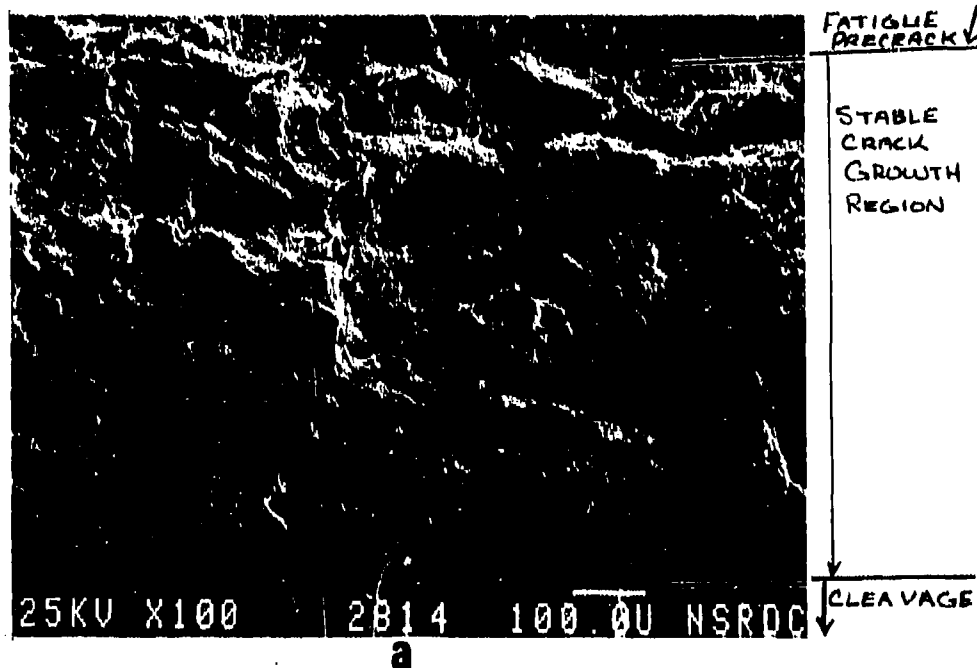


Figure 68. Scanning electron photomicrograph of the stable crack growth region of GGN-27. (a) Entire width of the stable crack growth region (100X). (b) Dimple morphology in the stable crack growth region (1000X).

microvoid morphology in the ductile crack growth region of specimen GGN-27 which was tested in the upper transition temperature region. All specimens exhibited a dual distribution of microvoid diameters as shown in the graph of microvoid diameters for specimen GGN-27 in Figure 69. The microvoid initiating particles varied with sulfides the most common initiating particle identified in the larger voids. Figures 70 and 71 show the cleavage initiation region and initiating particle for specimens GGN-27 and GGN-30, both of which exhibited an amount of stable crack growth prior to cleavage initiation. In both cases a titanium nitride particle of approximately 0.75 microns in diameter was identified as the initiating particle. Figure 72 shows stereo photomicrographs of the cleavage initiation region from specimen GFF-11 which failed entirely by cleavage. Figure 73 shows higher magnification SEM photomicrographs of the actual cleavage initiating particle identified as a manganese sulfide particle which was approximately one micron in diameter.

Figure 74 shows the matching fracture surfaces from specimen GFF-2 which was tested at  $-100^{\circ}\text{C}$ , the low end of the transition temperature region. A zone of ductile crack growth was apparent on this fracture surface but it extended less than one hundred microns from the notch and did not extend across the entire width of the specimen. This was typical of the fracture appearance of specimens



## GRAIN AND DIMPLE SIZE DISTRIBUTION Plate GGN

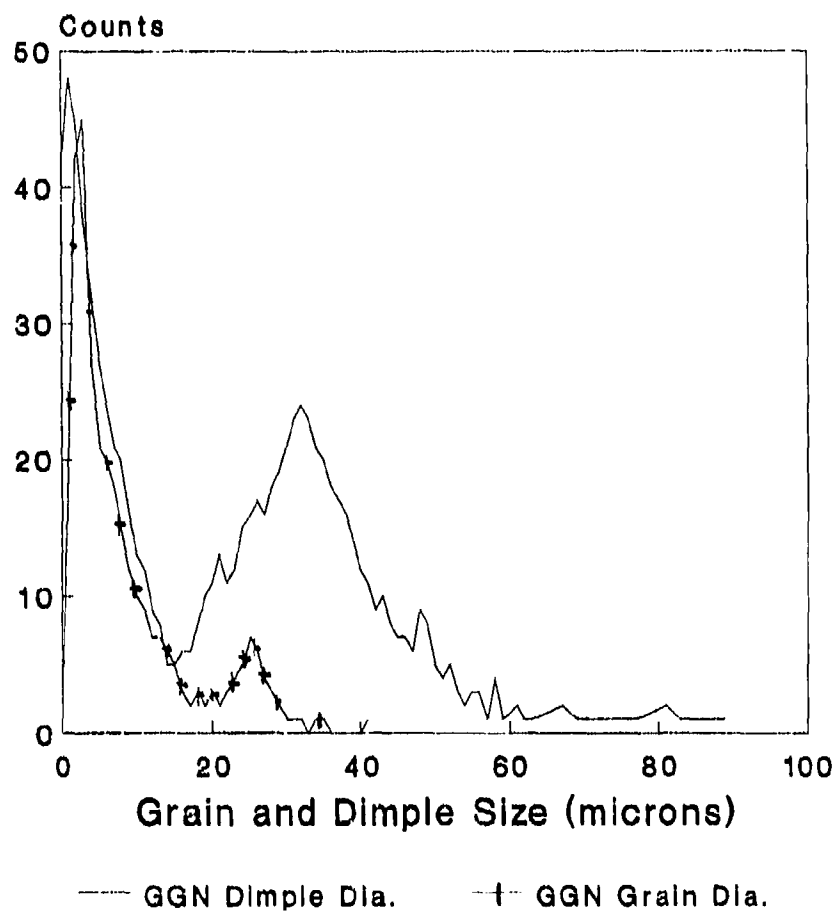
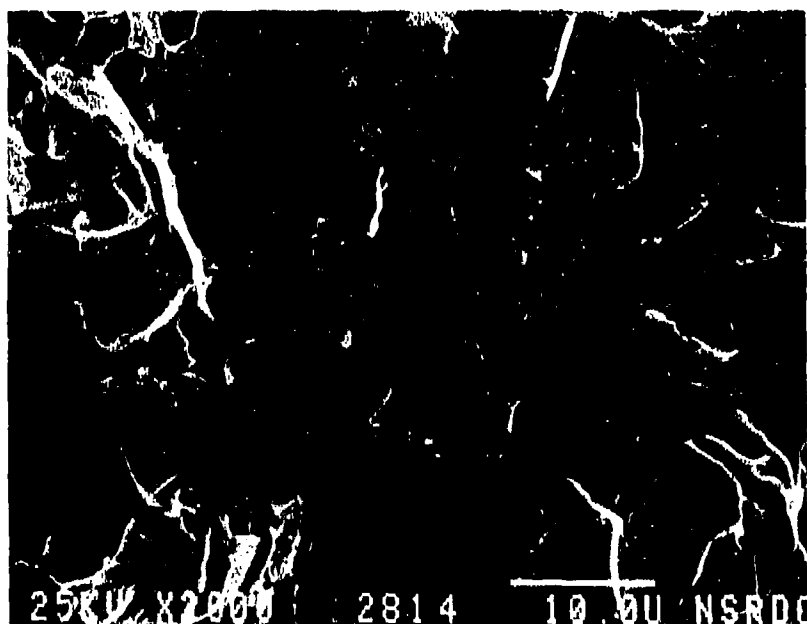
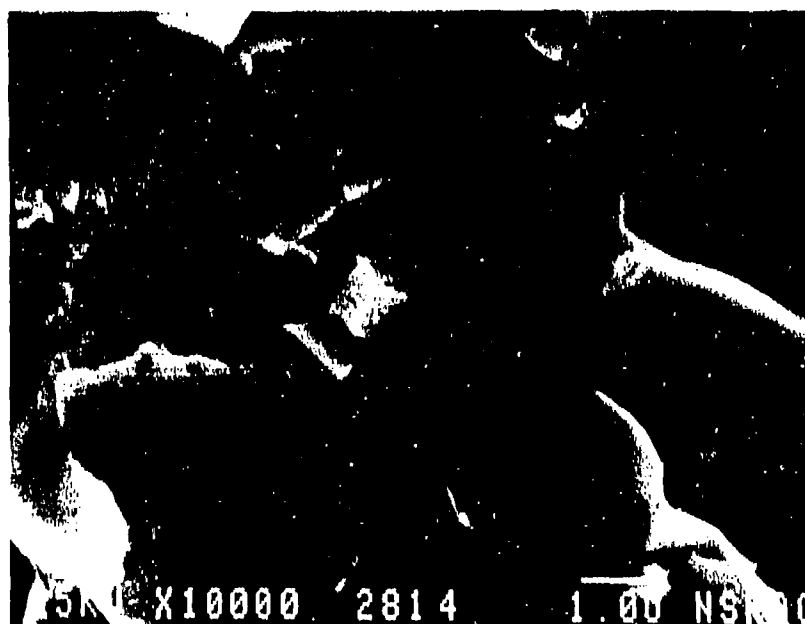


Figure 69. Plot of the dimple diameter distribution as measured from specimen GGN-27 compared to the plate GGN grain size distribution.



**a**

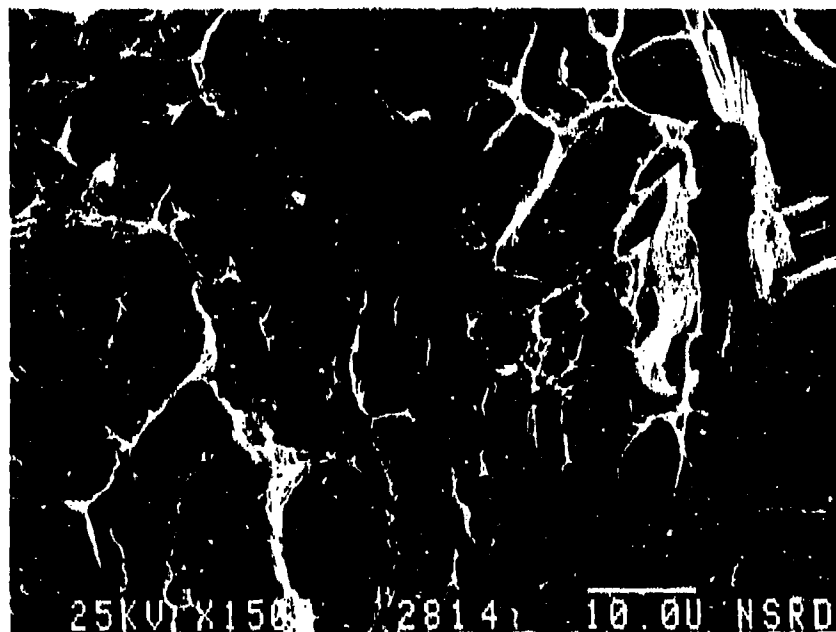


**b**

Figure 70. Scanning electron photomicrograph of the cleavage initiation region of GGN-27. (a) Arrow points to the cleavage initiation facet (2000X). (b) Arrow points to the initiating titanium nitride particle (10,000X).



a

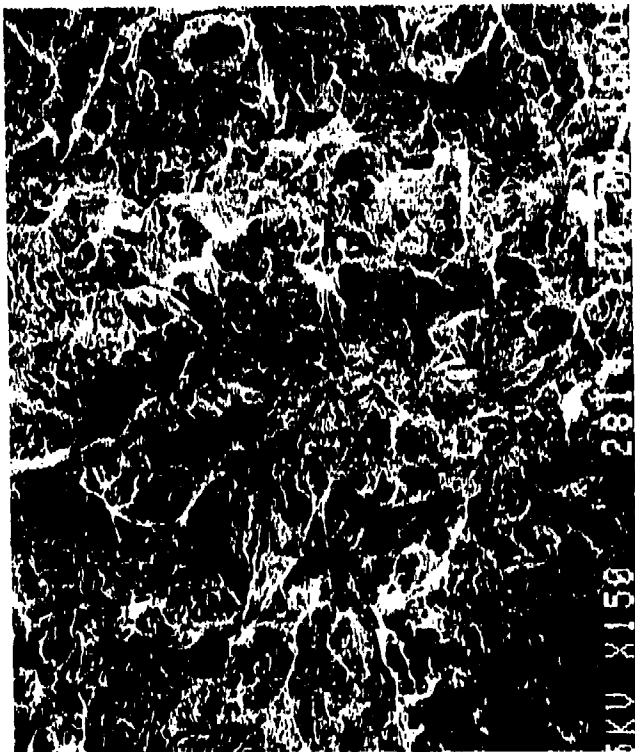


b

Figure 71. Scanning electron photomicrograph of fracture toughness specimen GGN-30 tested at  $-10^{\circ}\text{C}$ . (a) Arrow shows cleavage crack initiation region after small region of stable crack growth (10X). (b) High magnification of the cleavage initiation site (arrow) (1500X).

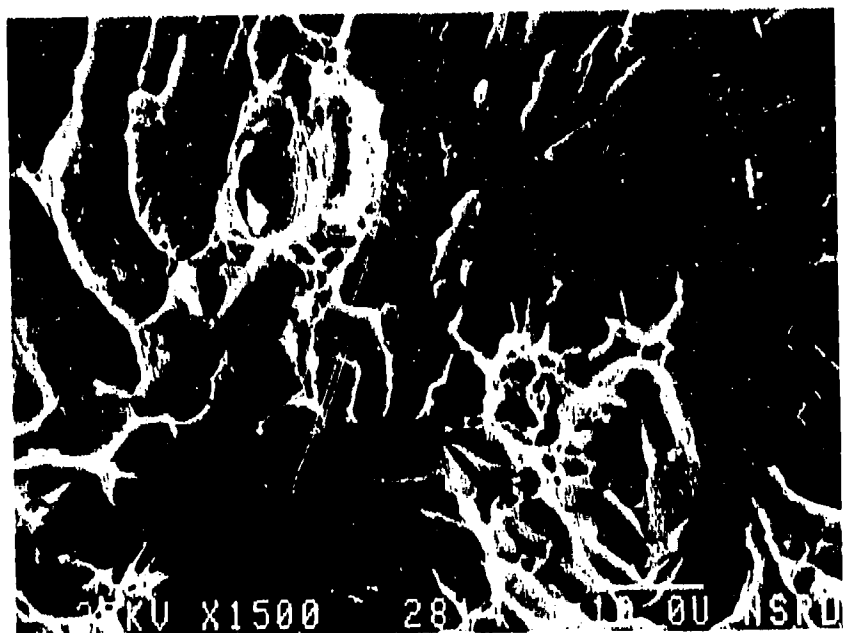


**a**

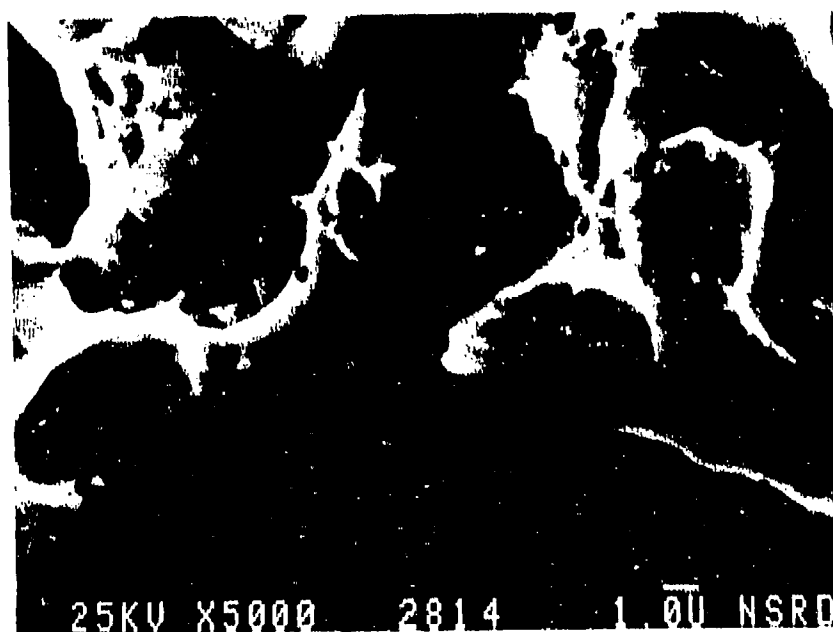


**b**

Figure 72. Stereo scanning electron photomicrograph of the cleavage initiation site on specimen GFF-11. (a)  $7^{\circ}$  with the arrow highlighting the cleavage initiation facet (150X). (b)  $0^{\circ}$  (150X).



a



b

Figure 73. Scanning electron photomicrograph of the cleavage initiating particle on specimen GTF-11. (a) The arrow points to the initiating niobium carbide particle, while the dimple at X was initiated by a manganese sulfide particle (1500X). (b) Higher magnification of the cleavage initiating niobium carbide particle (5000X).

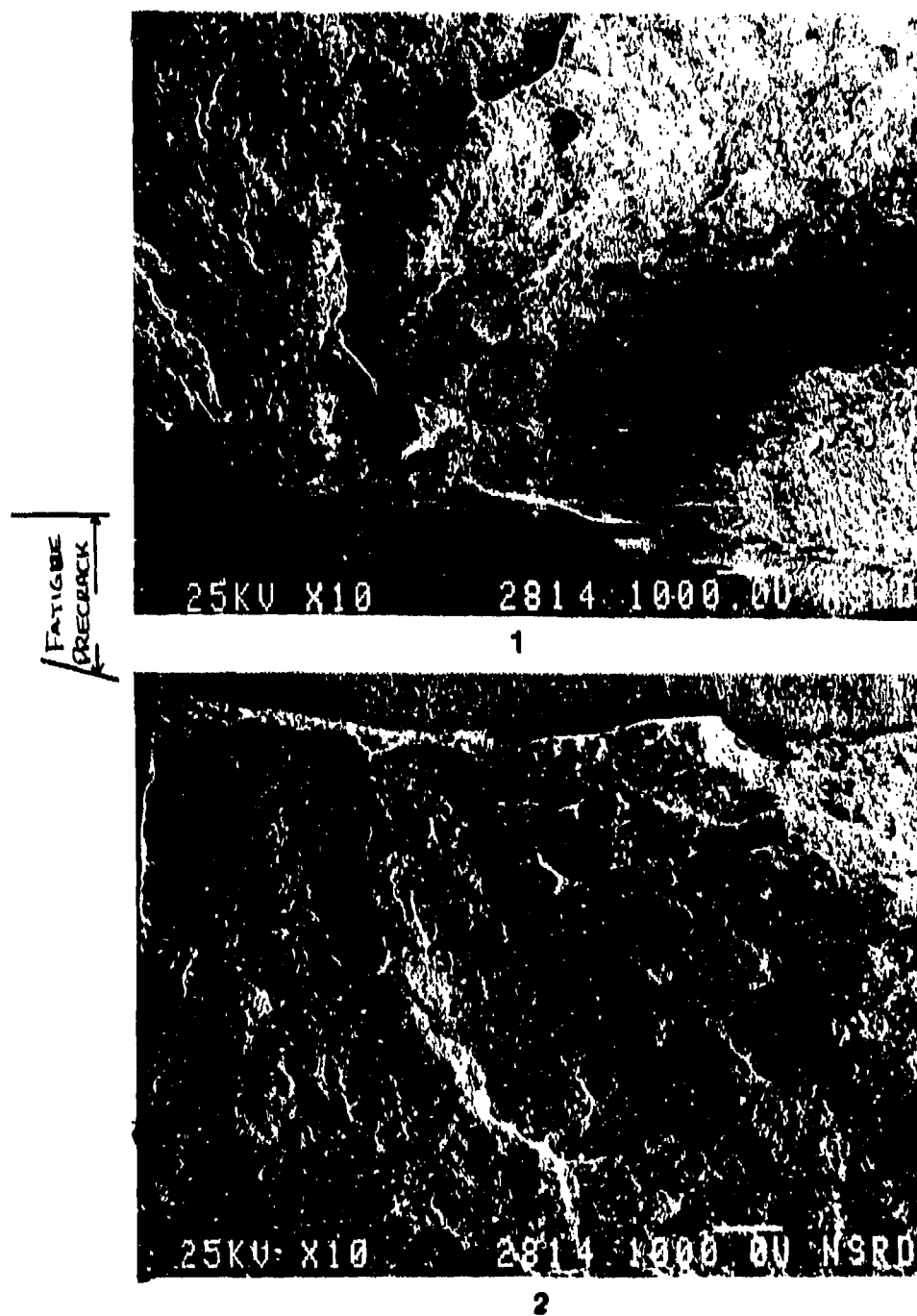
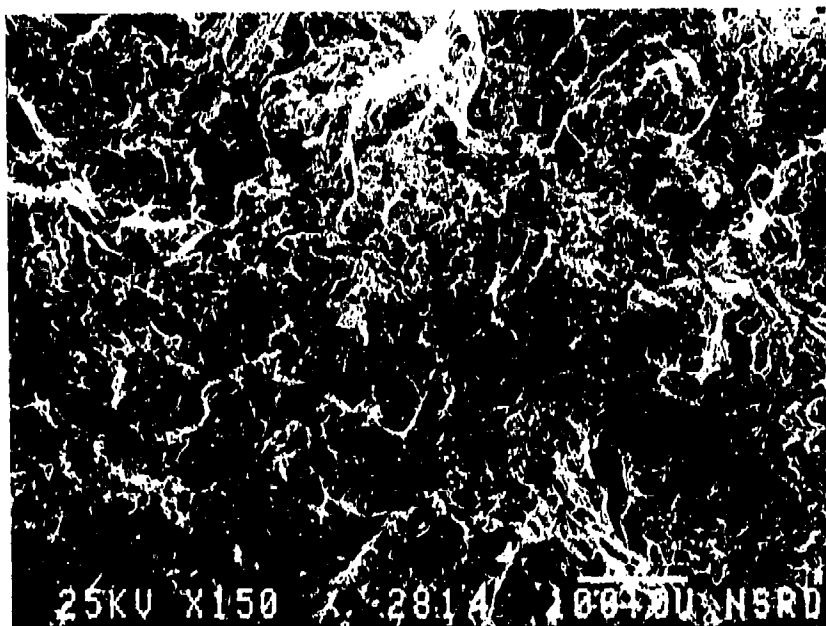


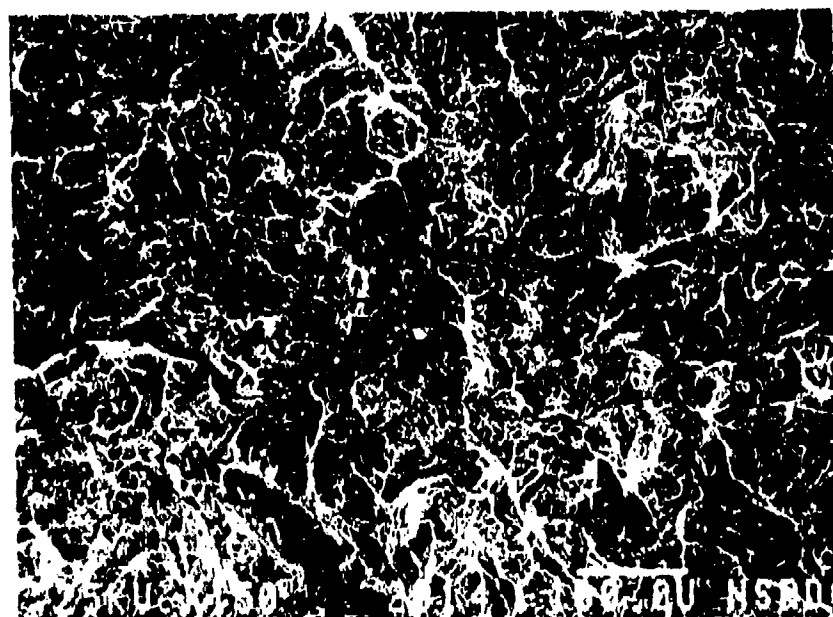
Figure 74. Scanning electron photomicrographs of the matching fracture surfaces from fracture toughness specimen GFF-C tested at  $-100^{\circ}\text{C}$  (10X). The surfaces are labelled 1 and 2.

from each plate that were tested at a temperature just above the lower shelf, brittle fracture mode temperature region. Figure 75 shows the matching fracture surfaces in the region of cleavage crack initiation from specimen GFF-2 with the arrow pointing to the initiating facet. The plastic deformation associated with cleavage is very small which is supported by the fact that these photomicrographs of matching surfaces are almost mirror images of each other. Figure 76 shows the cleavage initiating particle in specimen GFF-2 which was identified as a titanium nitride particle. The titanium nitride particle itself is cracked and the crack can clearly be seen to extend into the ferrite matrix indicating that crack initiation was caused by the cracked particle instead of particle debonding from the matrix.

Table 6 contains the data from the cleavage initiation region characterization measurements made on all of the fracture toughness specimens tested. This information includes initiating facet size, initiating particle identification and size, and distance of the cleavage initiating facet from the fatigue precrack. Carbide and nitride particles were most commonly identified as the microstructural elements responsible for cleavage crack initiation.



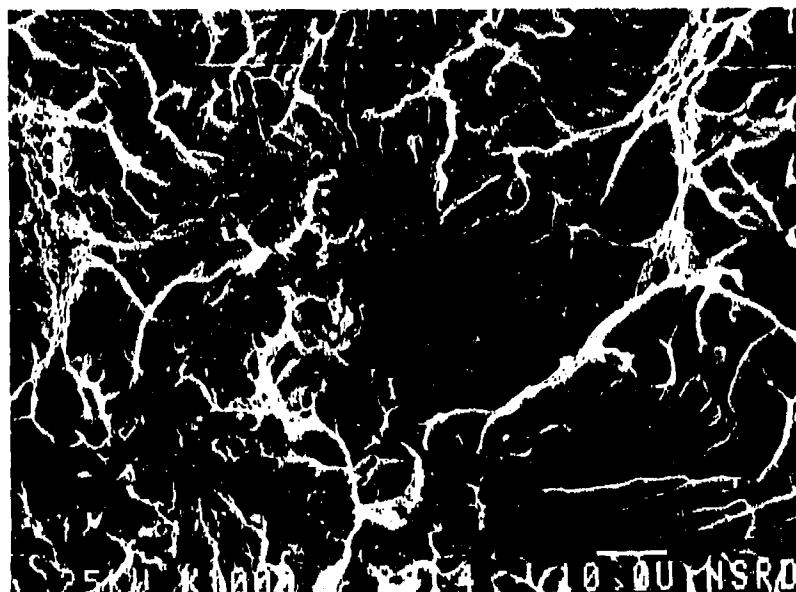
1



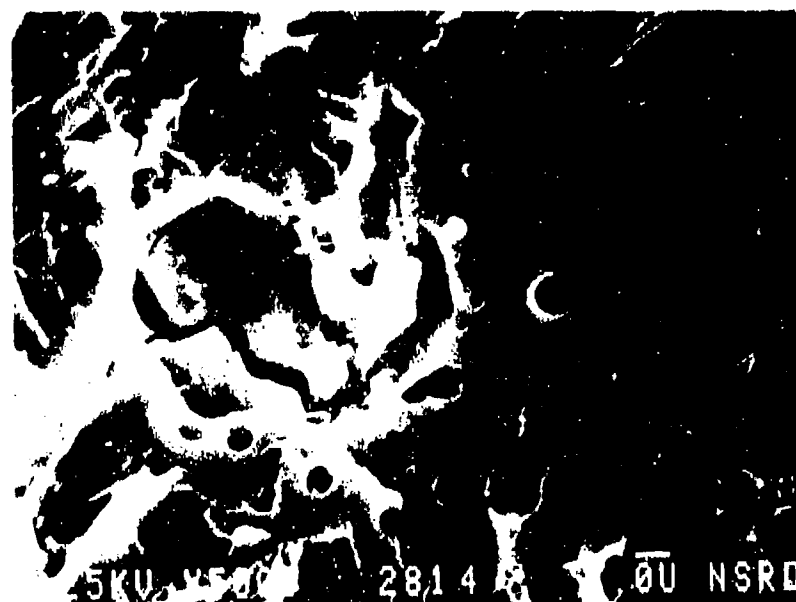
2

Figure 15. Scanning electron photomicrographs of the matching cleavage initiation sites from surfaces 1 and 2 of fracture toughness specimen GFF-2 (150X).





a



b

Figure 76. Scanning electron photomicrograph of the cleavage initiation site on surface 1 of fracture toughness specimen GFF-2. (a) Arrow points to the cracked cleavage initiating titanium nitride particle (1000X). (b) Higher magnification of the cleavage initiation particle (5000X).

TABLE 6

Specimen	Test T (° C)	J <sub>IC</sub> (kJ/m <sup>2</sup> )	J <sub>I</sub>	Initiation Facet Size (micron)	Initiating Particle	(X) Cleavage Initiation*	
						Distance (microns) (r)	(X)
Plate GGN							
31	-10	236	337	25	**	680	750
30	-10	364	378	38	nitride	1310	2090
29	-12		68	48	sulfide		480
27	-12	241	730	21	nitride	280	925
28	-15	292	306	34	carbide	850	950
25	-17		234	41	**		
24	-45		310	35	oxide		
23	-62		37	51	nitride		80
21	-73		271	17	carbide		290
22	-100		34	25	carbide		145
Plate GFF							
11	-70	527	1493	30	sulfide	1560	2330
9	-73	303	1287	48	carbide	1080	2930
6	-85	85	702	54	nitride	875	2250
5	-85	357	1076	37	oxide	620	2560
4	-85	131	651	33	**	450	1870
28	-90	361	660	34	nitride	1400	1760
8	-90	321	657	33	sulfide	580	1940
13	-95	301	1059	57	oxide	150	1400
29	-95	372	817	42	carbide	1025	1900
1	-100		101	29	nitride		540
2	-100		431	45	nitride	710	900
3	-100	125	608	41	carbide		1230
25	-110	165	973	62	**		1370
14	-110	275	412	25	sulfide	290	410
22	-120		345	35	carbide		370

\* The cleavage initiation distance measured is that between the tip of the fatigue pre-crack and the cleavage initiation site.

\*\* No cleavage initiating particle identified.

Table 6. Cleavage fracture initiation data measured from fracture toughness specimens from both plates.

## Secondary Cracking in Fracture Toughness Specimens

Fracture surface profile, metallographic specimens were prepared by sectioning each fracture specimen to expose the microstructure adjacent to the primary crack path on a plane perpendicular to the primary fracture. The fracture surface was protected by plating it with nickel before cutting with the diamond saw. These surfaces were then polished and etched to reveal the microstructure. Scanning electron microscopy of the areas adjacent to the primary fracture allowed measurement of the plastic deformation zone associated with the primary crack at each test temperature and also allowed observation and characterization of the nature of any secondary cracks. Secondary cracks were defined as cracks which initiated and propagated some distance under the same stress field as the primary crack but which did not gain the energy required to sustain crack growth. These cracks provided important information about the cracking process in these materials since they allowed easy study of crack initiation sites, critical propagation distance for self propagation, and high energy microstructures which act as barriers, or arresting structures to crack growth.

A survey of secondary cracks was taken and the crack size distribution is shown in Figure 77. The initiation and arresting sites were identified, and crack length was

# SECONDARY CRACK SIZE DISTRIBUTION Plates GFF and GGN

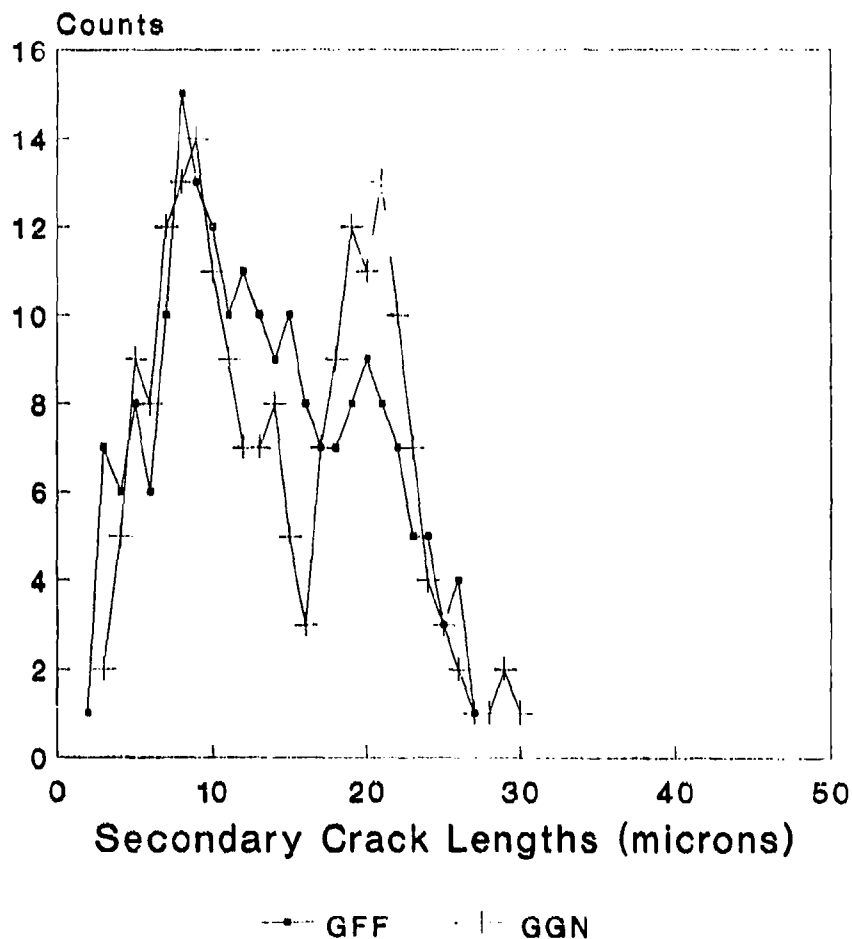


Figure 77. A plot of the distributions of secondary crack sizes measured adjacent to the primary crack in specimens from both plates.

measured. The measurements were only done in two dimensions which did not always allow accurate measure of the total crack length. However, since many cracks were measured it is believed that the average and maximum crack lengths are reasonably accurate. In most cases crack initiation occurred at a ferrite grain boundary, and crack arrest was at the adjacent ferrite grain boundary with some cracks covering several small ferrite grains before arresting, Figures 78 and 79. As can be seen in Figure 77 the peak in the secondary crack length curves coincides with the average grain size for the two plate materials while the maximum secondary crack size was found to be limited to approximately 25 microns in specimens from plate GFF and to 29 microns in plate GGN. As shown by the curve in Figure 77, the distribution of the secondary crack sizes roughly followed the grain size distributions, with specimens from plate GGN exhibiting a dual peak distribution of both grain sizes and secondary crack sizes while specimen from plate GFF exhibit a single peak distribution.

Specimens in the ductile-to-brittle transition temperature region were found to have both voids and secondary cleavage cracks as shown in Figure 80. Void initiation occurred at grain boundaries or precipitates as shown in this figure. In some cases a crack initiated in a ductile mode and then propagated in a cleavage mode as shown by the crack in the upper right portion of Figure 80



**a**



**b**

Figure 78. Scanning electron photomicrograph of secondary cracks adjacent to the main crack in fracture toughness specimen CGN-27 tested at  $-10^{\circ}\text{C}$ . (a) Main crack on the right, two small secondary cracks, each extending for less than a grain diameter, on the left (4000X). (b) Main crack on the right, secondary crack, extending across one small grain, on the left (4000X).

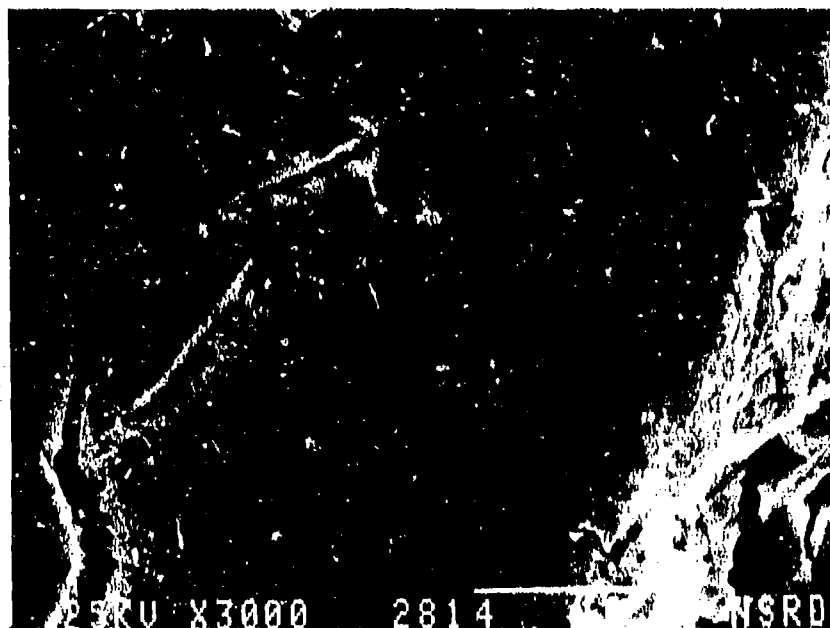


Figure 79. Scanning electron photomicrograph of secondary crack-  
ing in fracture toughness specimen GPF-14 tested at  $-105^{\circ}\text{C}$ .  
The main crack is shown by the arrow (3000X).

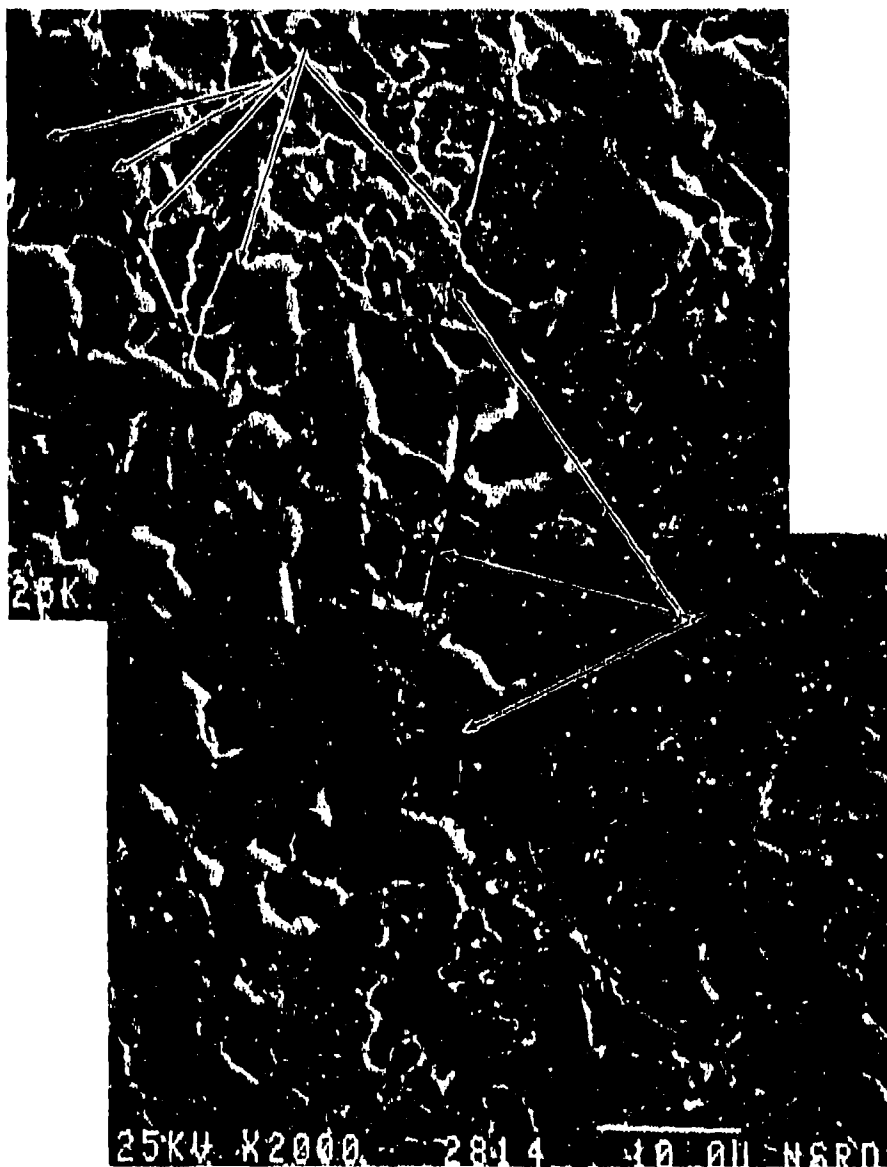


Figure 80. Scanning electron photomicrograph of secondary crack-  
ing in fracture toughness specimen GF1-11 tested at  $-70^{\circ}\text{C}$ . The  
arrows marked (a) point to voids initiating at grain boundaries.  
The arrows marked (b) point to cleavage cracks, most of which  
extend across several grains (2000X).



marked by arrows labelled both a and b. In most cases void initiation occurred readily but void growth was inhibited. Void sizes were limited to the area adjacent to the initiating precipitate at the grain boundary.

## DISCUSSION

### MICROSTRUCTURE, STRENGTH AND TOUGHNESS

#### Microstructure and Strength

The microstructure of the two ASTM A710, Grade A, Class 3, steel plates used in this study consisted of polygonal ferrite interspersed with regions of acicular ferrite, and very small areas of high carbon lath ferrite which may be either lower bainite or martensite. Scoonover and Speich [102] attribute the presence of these higher carbon structures to the rejection of carbon from the polygonal ferrite during cooling. The remaining carbon-rich austenite then transforms at a lower temperature to bainite and martensite, with some austenite remaining even at room temperature which transforms to cementite upon aging [102].

The differences between the microstructure of the two plates were seen in the distribution of grain sizes as well as the distribution of higher carbon lath ferrite microstructures, and carbide precipitates. Plate GGN had a slightly higher carbon content at 0.058 weight percent versus 0.04 weight percent carbon in plate GFF which accounts for the higher carbide content in plate GGN.

Another difference between the two plates occurred in the processing. Plate GFF was ingot cast and thus received a higher degree of deformation during the rolling process to

produce the final 50 mm thick plate than did plate GGN which was originally continuously cast into an 203 mm slab. This may account for the fact that the grain size distribution was more homogeneous in plate GFF which had a unimodal grain size distribution with the peak centered at 3 microns. The average grain size of plate GFF material was 7.8 micron with a standard deviation of 4.6, while plate GGN had a bimodal grain size distribution with grain diameter peaks centered on 3 and 25 microns and an average grain size of 8.7 microns.

The chemistries of the two plate materials differed somewhat resulting in a difference in precipitate size and distribution between the two plates. As shown in Table 2, plate GFF contained a smaller volume percent of both large precipitates and copper precipitates. This difference in precipitation must be considered when attempting to model the strengthening mechanisms present in the two plates. To determine the kinds of strengthening present in these plates, dislocation/precipitate interactions were studied using transmission electron microscopy of thin films made from the ends of Charpy V-notch specimens. Figures 81 and 82 show dislocation/precipitate interactions in the two plates. Precipitation of fine particles was apparent on many dislocations but the "pinned" dislocation line geometries suggested that Orowan type particle strengthening



Figure 81. Transmission electron photomicrograph showing the particle/dislocation interactions in the microstructure of plate GFF.



Figure 82. Transmission electron photomicrograph showing the particle/dislocation interactions in the microstructure of plate GGN.

was present in both plate materials. The larger manganese sulfide, oxide, titanium nitride, and carbide precipitates are impenetrable by the dislocations and act to pin the dislocations. In order for dislocation motion to continue the dislocation must pass around the larger particles leaving a dislocation loop around the particle, which then increases the effect of the particle on further dislocation motion. This "pinning" effect of large particles on dislocation motion is shown by the arrow in figure 83. The dislocations contain sharp angles which result from the local pinning effect of the particle on just the region of the dislocation within the stress field of the particle.

The smaller, copper precipitate clusters also have a strong effect on dislocation motion. Studies of the deformation of steels containing incoherent fcc copper precipitates suggest that the strengthening is caused by an Orowan mechanism [45-47]. Particle shearing was not observed in this, or other studies [45-47], and while dislocation loops were observed, Figure 84, the particles within the loops were not identified.

Nickel in solid solution also affects dislocation motion by increasing the strain in the matrix through atomic misfit, and thus must also be considered when determining the factors contributing to the strengthening of the two plates. Srinivas et al. [103] have studied strengthening in



Figure 83. Transmission electron photomicrograph showing the "pinning" effect of particles on dislocation motion in the microstructure of plate GFF, with resulting strengthening as described by the Orowan equation.



Figure 84. Transmission electron photomicrograph showing the dislocations loops around precipitates in a microstructure consisting of copper precipitates in a ferrite matrix.



Armco iron containing alloy additions in solid solution and determined the matrix friction stress to be approximately 118 MPa which is in good agreement with the results obtained earlier [104].

The contribution to strengthening by the various precipitates should be considered separately because of the variation in particle strength and distribution. Using the expression for Orowan strengthening given in equation <22> to describe the contributions to the yield strength by the niobium carbonitride and copper precipitates, as well as the strengthening caused by the larger inclusions yields an expression for total Orowan strengthening given by:

$$\sigma_o = (6.4 \times 10^{-6} / L_{Cu}) \ln(r_{Cu}/b) + (6.4 \times 10^{-6} / L_{NbCN}) \ln(r_{NbCN}/b) + (6.4 \times 10^{-6} / L_{lg \text{ prec}}) \ln(r_{lg \text{ prec}}/b) \quad <39>$$

where the L and r values are obtained from table 2. The total Orowan strengthening can then be determined using the pythagorean law of superposition proposed by Koppenaal and Kuhlman-Wilsdorf [105] given by:

$$\tau_{total} = (\tau_{Cu}^2 + \tau_{NbCN}^2 + \tau_{lg \text{ prec}}^2)^{1/2} \quad <40>$$

Hornbogen and Staniek [106] found that when precipitate size exceeded  $150 \times 10^{-10}$  m in Fe-1% Cu alloy, strengthening was independent of grain size. It seems reasonable to

assume that grain size strengthening has a negligible effect in age hardened A710 steels due to the large distribution of precipitates. The yield strength of the two plates studied can then be expressed by:

$$\sigma_y = \sigma_i + \sigma_{\text{total}} \quad <41>$$

where:

$$\begin{aligned} \sigma_i &= 118 \text{ MPa for ferrite [103]} \\ b &= 2.5 \times 10^{-10} \text{ m for ferrite [9]} \end{aligned}$$

	GFF	GGN
$r_{\text{Cu}}$	$6 \times 10^{-9} \text{ m}$	$5.5 \times 10^{-9} \text{ m}$
$r_{\text{NbCN}}$	$8 \times 10^{-9} \text{ m}$	$9 \times 10^{-9} \text{ m}$
$r_{\text{lg pre}}$	$15 \times 10^{-9} \text{ m}$	$14 \times 10^{-9} \text{ m}$
$L_{\text{Cu}}$	$7.7 \times 10^{-8} \text{ m}$	$6.5 \times 10^{-8} \text{ m}$
$L_{\text{NbCN}}$	$6.7 \times 10^{-8} \text{ m}$	$6.2 \times 10^{-8} \text{ m}$
$L_{\text{lg. pre.}}$	$4.4 \times 10^{-7} \text{ m}$	$4.2 \times 10^{-7} \text{ m}$

This equation yields the following values for the predicted yield strengths of the two plates;

$$\sigma_{\text{ysGFF}} = 546 \text{ MPa}$$

$$\sigma_{\text{ysGGN}} = 604 \text{ MPa}$$

The measured yield strengths for these two plates are;

$$\sigma_{\text{ysGFF}} = 506 \text{ MPa}$$

$$\sigma_{\text{ysGGN}} = 593 \text{ MPa.}$$

The predicted and empirical yield strengths are in reasonably close agreement indicating that the primary

strengthening mechanism for this material is precipitate strengthening by the Orowan mechanism. The difference in strength between the two plates is attributed to the difference in copper and niobium carbonitride precipitation.

### Microstructure and Toughness

The microstructural parameters affecting strength also play a major role in the resistance of the material to fracture, or the materials fracture toughness. Large precipitates tend to increase strength while having a detrimental effect on toughness [84-92]. The smaller copper precipitates provide an increase in strength but their effects on toughness are more complex and not yet fully understood. A decrease in grain size acts to increase both strength and toughness.

Fracture toughness is described as the ability of a material to resist crack growth. Thus, the fracture mode of a tough material is one of void initiation, growth and coalescence; a very high energy, relatively slow fracture mode due to the degree of plastic deformation involved as the applied stress is absorbed by plastic flow of the material. Cleavage fracture occurs by the nucleation of microcracks, caused by local plastic deformation, and the growth of these cracks under the influence of a local, concentrated tensile stress ahead of the crack tip that

exceeds some critical fracture stress [81]. Once a cleavage crack attains a critical size, it becomes self-propagating as described by Griffith [62] requiring no more applied energy to sustain crack growth. For this reason cleavage is a low energy fracture mode.

Studies of fracture in steels [77-81] have shown that cleavage cracks nucleate at brittle inclusions or particles as a result of strain localization caused by the deformation process. The brittle nature of these inclusions allows the crack to propagate under very little stress, within the particle, until a boundary is encountered resulting in a crack nucleus with a length equal to the particle diameter. Because of the inhomogeneities in the microstructure of most materials, the crack growth process can then be divided into two stages; (a) the initial propagation of the crack into the material immediately surrounding the microcrack nucleus (i.e. the ferrite surrounding a cracked carbide), and (b) the propagation of the crack as obstacles, such as grain boundaries, are encountered. The critical event, i.e. the event controlling the cleavage fracture process and thus the cleavage fracture strength of the material, is determined by which of these two crack propagation stages is the most difficult to accomplish.

Much of the work to date has described the cleavage initiation process in age hardenable steels in terms of the

distribution of critical carbide sizes in front of the crack tip [81, 84-86, 88-90]. These models describe the critical event in the cleavage fracture process as the attainment of a critical stress (that required to fracture a large carbide) over some characteristic distance in front of the crack tip. The critical stress required to cause cleavage failure can then be determined from the carbide size distribution, average grain size, yield strength, effective shear stress, friction stress and plastic work required to fracture ferrite, as described in equation <32>. The characteristic distance is that which ensures the presence of a large carbide oriented favorably to the crack tip such that the crack tip stress field causes brittle fracture of the carbide.

In very low carbon steels such as those studied in this work, there are fewer large carbides than in mild and high carbon steels, and these have large interparticle spacings. This may account for the fact that many of the cleavage fracture initiating particles in this study were identified as other than carbides (nitrides, oxides, sulfides). As the carbon content of steel is lowered, the importance of other large, brittle particles in the cleavage crack nucleation process increases and thus must be considered in models of the cleavage fracture process.

Subcritical, secondary crack sizes were measured on

polished and etched surfaces cut perpendicular to the fracture surface of the fracture toughness specimens. The range of crack sizes measured is shown in Figure 77. Most of the secondary cracks were found to have initiated at ferrite grain boundaries at carbide films or precipitates. These cracks then extended across the ferrite grain and most arrested at the ferrite grain boundary. Few crossed into adjacent ferrite grains suggesting that the crack driving force was insufficient to cause crack propagation through the higher energy ferrite grain boundaries. This may explain why no secondary cracks were found to exceed the maximum grain size measured (41 microns).

Cleavage initiating facets were also characterized with the results shown in Tables 5 and 6. The cleavage initiation facets ranged in size from 20 to 75 microns with plate GGN facets having a larger size range than did those from plate GFF which is consistent with the larger grain size of GGN. The cleavage initiation facet size and the distribution of secondary crack sizes were compared to determine a critical crack size for cleavage failure. These results suggest that the critical flaw size for unstable cleavage failure of these steels is greater than 20 microns (the smallest initiating facet size measured). This supports the suggestion by Curry and Knott [84] that for grain sizes less than 40 microns the critical cleavage event becomes the propagation of the cleavage crack across ferrite

grain boundaries instead of across the carbide/ferrite boundary. Taking this suggestion one step further, in a non-homogeneous grain sized material such as the weld metal studied by Armstrong et al. [92], and plate GGN of the present study, the critical event for cleavage failure becomes the propagation of a crack across a ferrite grain boundary in a region of grains large enough to ensure the attainment of the critical crack size required for self-propagation. In regions of small grains, more grain boundaries must be crossed by the crack before it attains critical size, requiring a larger stress. Crack propagation across grain boundaries requires more energy due to the high strain energy density caused by matrix misorientation between two adjacent grains, while the work required to propagate a crack through the ferrite grains themselves is much less [79,80,85].

The distance from the sharp fatigue precrack to the initiating facet was also measured and found to range from 40 to 500 microns for specimens exhibiting no ductile crack growth prior to unstable cleavage failure, to over 5000 microns for specimens that did exhibit stable ductile crack growth prior to cleavage failure. This distance was smaller on average for specimens from plate GGN indicating that the probability that a crack will attain the critical size for self-propagation is greater in this non-homogeneous grain

sized material. No "characteristic" distance for cleavage initiation was identified in either plate from the measurements of the cleavage initiation site from the growing ductile crack, or the sharp crack. These measurements seemed to be independent of both test temperature fracture toughness values.

The proposed model describes the unstable cleavage fracture process of this steel as: cracks nucleate at large particle and matrix boundaries due to the strain localization that arises when these incoherent particles act as barriers to dislocation glide. The cracks quickly grow to a length equal to the diameter of the brittle particle, which provides little resistance to crack growth. The cracks then propagate into the ferrite matrix under the driving force of the localized strain and are arrested by high energy ferrite grain boundaries. (This step of the model is supported by the presence of a large number of subcritical, secondary, grain sized cracks adjacent to the primary crack in the specimens tested.) When the intensification of the tensile stress distribution in front of the ductile crack tip or notch, due to the applied load is sufficiently high and when it encompasses a grain sized crack of critical length under that stress, all of the conditions are met for unstable cleavage failure.

Using this model, the lower toughness of plate GGN



is explained by: (a) the stress intensification ahead of the crack tip is larger in plate GGN than in plate GFF specimens under a given load due to the higher yield stress of this plate, and (b) plate GGN contains a higher volume fraction of large grain sized flaws (due to the higher fraction of large grains) which can become critical and propagate at lower stresses than those in plate GFF. This model suggests that not only is a small grain size important for high strength and good fracture toughness but also stresses the importance of a homogenized grain size for inhibiting cleavage fracture propagation.

#### MECHANISMS OF LONGITUDINAL CRACKING IN TENSILE SPECIMENS

Longitudinal cracking in steels has been described by several researchers in both fracture toughness specimens [100,101,103,107-114] and in tensile specimens [109,110,112,114-116]. This phenomena has been attributed to many microstructural features including rolling texture, elongated inclusions, aligned carbide planes, and prior austenite and deformed ferrite grain boundaries. Most of the studies using impact toughness specimens have noted that longitudinal cracking, also called splitting and delamination in these studies, has only been observed in the ductile-brittle transition temperature region but little information has been put forth to explain this phenomena.

In the present study longitudinal cracking was not

observed on any of the impact, or quasi-static toughness specimens, but was observed on all tensile specimens except for those tested at the highest temperatures. These results indicate that longitudinal cracking is also a transition fracture phenomena in tensile specimens. The fact that other researchers have not discussed tensile specimen splitting as a transition phenomena may be due to the fact that only room temperature tensile testing was conducted [109,110,112,114-116]. Most of these studies attributed the tendency for splitting to rolling texture and precipitation, and noted that normalizing [109,110,116] and either no aging treatment, or overaging [109-116] inhibited the occurrence of splitting. While it was noted in these studies that these treatments also decreased the impact transition temperatures, these results were not directly related to the lack of observed splitting. Since it has been noted in the present study that splitting is also a transition phenomena in tensile specimens, it is suggested that the processing and composition changes identified in the previous studies depressed the tensile transition temperature such that room temperature tensile properties and fracture mode exhibited upper shelf behavior. That these same processing parameter changes were also found to inhibit splitting in impact specimens is not explained in this study except to note that splitting was not observed in longitudinal impact specimens in this study either. If splitting is a strain controlled

phenomena, as will be described later, and the amount of strain is strain rate dependent, then impact loading may inhibit splitting in non-textured specimens.

Microstructural analysis of both plate materials in this study included neutron pole figures which were done at the National Bureau of Standards [117]. Neither plate exhibited any notable texturing which is probably due to the re-austenitizing, quench, and aging treatment received subsequent to rolling as well as to the high finishing temperature used in the rolling process (above the ferrite transformation temperature). Optical photomicrographs did show slight elongation of the ferrite grains in the direction of rolling, Figures 11 and 12, and plate GGN exhibited a dual grain size distribution with a slight alignment of planes of large grains in the rolling direction. Both of these microstructural features have been associated with splitting [108-110, 112-114] since they were identified with preferential distribution of carbides, or high carbon microstructures in the rolling direction.

The fracture mode observed in the tensile specimens at all but the lowest temperatures was microvoid coalescence. Voids or transverse cracks were also observed at the center of the necked region on the face of the longitudinal cracks at the lowest temperatures as shown in figures 38 and 55 by the interrupted cleavage facets in this region. Microvoid

coalescence and ductile tearing were also the modes of failure in the longitudinal cracks except at the lowest test temperatures where cleavage facets, which followed the deformation pattern of the grains, were observed. This observance of a ductile failure mode in the longitudinal cracks conflicts with most of the studies mentioned above. DeArdo [114] concluded that because two different modes of failure were observed (ductile void coalescence on the transverse fracture surfaces and brittle failure on the longitudinal crack surfaces) that two separate failure mechanisms were involved. Schofield et al. [112] noted, on the other hand, that the ductile-brittle transition temperature was orientation dependent for their impact specimens which may explain why the longitudinal and final transverse fracture modes vary in tensile specimens.

The fact that all of the tensile specimens tested in this study exhibited a considerable amount of necking indicates that longitudinal cracking did not occur until well after the onset of necking and introduction of a triaxial stress state. Because of this, Baldi and Buzzichelli [101] suggested a critical tensile stress criterion for longitudinal cracking. However, the study done by Hicho et al. [116] on notched tensile specimens showed that the onset of stress triaxiality caused by necking, by itself, could not cause longitudinal cracking, but that a critical strain was

required to initiate voids that were then propagated in the longitudinal direction by the transverse stresses introduced by necking.

The idea of a critical strain, when coupled with the theories of both DeArdo [114] and Hero et al. [113] that higher density planes of carbides exist in the rolling (longitudinal) direction and act as void initiation sites in microalloyed steels, can be used to explain the mechanisms of longitudinal cracking observed in the tensile specimens of both plates GGN and GFF.

The specimens tested in this study exhibited the typical ductile-rupture, cup-and-cone type of fracture common for upper-shelf behavior at room temperature or slightly above. In this mode, voids initiate at particles at the center volume of the tensile specimen gage section after the ultimate tensile stress has been exceeded due to strain localization. As loading continues the void density increases and voids grow in size until only thin ligaments remain separating the voids. Fracture occurs when these ligaments rupture [118].

The materials used in this study were observed to have a higher density of aligned carbide precipitates in the longitudinal direction. The actual precipitate densities in the three plate directions were not measured in this study but differences are inferred from the slight grain

shape differences apparent in the optical photomicrographs. Higher density carbide distribution in a particular plate direction has been described by Embury and Cooper [109] as due to the formation of low carbon ferrite at deformed austenite grain boundaries on transformation and the subsequent rejection of carbon towards the centers of the prior austenite grains resulting in coplanar arrays of carbide precipitates. If these carbides act as sites for void initiation, it would be expected that the density of voids might be slightly higher along those planes of carbides in the longitudinal direction.

In the upper transition region the longitudinal cracks were not observed to originate at the center of the tensile specimens. Instead there was a small region of mode one dimples at the center with the longitudinal cracks radiating outward from there. This indicates that the longitudinal cracks did not propagate until after this central void region had coalesced into one large void which suggests a critical strain criteria for longitudinal crack formation.

As the test temperature was decreased, the longitudinal cracks originated closer to the center until the cracks initiated at the center. Even at these temperatures void coalescence was still the failure mode at the center of the specimen and the final transverse fracture occurred at the center of the necked region suggesting that the longitudinal

cracks were not enough to relieve longitudinal stresses.

At the lowest temperatures tested, voids initiated at the center volume of the tensile specimens at precipitates but, once necking had reached a point such that the induced transverse stresses exceeded the transverse fracture stress, the longitudinal cracks propagated in a cleavage mode until outside the necked region. Material outside the neck which had little or no prior strain history then deformed to relax the stresses and arrest the crack. At this point in the fracture process the two halves of the fracture specimen necked region are once again in a plane stress regime and final fracture occurred outside of the necked region with cleavage initiating at the point of longitudinal crack arrest.

Bridgeman [99] and other investigators [119,112] have studied the stress state caused by necking in a tensile specimen. From these studies equations have been put forth which quantify the tangential and radial stresses induced by the curvature at the neck under the influence of the applied load. These stresses are given by:

$$\sigma_r = \sigma_t = \sigma_f [\ln(1 + 1/2(a/r))] \quad <42>$$

where  $\sigma_r$  is the radial stress,  $\sigma_t$  is the transverse stress,  $\sigma_f$  is the fracture stress,  $a$  is the radius of the gage section at the neck and  $R$  is the radius of curvature of the

neck. Using this equation it was determined that the radial stresses just prior to final fracture in the specimens in this study ranged from 480 MPa at room temperature to 580 MPa at the lowest test temperatures. These stresses do not exceed the transverse tensile stresses as measured on transverse specimens and shown in Table 3 but may be large enough to cause void coalescence in the longitudinal direction in strain hardened material. It is assumed here that the transverse tensile properties vary with temperature in a manner similar to longitudinal properties since transverse properties were only measured at room temperature. It is known from the transverse tensile tests that ductility is reduced in the transverse direction. This is supported by other researchers [112-114] who found decreased ductility in through thickness specimens which they attributed to the difference in precipitate density.

The mechanism of longitudinal cracking in tensile specimens is presented as:

- (1) Voids initiate at carbides and other large particles in the center volume of the gage section due to strain localization.
- (2) Necking begins causing the initiation of tangential stresses which have a radial (or transverse) component.
- (3) Void formation is more dense in the longitudinal direction due to the high density of carbides which act as initiation sites resulting in void arrays in the longitudinal direction.
- (4) The induced transverse stresses in the necked region



drive void coalescence in the longitudinal direction until these stresses fall to zero outside the neck, or until longitudinal crack growth relieves the transverse stresses.

- (5) Crack propagation proceeds in the transverse direction until final fracture occurs.

This study has identified longitudinal cracking as a transition phenomena in tensile specimens and has shown that longitudinal cracking may be seen in tensile specimens even when none is observed in impact or quasi-static toughness specimens. Because of this characterization, it is necessary to study the full transition properties of both toughness and tensile specimens when characterizing the effects of processing and compositional changes on mechanical properties.

## CONCLUSIONS

The conclusions of this study are:

(1) The strength of microalloyed steels can be reasonably predicted using the classical models, assuming that the effects of precipitation are additive using the pythagorean superposition rule. Strengthening due to grain size was found to be negligible in comparison to the strengthening contribution of the large distribution of both copper and niobium carbonitride precipitates.

(2) The critical event in the cleavage fracture process controlling toughness in low carbon, low alloy steels is the attainment of a critical stress in front of the crack tip which ensures propagation of a microcrack initiated at a large particle, through the ferrite grain surrounding the particle and into the adjacent ferrite grain. A weakest link statistical modelling approach to describing the fracture toughness of this material must consider the distribution of large precipitates necessary for crack nucleation in conjunction with regions of large grains which increase the probability of crack propagation to a critical size.

(3) Longitudinal cracking in tensile specimens is a transition phenomena with a mechanism consisting of competing critical strain and critical stress criteria. A

large amount of strain is necessary to ensure crack or void initiation along high density, longitudinal planes of carbide precipitates. A large amount of strain also ensures that necking will proceed until the critical transverse stresses can be induced which cause crack propagation in the longitudinal direction prior to transverse crack propagation.

(4) From a detailed microstructural and fractographic analysis of the two plate materials the differences in strength were mainly attributed to the difference in copper and niobium carbonitride precipitate distribution with the higher strength properties found in the plate with the highest volume fraction of both precipitates. The differences in fracture toughness as measured by the fracture appearance transition temperature (FATT) and ductile-brittle transition temperature (DBTT) was attributed to the difference in grain size distribution with the lower toughness exhibited by the plate with a non-homogeneous grain size distribution (higher volume fraction of large grains).

## SUGGESTED WORK

More work is required to fully understand the longitudinal cracking phenomena in high strength, low alloy steels. A full characterization of the tensile and impact properties in all three plate directions, as well as more detailed study of the microstructural elements involved, would eliminate the need for the assumptions made in this paper.

It is also necessary to gain a better understanding of the effects of copper precipitation on fracture toughness.

## REFERENCES

- [1] DeArdo, A.J., J.M.Gray, and L.Meyer, "Fundamental Metallurgy of Niobium in Steel", Niobium-Proceedings of the International Symposium, H.Stuart, Ed., TMS-AIME, New York, 1984, p 685
- [2] Montemarano, T.M., B.P.Sack, J.P.Gudas, M.G.Vassilaros, and H.H.Vandervelt, "High Strength, Low Alloy Steels in Naval Construction", J. of Ship Production, Vol. 2, pp145-162
- [3] Gray, J.M., "Processing and Properties of Low Carbon Steel", Transactions of the Metallurgical Society, AIME, 1973, p225
- [4] Hornbogen, E., and R.C.Glenn, Transactions of the Metallurgical Society - AIME, Vol. 218, 1962, p525
- [5] Jolley, W., Transactions of the Metallurgical Society - AIME, Vol. 242, 1968, pp306-314
- [6] Kelly, R.E., Masters Thesis, University of Texas, El Paso, 1974
- [7] Coldren, A.P., T.G.Oakwood, and G. Tither, "Microstructure and Properties of Controlled-Rolled and Accelerated Cooled, Molybdenum Containing Linepipe Steels", J. of Materials for Energy Systems, Vol. 5, No. 4, March 1984,
- [8] Lin, Ing-Hour, "Fracture and Flow of Iron and Its Alloys: Theory and Experiment", Ph.D. Dessertation, The Ohio State University, 1980
- [9] Gladman, T., D.Dulieu, and I.D. McIvor, "Structure-Property Relationships in High-Strength, Microalloyed Steel", Microalloying '75, Union Carbide Corp., New York, N.Y., 177, pp 32-55
- [10] Irvine, K.J., F.B.Pickering, and T. Gladman, "Grain Refined C-Mn Steels", J. of Iron and Steel institute, Vol. 205, 1967, pl61
- [11] Hall, E.O., Proceedings, Physics Society, Vol. 64B, 1951, p747
- [12] Petch, N.J., "The Cleavage Strength of Polycrystals", J. of Iron and Steel Institute, Vol. 174, 1953, p25
- [13] Hillert, M.M., Acta Metallurgica, Vol. 13, 1965, p227

- [14] Cottrell, A.H., Transactions TMS-AIME, Vol. 212, 1958, p 192
- [15] Wilson, D.V., and J.A.Chapman, Phil. Magazine, Vol. 8, 1963, p 1543
- [16] Worthington, P.J., and E.Smith, Phil. Magazine, Vol. 9, 1964, p 211
- [17] Marcinkowski, M.J., and R.M.Fisher, Transactions TMS-AIME, Vol. 233, 1965, p 293
- [18] Meakin, J.D., and N.J.Petch, ASD-TDR-63-324, Orlando, Fla., 1963, p 2243
- [19] Conrad, H., Electron Microscopy and Strength of Crystals, Ed. Thomas and Washburn, Interscience, 1963, p 299
- [20] Brandon, D.G., and J. Nutting, J. of the Iron and Steel Institute, Vol. 196, 1960, p160
- [21] Li, J.C.M., and Y.T. Chou, "The Role of Dislocations in the Flow Stress - Grain Size Relationship", Metallurgical Transactions, Vol. 1, May 1970, p 1145
- [22] Li, J.C.M., "Petch Relation and Grain Boundary Sources", Transactions of TMS-AIME, Vol. 227, No. 1, Feb. 1963, pp239-247
- [23] Bramfitt, R.L., and A.R.Marder, Proceedings of the Processing and Properties of Low Carbon Steel Conference, AIME, 1973, pp 191-224
- [24] Little, J.M., J.A.Chapman, W.B.Morrison, and B.Mintz, Proceedings, 3<sup>rd</sup> International Conference on the Strength of Metals and Alloys, Inst. of Metals and the Inst. of Iron and Steel, Publ. No. 36, Vol 1, 1973, pp 80-84
- [25] Gladman, T., Proc. of the Royal Society, Vol. 294A, 1966, P298
- [26] Gladman, T., and D.Dulieu, Metal Science, June 1974, p167
- [27] Cuddy, L.J., Thermomechanical Processing of Microalloyed Austenite, TMS-AIME, PA., 1982, pp 129-140
- [28] Amin, R.K., and F.B.Pickering, Thermomechanical Processing of Microalloyed Austenite, TMS-AIME, Pa., 1982, pp 1-3

- [29] DiMicco, D.R., and A.T.Davenport, Thermomechanical Processing of Microalloyed Austenite, TMS-AIME, Pa., 1982, pp 59-81
- [30] Amin, R.K. and F.B.Pickering, Thermomechanical Processing of Microalloyed Austenite, TMS-AIME, Pa., 1982, pp 377-403
- [31] LeBon, A., J.Refes-Vernis, and C.Rossard, Metal Science, Vol. 9, 1975, p36
- [32] Kubota, H., et. al., Nippon Kokan Technical Report, OVERSEAS, No. 29, 1971, p23
- [33] Coladas, R., J.Masolinave, and J.P.Bailon, The Hot Deformation of Austenite, J.Ballance, Ed., TMS-AIME, New York, 1976
- [34] Jonas, J., and I Weiss, Metal Science, Vol. 13, 1979, p 238
- [35] Webster, D., and J.A.Woodhead, J. of the Iron and Steel Institute, Vol. 202, 1964, p 987
- [36] Jones, J.D., and A.B.Rothwell, Deformation Under Hot-Working Conditions, ISI Publication No. 108, London, 1968, p 78
- [37] Gray, J.M., D.Webster, and J.H.Woodhead, "Precipitation in Mild Steel Containing Small Additions of Niobium", J. of The Iron and Steel Institute, Aug. 1965, p812
- [38] Watanabe, H., Y.E.Smith, and R.D.Pehlke, The Hot Deformation of Austenite, J.Ballance, Ed., TMS-AIME, New York, 1975, p145
- [39] Gray, J.M., and R.B.G.Yeo, "Columbium Carbonitride Precipitation in Low-Alloy Steels with Particular Emphasis on 'Precipitate-Row' Formation", Transactions of ASM, Vol. 61, 1968, p255
- [40] Morrison, W.B., "The Strengthening of Carbon Steel by Small Niobium Additions", Iron and Steel, Aug. 1964, p390
- [41] Gray, J.M., Metallurgical Transactions, Vol. 3, 1972, p 1495
- [42] Gray, J.M., and W.G.Wilson, 14<sup>th</sup> Mechanical Working and Steel Processing Conference Proceedings, TMS-AIME, N.Y., 1972

- [43] Lloyd, D.J., "Precipitation Hardening", Proceedings of the International Conference on Stresses in Metals and Alloys, Montreal, 1986, p 1745
- [44] Smith, C.S., and E.W. Palmer, "The Precipitation-Hardening of Copper Steel," Transactions AIME, Vol. 105, Feb. 1933, pp133-168
- [45] Hornbogen, E., and R.C. Glenn, "A Metallographic Study of Precipitation of Copper from Alpha-Iron," Transactions TMS-AIME, Vol. 218, Dec. 1960, p1064
- [46] Goodman, S.R., S.S. Brenner, and J.R. Low, Jr., An FIM-atom Probe Study of the Precipitation of Copper from Iron-1.4 At.% Copper, Part II; Atom Probe Analysis," Metallurgical Transactions, Vol. 4, 1973, p2371
- [47] Miglin, M.T., J.P. Hirth, A.R. Rosenfield, and W.A.T. Clark, "Microstructure of a Quenched and Tempered Cu-Bearing High Strength, Low Alloy Steel," Metallurgical Transactions, Vol. 17A, May 1986, p791
- [48] Armstrong, R.W., "The Influence of Polycrystal Grain Size on Several Mechanical Properties of Materials", Metallurgical Transactions, Vol. 1, May 1970, p 1169
- [49] Mott, M.F., and F.R.N.Nabarro, Proceedings, Physics, Society, Vol. 59, 1940, p 86
- [50] Mott, N.F., Imperfections in Nearly Perfect Crystals, J.H.Jollomon, et.al. Eds., John Wiley and Son, New York, 1952, p173
- [51] Orowan, E., Proceedings of the International Conference on Stresses in Metals and Alloys, Inst. of Metals, London, 1948, p 451
- [52] Ashby, M.F., Acta Metallurgica, Vol. 14, 1966, p 679
- [53] Kocks, U.F., Philos. Magazine, Vol. 13, 1966, p 541
- [54] Tresca, H., Compt. Rend. Academy of Science, Paris, Vol. 59, 1864, p754
- [55] Teoh, L.L., "Advances in Low Carbon, High Strength Steels", SEASI Quarterly, Jan. 1983, pp 71-81
- [56] Baumgardt, H., H.de Boer, and F. Heisterkamp, "Review of Microalloyed Structural Plate Metallurgy - Alloying, Rolling, and Heat Treatment", Niobium - Proceedings of the International Symposium, Ed. H. Stuart, TMS-AIME,



Warrendale, Pa., 1984, p 883

- [57] Speich, G., and D.S.Dabkowski, The Hot Deformation of Austenite, TMS-AIME, New York, 1977, p 577
- [58] Orowan, E., Dislocations in Metals, AIME Publication No. 128, 1954
- [59] Leslie, W.C., "Inclusions and Mechanical Properties", ISS-Transactions, Vol. 2, 1983, p 1
- [60] Gladman, T., J. of The Iron and Steel inst., Vol. 203, 1965, p1038
- [61] Natishan, M.E., "Micromechanisms of the Cleavage Fracture Process in High Strength, Low Alloy Steels", David Taylor Research Center Annual IR/IED Report, No. 88/CT02, 1988
- [62] Griffith, A.A., "The Phenomena of Rupture and Flow in Solids", Royal Society Proceedings, VCCXXI - A587, Oct. 1920, p 163
- [63] ASTM Book of Standards, E399, ASTM, Easton, Md., 1987
- [64] Zener, C., "The Micro-Mechanisms of Fracture", Trans-ASM, Vol. 40A, 1948, p 3
- [65] Ewing, J.A., and W. Rosenhain, "Experiments in Micro-Metallurgy; Effects of Strain", Proceedings of the Royal Society, Vol. 65, 1899, p 85
- [66] Reynolds, A.W., J. of Applied Physics, Jan. 1948
- [67] Burke, J.E., and C.S.Barrett, "The Nature of Strain Markings in Alpha-Brass", Metals Technology, AIME Technical Publication No. 2327, Feb. 1948,
- [68] Stroh, A.N., "The Formation of Cracks as as Result of Plastic Flow", Proceedings of the Royal Society, Vol. A233, 1954, p 404
- [69] Mott, N.F., Proceedings of the Royal Society, Vol. A220, 1953, p 1
- [70] Eshelby, J.D., F.C.Frank, and F.R.N.Nazarro, Philos. Magazine, Vol. 42, 1951, p 351
- [71] Cottrell, A.H., "Theory of Brittle Fracture in Steel and Similar Metals", Transactions TMS-AIME, Vol. 212, 1958, pp192-203

- [72] Stroh, A.N., "Theory of the Fracture of Metals", *Advances in Physics*, Vol. 6, 1957, pp 418-434
- [73] Hahn, G.T., and A.R. Rosenfield, "A Modified Double-Pile-Up Treatment of the Influence of Grain Size and Dispersed Particles on Brittle Fracture", *Acta Metallurgica*, Vol. 14, 1966, pp 1815-1825
- [74] Koehler, J.S., *Physics Review*, Vol. 85, 1952, p480
- [75] Low, J.R. Jr., "The Relation of Microstructure to Brittle Fracture", *Transactions ASM*, Vol. 46A, 1954, pp 163-179
- [76] Orowan, E., Fatigue and Fracture of Metals, John Wiley and Son, New York, 1952, p 139
- [77] Stroh, A.N., "Brittle Fracture and Yielding", *Philos. Magazine*, Vol. 46, 1955, p 968
- [78] McMahon, C.J., and M. Cohen, "Initiation of Cleavage in Polycrystalline Iron", *Acta Metallurgica*, Vol. 13, June 1965
- [79] McMahon, C.J., and M. Cohen, "The Fracture of Polycrystalline Iron", Proceedings of the First International Conference on Fracture, Vol. 121965, pp 779-812
- [80] Smith, E., "The Nucleation and Growth of Cleavage Microcracks in Mild Steel", Proceedings of the Conference on the Physical Basis Yield and Fracture, Inst. of Physics and Physical Society, Oxford, 1966, pp 36-46
- [81] Ritchie, R.O., J.F. Knott, and J. Rice, "On the Relationship Between Critical Tensile Stress and Fracture Toughness in Mild Steel", *J. of Mechanics and Physics of Solids*, Vol. 21, 1973
- [82] Hutchinson, J.W., "Singular Behavior at the End of a Tensile Crack in a Hardening Material", *J. of Mechanics and Physics of Solids*, Vol. 16, 1968, pp 13-31
- [83] Rice J.R., and G.F. Rosengren, "Plane Strain Deformation Near a Crack Tip in a Power Law Hardening Material", *J. of Mechanics and Physics of Solids*, Vol. 16, 1968 pp 1-12
- [84] Curry, D.A., and J.F. Knott, "The Relationship Between Fracture Toughness and Microstructure in the Cleavage Fracture of Mild Steel",

- [85] Curry, D.A. and J.F.Knott, "Effects of Microstructure on the Cleavage Fracture Stress in Steel", Metal Science, Vol. 12, No. 11, 1978, pp 511-514
- [86] Knott, J.F., Proceedings of the Fourth International Conference on Fracture, Ed. D.M.R.Taplin, Pergamon Press, New York, 1978, pp 61-92
- [87] Armstrong, R.W., Acta Metallurgica, Vol. 15, 1967, p 667
- [88] Curry, D.A., "Predicting the Temperature and Strain Rate Dependence of the Cleavage Fracture Toughness of Ferritic Steels", Materials Science and Engineering, Vol. 43, 1980, pp135-144
- [89] Wallin, K., T. Saario, and K.Torrenen, "Statistical Model for Carbide Induced Brittle Fracture in Steel", Metal Science, Vol. 18, Jan. 1984, pp 13-16
- [90] Lin, T., A.G.Evans, and R.O.Ritchie, "A Statistical Model of Brittle Fracture by Transgranular Cleavage", Lawrence-Berkeley Report No. LBL-19673, May 1985
- [91] Rosenfield, A.R., D.K.Shetty, and A.J.Skidmore, "Fractographic Observations of Cleavage Initiation in the Ductile-Brittle Transition Region of a Reactor Pressure Vessel Steel", Metallurgical Transactions, Vol. 14A, Sept. 1983, p 1934
- [92] Zhang, X.J., R.W.Armstrong, and G.R.Irwin, J. of Material Science Letters, Vol. 5, 1986, pp 961-964
- [93] Joyce, J.A., and J.P.Gudas, Elastic-Plastic Fracture, ASTM STP 668, ASTM, Philadelphia, 1979, pp 451-468
- [94] Hudak, S.J., Jr., A.Saxena, R.J.Bucci, and R.C.Malcolm, "Development of Standard Methods of Testing and Analyzing Fatigue Crack Growth Rate Data", Air Force Materials Laboratory Technical Report No. AFML-TR-78-40, August 1978
- [95] Ernst, H., P.C.Paris, and J.D.Landes, Fracture Mechanics: 13<sup>th</sup> Symposium, ASTM STP 743, Ed. R.Rokerts, ASTM, Philadelphia, 1981, pp 476-502
- [96] Bridgeman, P.W., Studies in Large Plastic Flow and Fracture, McGraw-Hill Book Co., New York, 1952, pp 9-37
- [97] Czyryca, E.J., Unpublished tensile data on ASTM A710, grade A, class 3, steels plates coded GFF and GGN, David Taylor Research Center, 1984

- [98] Joyce, J.A., and D.F.Hasson, "Characterization of Transition Temperatrue Behavior of Hy-130 Steel by the J<sub>IC</sub> Fracture Toughness Parameter", J. of Engineering Fracture Mechanics, Vol. 13, 1980, pp 417-430
- [99] Beachem, C.D., Metallurgical Transactions, Vol. 6A, 1975, p 377
- [100] Bramfitt, B.L., and A.R.Marder, "Splitting Behavior in Plate Steels", Toughness Characterization and Specifications for HSLA and Structural Steels, Ed. P.L. Mangonon, Jr., TMS-AIME, Warrendale, Pa., 1979, p239
- [101] Baldi, G., and G.Buzzichelli, "Critical Stress for Delamination Fracture of HSLA Steels", Metals Science, Oct. 1978, p459
- [102] Speich, G.R., and T.M.Scoonover, "Continuous Cooling Transformation Behavior of HSLA-80 (A710) Steel", presented at the TMS-AIME Symposium on Processing, Microstructure and Properties of HSLA Steels, Nov. 1987, Pittsburg, Pa.
- [103] Srinivas, M., G.Malakondalah, and P.Rama Rao, "The Influence of Polycrystal Grain Size on Fracture Toughness of, and Fatigue Threshold in Armco Iron", Unpublished Draft Article submitted to Engineering Fracture Mechanics for the issue honoring Takeo Yokobori, 1987
- [104] Anderson, E., D.W.L. King, and J.Spreadborough, "The Relationship between Lower Yield Strength and Grain Size in Armco Iron," Transactions AIME, Vol. 242, 1968, p115
- [105] Koppenaal, T.J., and D.Kuhlman-Wilsdorf, Applied Physics Letters, Vol. 14, 1964, pp 59-61
- [106] Hornbogen, E., and G. Staniak, "Grain Size Dependence of the Mechanical Properties of an Age Hardening Fe-1%Cu Alloy," J. of Materials Science, Vol. 9, 1974, pp 879-886
- [107] Armstrong, R.W., L.R.Link, and G.R.Speich, "Analysis of Ductile-Brittle TRANSITION Temperatures For Controlled-Rolled, Microalloyed, C-Mn Steels", DTRC/SME-88-30, David Taylor Research Center, May 1988
- [108] Speich, G.R., and D.S.Dabkowski, Proceedings - Hot Deformation of Austenite, AIME Conference, J.B.Ballance Ed., AIME New York, 1979, pp 557-597

- [109] Embury, J.D., and K.Cooper, "Some Aspects of the Fracture Behavior of High Strength, Low Alloy Steels' Canadian Metallurgical Quarterly, Vol. 14, 1975, p 69
- [110] Dabkowski, D.S., P.J.Konkol, and M.F.Baldy, "Splitting-Type Fractures in High Strength Line-Pipe Steels", Metals Engineering Quarterly, Feb. 1976
- [111] English, A.T., "Influence of Mechanical Fiberling on Anisotropy of Strength and Ductility", J. of Metals, April 1965, p 395
- [112] Schofield, R., G.Rowntree, N.V.Sarma, and R.T.Weiner, "Arrowhead Fractures in Controlled-Rolled Pipeline Steels Metals Technology, July 1974, p 325
- [113] Hero, H., J.Evensen, and J.D.Embury, "The Occurrence of Delamination in Control Rolled HSLA Steel", Canadian Metallurgical Quarterly, Vol. 14, No. 2, 1975, pp 117-122
- [114] DeArdo, A.J., "An Investigation of the Mechanisms of Splitting Which Occurs in Tensile Specimens of High Strength, Low Alloy Steels", Metallurgical Transactions A, Vol. 8A, March 1977, p 473
- [115] Hicho, G.E., S.Singhal, L.C.Smith and R.J.Fields, "Effects of Thermal Processing Variations on the Mechanical Properties and Microstructure of a Precipitation Hardened HSLA Steel", J. of Heat Teating, Vol. 3, No. 3, June 1984, p 205
- [116] Hicho, G.E., C.H.Brady, L.C.Smith, and R.J.Fields, "Effects of Heat Treatment on Mechanical Properties of ASTM A710 Steel", NBSIR 84-2891, National Bureau of Standards, March 1985
- [117] Crooks, M.J., L.C.Smith, and R.C.Reno, "Microstructural Evaluation of Explosion Bulge Tested HSLA Plate," NBSIR 87-3647, National Bureau of Standards, Oct. 1987
- [118] Wilsdorf, H.G.F., "Void Initiation, Growth and Coalescence in the Ductile Fracture of Metals", J. of Electronic Materials, Vol. 4, No. 5, 1975, p 791
- [119] Davidenkov, N.N., and N.I.Spiridonova, "Mechanical Methods of Testing - Analysis of the State of Stress in the Neck of a Tensile Test Specimen", Proceedings ASTM, Vol. 46, 1946, pp 1-12
- [120] Parker, E.R., H.E.Davis, and A.E.Flannigan, "A Study of the Tension Test", A paper presented at the 49<sup>th</sup> Annual meeting of the Society, June 24-28, 1946

# INITIAL DISTRIBUTION

## Copies

## CENTER DISTRIBUTION

		Copies	Code
1	DDRE/Lib		
1	CNO/OP 098T	1	01A (DDM)
		1	011.3
2	OCNR	1	011.5
	1 432S	1	17
	1 Library	1	172
		2	172.4
1	NAVPGSCOL	1	172.5
		1	173
1	USNROTCU	1	173.3
	NAVADMINU MIT	1	174
		1	174.3
3	NRL	1	174.4
	1 Code 6380	1	28
	1 Code 6384	1	2801
	1 Code 6322	2	2803
		1	2809
20	NAVSEA	5	281
	1 SEA 05M	1	2812
	1 SEA 05MB	1	2812 (TMS)
	2 SEA 05M2	5	2814
	1 SEA 05R	25	2814 (MEN)
	1 SEA 05R25	1	2814 (EJC)
	1 SEA 05R26	1	2814 (LRL)
	2 SEA 08	1	2814 (RJA)
	1 SEA 55Y	1	2814 (MGV)
	1 SEA 55Y1	1	2815
	1 SEA 55Y12	1	522.2
	1 SEA 55Y2	2	5231
	1 SEA 55Y21		
	1 SEA 55Y22		
	1 SEA 55Y23		
	1 SEA 55Y3		
	1 SEA 55Y31		
	2 SEA 99612		
12	DTIC		